Transient Response of a Loaded Horizontal Antenna
Over Lossy Ground with Application to EMP Simulators

Y. Rahmat-Samii
P. Parhami
R. Mittra

University of Illinois
Urbana, Illinois 61801

Abstract

A novel technique is developed for evaluating the Sommerfeld-type integrals encountered when analyzing a horizontal current element over lossy ground. The integration results are compared with their asymptotic values, making it possible to efficiently compute the currents of a horizontal antenna over lossy ground. The frequency domain results are compared with those available in the literature, and the Fast Fourier Transform (FFT) technique is used for obtaining the current transient response due to an input pulse excitation. The effect of loading is also investigated for reducing the undesirable ringing behavior present in the late time antenna current. Extensive numerical results are computed and repeated by using an efficient user oriented computer program developed for this work.

Acknowledgement

Transient Response of a Loaded Horizontal Antenna
Over Lossy Ground with Application to EMP Simulators

Y. Rahmat-Samii
P. Parhami
R. Mittra

University of Illinois
Urbana, Illinois 61801

Abstract

A novel technique is developed for evaluating the Sommerfeld-type integrals encountered when analyzing a horizontal current element over lossy ground. The integration results are compared with their asymptotic values, making it possible to efficiently compute the currents of a horizontal antenna over lossy ground. The frequency domain results are compared with those available in the literature, and the Fast Fourier Transform (FFT) technique is used for obtaining the current transient response due to an input pulse excitation. The effect of loading is also investigated for reducing the undesirable ringing behavior present in the late time antenna current. Extensive numerical results are computed and repeated by using an efficient user oriented computer program developed for this work.

Acknowledgement

TABLE OF CONTENTS

LIST OF FIGURES

4

Page

1. INTRODUCTION

An electromagnetic pulse (EMP) generated by a nuclear burst typically has a fast rise time ($\sim$10 nsecs), a slow decay time ($\sim$100 nsecs) and a high peak amplitude (on the order of several kilovolts per meter) [1]. Such a pulse has deleterious effects on most systems, such as transmission lines, transmitting and receiving installations, and missiles, causing temporary or permanent damage. In recent years, several designs have been proposed and built for EMP testing of vulnerable systems. Simulators may be classified as open or closed types depending on the nature of propagation mechanism they support. For example, a parallel-plate structure is considered as a closed simulator while a horizontal antenna is referred to as an open simulator.

A need for an accurate analysis of these simulators is apparent as their construction is very expensive. In this report, we investigate the performance of an open simulator which is composed of a horizontal antenna over lossy ground. The radiated field of this structure behaves differently from the driving pulse mainly because of the multiple reflections occurring at the two ends of the antenna, which, in turn, cause the undesirable ringing phenomenon in the time domain (transient) response. This ringing effect may be suppressed by employing an extremely long antenna in which the source current pulse becomes negligibly small as it travels to the end points. Such a long simulator has in fact been built and has a length of approximately 300 meters [1]. However, lengthening the size of the wire is not the only way to reduce the ringing effect. In this report we investigate an alternate approach based on appropriately loading the antenna to suppress the ringing effect. This approach has the merit of keeping the antenna size to reasonable length.

6

The radiation characteristics of loaded and unloaded linear antennas in free space have been studied in great detail in both the frequency and time domains. A recent book edited by Felsen [2] covers these topics in depth, and contains pertinent references. Frequency domain responses of linear antennas over lossy ground have originally been investigated by Miller, et al. [3,4] and more recently by others [5,6]. The basic difficulty observed in incorporating the ground effects is the accurate and efficient evaluation of Sommerfeld-type integrals. These integrals appear in the exact solution of the radiated field of a current element over ground, and their original forms were first obtained by Sommerfeld [7] almost 70 years ago. Since that time, these integrals have been studied extensively and approximations for their evaluation have been developed for them by many authors [8-13]. Since the integral equation for the antenna current requires the repeated computation of these Sommerfeld integrals, an efficient and accurate numerical method for their evaluation would be extremely useful. Moreover, one must repeat the frequency domain calculation for many frequencies in the process of constructing the time domain (transient) response making the computation even more time-consuming. To the best of our knowledge a thorough study of the time domain responses of antennas over lossy (imperfect) ground has not yet been reported in the literature.

The present work is an attempt to address the aforementioned problem, i.e., to investigate the transient response of a loaded horizontal antenna over lossy ground. Initially, in Section 2, we derive the vector potentials due to a horizontal current element in terms of Sommerfeld-type integrals. A novel and efficient procedure is then outlined in Section 3 for numerically evaluating these integrals. Also included in this section is the asymptotic evaluation of the integrals in terms of Fresnel reflection coefficients.

7

Extensive results are presented to justify the accuracy of the technique developed along with a comparison between the asymptotic solution and the numerical evaluation of the integrals. Section 4 develops an integral equation formulation for the antenna current in the frequency domain and discusses the numerical procedure used to solve this integral equation, based on the application of the method of moments and the finite difference technique. The results obtained are compared with the available data to verify the accuracy of the method. In the final section, the Fast Fourier Transform (FFT) algorithm is used to convert the frequency domain results into the time domain responses. Extensive numerical results are presented for the transient current induced on both the loaded and unloaded antennas placed over a lossy ground. Also included is Appendix III, a self-contained report which investigates the loading characteristics of linear antennas over lossy ground.

2. DERIVATION OF $\vec{\Pi}$ FOR A HORIZONTAL CURRENT ELEMENT

The geometry of a current element P_1 over an imperfect ground is depicted in Figure 1. Regions 1 and 2 are characterized by $(\varepsilon_1 = \varepsilon_{1r}\varepsilon_0, \mu_1 = \mu_0)$ and $(\varepsilon_2 = \varepsilon_{2r}\varepsilon_0, \mu_2 = \mu_0)$, respectively, where ε_0 and μ_0 are free-space parameters. The current element is in the x-direction (horizontal) and its coordinates are $(0,0,h)$. The geometrical image of P_1 with respect to the interface is designated by P_2, and the distances of P_1 and P_2 to the observation point O, with coordinates (x,y,z), are labelled as $P_1 O = r_1$ and $P_2 O = r_2$, respectively. Our objective is to determine the field radiated by P_1 at the observation point O in the presence of the imperfect ground.

Starting with Maxwell's equation and the suppressed time convention $\exp(j\omega t)$, viz.,

$$\nabla \times \vec{H} = j\omega\varepsilon_0\varepsilon_r\vec{E} + \vec{J} \qquad (2.1a)$$

$$\nabla \times \vec{E} = -j\omega\mu_0\vec{H} \quad , \qquad (2.1b)$$

one may define the vector potential $\vec{\Pi}$ as

$$\vec{H} = j\omega\varepsilon_0\varepsilon_r \ \nabla \times \vec{\Pi} \qquad (2.2)$$

Introduction of a scalar potential Φ from

$$\nabla\Phi = \vec{E} - \omega^2\mu_0\varepsilon_0\varepsilon_r\vec{\Pi} \qquad (2.3)$$

and application of the Lorentz gauge

$$\nabla \cdot \vec{\Pi} - \Phi = 0 \quad , \qquad (2.4)$$

allows one to finally express Maxwell's equation as

9
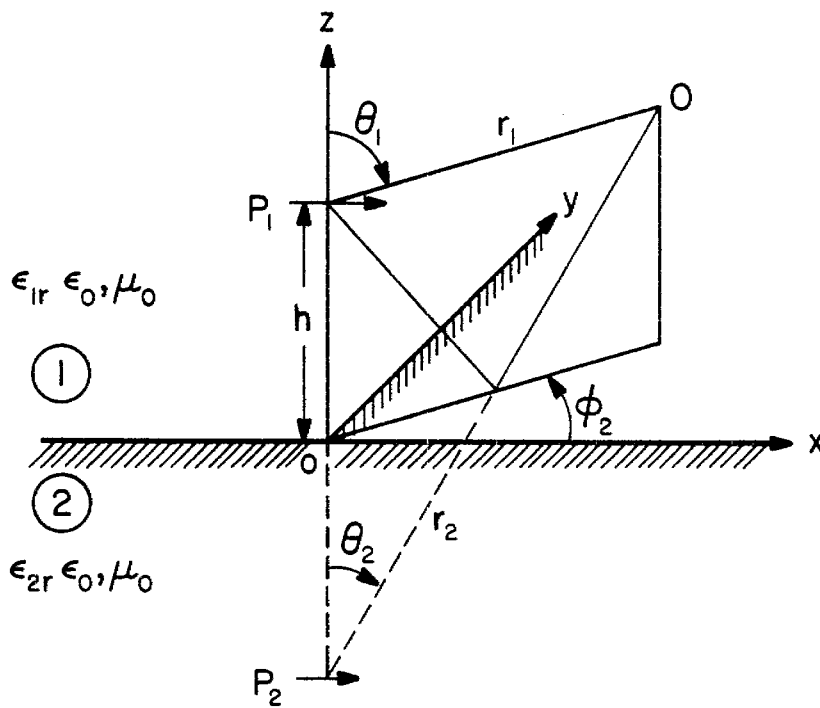
Figure 1.   Geometry and the coordinate systems for the current element P_1 radiating over imperfect ground.

$$(\nabla^2 + k^2)\, \vec{\Pi} = -(j\omega\varepsilon_0\varepsilon_r)^{-1}\, \vec{J} \qquad (2.5)$$

$$\vec{H} = j\omega\varepsilon_0\varepsilon_r\, \nabla \times \vec{\Pi} \qquad (2.6)$$

$$\vec{E} = (\nabla\nabla\cdot + k^2)\, \vec{\Pi} \qquad (2.7)$$

where $k^2 = \omega^2\mu_0\varepsilon_0\varepsilon_r$. The preceding results are general and valid for both regions 1 and 2. To solve the vector differential equation (2.5), one determines the proper boundary conditions by simply enforcing the continuity of the tangential $\vec{E}$ and $\vec{H}$ fields at the interface resulting in

$$\frac{\partial}{\partial x}\Pi_{1x} + \frac{\partial}{\partial z}\Pi_{1z} = \frac{\partial}{\partial x}\Pi_{2x} + \frac{\partial}{\partial z}\Pi_{2z} \qquad (2.8a)$$

$$\Pi_{1x} = \kappa\Pi_{2x} \qquad (2.8b)$$

$$\Pi_{1z} = \kappa\Pi_{2z} \qquad (2.8c)$$

$$\frac{\partial}{\partial z}\Pi_{1x} = \kappa\frac{\partial}{\partial z}\Pi_{2x} \quad , \qquad (2.8d)$$

where $\kappa = \varepsilon_{2r}/\varepsilon_{1r}$. The unique physical solution is then obtained by imposing the radiation condition.

For the horizontal current element P_1 with moment I dx', the source current $\vec{J}$ may be set as

$$\vec{J}_1 = \hat{x}I\, dx'\, \delta(x)\, \delta(y)\, \delta(z - h) \qquad (2.9)$$

where h is the height of the current element from the interface. As originally observed by Sommerfeld [7], two components of the Hertz potential $\vec{\Pi}$ are needed for a complete description of the horizontal current element problem. This, however, is not the case for the vertical current element, in which only one component is needed. The two components are chosen to be in the $\hat{x}$ and $\hat{z}$ directions, i.e., along the current element

and along the normal to the interface, and are designated as follows

$$\vec{\Pi} = \Pi_x \hat{x} + \Pi_z \hat{z} \tag{2.10}$$

2.1   Solution in the Transform Domain

To determine Π_x and Π_z from (2.5) and (2.8), respectively, the Fourier transform technique is used. This technique has been employed extensively in the literature for solving infinite-interface-type problems. Here, the technique is only briefly discussed and the final results are presented. The two-dimensional Fourier transform pair is defined as

$$\tilde{\vec{\Pi}} = \int\int_{-\infty}^{\infty} \vec{\Pi} \exp[-j(\alpha x + \beta y)] \, dx \, dy \tag{2.11a}$$

$$\vec{\Pi} = \frac{1}{4\pi^2} \int\int_{-\infty}^{\infty} \tilde{\vec{\Pi}} \exp[j(\alpha x + \beta y)] \, d\alpha \, d\beta \tag{2.11b}$$

The transform of (2.5), in terms of its components, takes the following forms in regions 1 and 2, viz.,

$$\left(\frac{\partial^2}{\partial z^2} + \gamma_1^2 \right) \left\{ \begin{array}{c} \tilde{\Pi}_{1x} \\ \tilde{\Pi}_{1z} \end{array} \right\} = \left\{ \begin{array}{c} -I_0 \, \delta(z-h) \\ 0 \end{array} \right\} \tag{2.12}$$

and

$$\left(\frac{\partial^2}{\partial z^2} + \gamma_2^2 \right) \left\{ \begin{array}{c} \tilde{\Pi}_{2x} \\ \tilde{\Pi}_{2z} \end{array} \right\} = \left\{ \begin{array}{c} 0 \\ 0 \end{array} \right\} \tag{2.13}$$

where γ_i (i = 1,2) and I_0 have been defined as

12

$$\gamma_i = [k_i^2 - \alpha^2 - \beta^2]^{1/2}, \quad \text{Im}(\gamma_i) \leq 0 \tag{2.14}$$

$$I_0 = (j\omega\varepsilon_0\varepsilon_{1r})^{-1} \, Idx' \tag{2.15}$$

where $k_i^2 = \omega^2\mu_0\varepsilon_{ir}\varepsilon_0.$

The general solution of (2.12) and (2.13) which satisfies the radiation condition may be expressed as

$$\begin{Bmatrix} \tilde{\Pi}_{1x} \\ \tilde{\Pi}_{1z} \end{Bmatrix} = \begin{Bmatrix} I_0 \, \exp(-j\gamma_1|z-h|)/(2j\gamma_1) \\ 0 \end{Bmatrix} + \begin{Bmatrix} A_{1x} \\ A_{1z} \end{Bmatrix} \exp(-j\gamma_1 z),$$

$$z \geq 0 \tag{2.16}$$

$$\begin{Bmatrix} \tilde{\Pi}_{2x} \\ \tilde{\Pi}_{2z} \end{Bmatrix} = \begin{Bmatrix} A_{2x} \\ A_{2z} \end{Bmatrix} \exp(j\gamma_2 z) \qquad z \leq 0 \tag{2.17}$$

where A's are constant coefficients in terms of α and β. The Fourier transform of the boundary condition (2.8) is

$$\begin{bmatrix} j\alpha & \dfrac{\partial}{\partial z} & -j\alpha & -\dfrac{\partial}{\partial z} \\[2mm] 1 & 0 & -\kappa & 0 \\[2mm] 0 & 1 & 0 & -\kappa \\[2mm] \dfrac{\partial}{\partial z} & 0 & -\kappa\dfrac{\partial}{\partial z} & 0 \end{bmatrix} \begin{bmatrix} \tilde{\Pi}_{1x} \\[2mm] \tilde{\Pi}_{1z} \\[2mm] \tilde{\Pi}_{2x} \\[2mm] \tilde{\Pi}_{2z} \end{bmatrix} = 0 \tag{2.18}$$

13

Substituting (2.16) and (2.17) into (2.18) and solving the resulting equation

for A's, one finally arrives at

$$A_{1x} = I_0 \frac{\gamma_1 - \gamma_2}{2j\gamma_1 (\gamma_1 + \gamma_2)} \exp(-j\gamma_1 h) \qquad (2.19a)$$

$$A_{1z} = I_0 \frac{\alpha(\kappa-1)}{j(\gamma_1 + \gamma_2)(\kappa\gamma_1 + \gamma_2)} \exp(-j\gamma_1 h) \qquad (2.19b)$$

$$A_{2x} = I_0 \frac{1}{j\kappa(\gamma_1 + \gamma_2)} \exp(-j\gamma_1 h) \qquad (2.19c)$$

$$A_{2z} = I_0 \frac{\alpha(\kappa-1)}{j\kappa(\gamma_1 + \gamma_2)(\kappa\gamma_1 + \gamma_2)} \exp(-j\gamma_1 h) \quad . \qquad (2.19d)$$

Having obtained the A's, one can then determine the $\tilde{\Pi}$'s from (2.16) and

(2.17) and find

$$\begin{Bmatrix} \tilde{\Pi}_{1x} \\ \tilde{\Pi}_{1z} \end{Bmatrix} = I_0 \begin{Bmatrix} \frac{1}{2j\gamma_1} \\ 0 \end{Bmatrix} \exp(-j\gamma_1 |z-h|) + I_0 \frac{1}{j(\gamma_1 + \gamma_2)} \begin{Bmatrix} \frac{\gamma_1 - \gamma_2}{2\gamma_1} \\ \frac{\alpha(\kappa-1)}{\kappa\gamma_1 + \gamma_2} \end{Bmatrix}$$

$$\cdot \exp[-j\gamma_1(z+h)] \qquad (2.20)$$

and

$$\begin{Bmatrix} \tilde{\Pi}_{2x} \\ \tilde{\Pi}_{2z} \end{Bmatrix} = I_0 \frac{1}{j\kappa(\gamma_1 + \gamma_2)} \begin{Bmatrix} 1 \\ \frac{\alpha(\kappa-1)}{\kappa\gamma_1 + \gamma_2} \end{Bmatrix} \exp(-j\gamma_1 h) \exp(j\gamma_2 z). \qquad (2.21)$$

It is worth mentioning that the counterparts of (2.20) and (2.21) can

easily be obtained for a vertical current element. Using (2.20) and (2.21)

in the transform versions of (2.6) and (2.7), one finds

14

$$
\begin{bmatrix} \tilde{E}_x \\[2ex] \tilde{E}_y \\[2ex] \tilde{E}_z \end{bmatrix} = \begin{bmatrix} k^2-\alpha^2 & -\alpha\beta & j\alpha\dfrac{\partial}{\partial z} \\[2ex] -\alpha\beta & k^2-\beta^2 & j\beta\dfrac{\partial}{\partial z} \\[2ex] j\alpha\dfrac{\partial}{\partial z} & j\beta\dfrac{\partial}{\partial z} & \left(k^2+\dfrac{\partial^2}{\partial z^2}\right) \end{bmatrix} \begin{bmatrix} \tilde{\Pi}_x \\[2ex] 0 \\[2ex] \tilde{\Pi}_z \end{bmatrix}
\tag{2.22}
$$

and

$$
\begin{bmatrix} \tilde{H}_x \\[2ex] \tilde{H}_y \\[2ex] \tilde{H}_z \end{bmatrix} = j\omega\varepsilon_0\varepsilon_r \begin{bmatrix} 0 & -\dfrac{\partial}{\partial z} & j\beta \\[2ex] \dfrac{\partial}{\partial z} & 0 & -j\alpha \\[2ex] -j\beta & j\alpha & 0 \end{bmatrix} \begin{bmatrix} \tilde{\Pi}_x \\[2ex] 0 \\[2ex] \tilde{\Pi}_z \end{bmatrix}
\tag{2.23}
$$

2.2 Space-Domain Integral Representations

Since in this work the primary interest lies in the evaluation of the fields in region 1, attention is therefore focused on the determination of space-domain integral representations for Π_{1x} and Π_{1z}. These integral representations take many different forms and a comprehensive discussion is given in [9]. In this paper an attempt is made to use the form which has the contributions from the incident and reflected parts in an explicit manner. To obtain this form, one first splits Π_{1x} from (2.20) into

$$
\tilde{\Pi}_{1x} = \tilde{\Pi}_{1x}^i + \tilde{\Pi}_{1x}^r
\tag{2.24a}
$$

$$
\tilde{\Pi}_{1x}^r = {}_\infty\tilde{\Pi}_{1x}^r + {}_0\tilde{\Pi}_{1x}^r
\tag{2.24b}
$$

15

where

$$\tilde{\Pi}_{1x}^{i} = I_0 \; \frac{1}{2j\gamma_1} \; \exp(-j\gamma_1|z-h|) \tag{2.25a}$$

$$\left\{ \begin{array}{c} {}_{\infty}\tilde{\Pi}_{1x}^{r} \\[2ex] {}_{0}\tilde{\Pi}_{1x}^{r} \end{array} \right\} = I_0 \; \left\{ \begin{array}{c} \dfrac{-1}{2j\gamma_1} \\[2ex] \dfrac{1}{j(\gamma_1+\gamma_2)} \end{array} \right\} \; \exp[-j\gamma_1(z+h)] \tag{2.25b}$$

and then redefines $\tilde{\Pi}_{1z}$ as

$$\tilde{\Pi}_{1z} = \tilde{\Pi}_{1z}^{r} \; . \tag{2.26}$$

In the preceding equations, $\tilde{\Pi}_{1x}^{i}$ may be interpreted as the source contribution when no ground is present, ${}_{\infty}\tilde{\Pi}_{1x}^{r}$ is the image contribution when the ground is a perfect conductor, and finally ${}_{0}\tilde{\Pi}_{1x}^{r}$ and $\tilde{\Pi}_{1z}^{r}$ are the correction terms for the imperfect ground.

The objective is to determine the inverse Fourier transforms of $\tilde{\Pi}$'s by using (2.11b). By substituting ${}_{\infty}\tilde{\Pi}_{1x}^{r}$ from (2.25b) into (2.11b) and introducing the following spherical-type change of variables:

$$\left\{ \begin{array}{l} x = r_2 \; \sin\theta_2 \; \cos\phi_2 = \rho_2 \; \cos\phi_2 \\[1.5ex] y = r_2 \; \sin\theta_2 \; \sin\phi_2 = \rho_2 \; \sin\phi_2 \\[1.5ex] z+h = r_2 \; \cos\theta_2 = z_2 \end{array} \right. \tag{2.27}$$

$$\left\{ \begin{array}{l} \alpha = -\lambda \; \cos\zeta \\[1.5ex] \beta = -\lambda \; \sin\zeta, \end{array} \right. \tag{2.28}$$

16

one arrives at

$$\infty \Pi_{1x}^r = -\frac{I_0}{4\pi j} \int_0^\infty \frac{\lambda}{\sqrt{k_1^2 - \lambda^2}} J_0(\rho_2 \lambda) e^{-jz_2\sqrt{k_1^2 - \lambda^2}} \, d\lambda \qquad (2.29)$$

with the requirement that $\text{Im} \sqrt{k_1^2 - \lambda^2} \leq 0$. In deriving the preceding
equation the following identity was used, viz.,

$$\cos(n\tau)J_n(z) = \frac{(-j)^{-n}}{2\pi} \int_{-\pi}^\pi e^{-jz\cos(\tau'-\tau)} \cos(n\tau')d\tau' \qquad (2.30)$$

where J_n is the nth-order Bessel function. Expression (2.29) can be
integrated in a closed form to yield

$$\infty \Pi_{1x}^r = -I_0 \frac{e^{-jk_1 r_2}}{4\pi r_2} \qquad (2.31)$$

Similarly, the inverse Fourier transform of $\tilde{\Pi}_{1x}^i$, defined in (2.25a), can
be constructed to give

$$\Pi_{1x}^i = \frac{I_0}{4\pi j} \int_0^\infty \frac{\lambda}{\sqrt{k_1^2 - \lambda^2}} J_0(\rho_2\lambda) e^{-j|z_1|\sqrt{k_1^2-\lambda^2}} \, d\lambda \qquad (2.32)$$

or

$$\Pi_{1x}^i = -I_0 \frac{e^{-jk_1 r_1}}{4\pi r_1} \qquad (2.33)$$

In (2.33) and (2.31), (r_1, θ_1, ϕ_1) and (r_2, θ_2, ϕ_2) are the spherical coordinates

erected at the source and its image point , respectively. The geometry of
these coordinates is shown in Figure 1.

   Although, as was expected, Π_{1x}^i and $_\infty\Pi_{1x}^r$ could be expressed in a
closed form, this is not the case for $_0\Pi_{1x}^r$ and Π_{1z}^r. Substituting $_0\tilde\Pi_{1x}^r$ from
(2.25b) into (2.11b) and incorporating the transformations given in (2.27)
and (2.28) along with (2.30), one finally arrives at

$$_0\Pi_{1x}^r = \frac{2I_0}{4\pi j} \int_0^\infty \frac{\lambda}{\sqrt{k_1^2-\lambda^2} + \sqrt{\kappa k_1^2-\lambda^2}} J_0(\rho_2\lambda)e^{-jz_2\sqrt{k_1^2-\lambda^2}} \, d\lambda \quad . \qquad (2.34)$$

Similarly, after some manipulations, it is found that

$$\Pi_{1z}^r = -\frac{2I_0}{4\pi k_1^2} \cos\phi_2 \int_0^\infty \lambda^2 \frac{\sqrt{k_1^2-\lambda^2} - \sqrt{\kappa k_1^2-\lambda^2}}{\kappa\sqrt{k_1^2-\lambda^2} + \sqrt{\kappa k_1^2-\lambda^2}} J_1(\rho_2\lambda)e^{-jz_2\sqrt{k_1^2-\lambda^2}} \, d\lambda \quad ,$$

$$(2.35)$$

where in (2.34) and (2.35) relations $\mathrm{Im}\sqrt{k_1^2-\lambda^2} \le 0$ and $\mathrm{Im}\sqrt{\kappa k_1^2-\lambda^2} \le 0$ hold.
Integral representations (2.34) and (2.35) are the well-known Sommerfeld's
integrals for a lossy ground [7]. Attempts have been made to employ
these equations in numerical evaluations, and some degree of success has
been achieved [3-6], [10]. In this work, however, other forms of these
integrals that appear to be numerically more tractable are used.

   Incorporating the well-known identities between Bessel and Hankel
functions, viz.,

18

$$J_i(x) = \frac{1}{2} \left[H_i^{(1)}(x) + H_i^{(2)}(x) \right] \quad ; \quad i = 0, 1 \tag{2.36a}$$

$$H_0^{(1)}(x) = -H_0^{(2)}(-x) \tag{2.36b}$$

$$H_1^{(1)}(x) = H_1^{(2)}(-x) \tag{2.36c}$$

into (2.34) and (2.35), one arrives at

$$_0\Pi_{1x}^r = \frac{I_0}{4\pi j} \int_{-\infty}^{\infty} \frac{\lambda}{\sqrt{k_1^2 - \lambda^2} + \sqrt{\kappa k_1^2 - \lambda^2}} \, H_0^{(2)}(\rho_2 \lambda) e^{-jz_2\sqrt{k_1^2 - \lambda^2}} \, d\lambda \tag{2.37}$$

and

$$\Pi_{1z}^r = -\frac{I_0}{4\pi k_1^2} \cos\phi_2 \int_{-\infty}^{\infty} \lambda^2 \frac{\sqrt{k_1^2 - \lambda^2} - \sqrt{\kappa k_1^2 - \lambda^2}}{\kappa\sqrt{k_1^2 - \lambda^2} + \sqrt{\kappa k_1^2 - \lambda^2}} \, H_1^{(2)}(\rho_2 \lambda)$$

$$\cdot e^{-jz_2\sqrt{k_1^2 - \lambda^2}} \, d\lambda \quad . \tag{2.38}$$

The behavior of (2.37) and (2.38) at $\rho_2 = 0$ is discussed in Section 3, and it is shown that these integrals are indeed bounded at $\rho_2 = 0$, which can be observed directly from (2.34) and (2.35).

To recast (2.37) and (2.38) to yet another form which is of considerable interest in this work, the following change of variable is introduced.:

$$\lambda = k_1 \sin \xi \tag{2.39}$$

Substituting (2.39) into (2.37) and (2.38) and simplifying the result, one

finally arrives at

$$_0\Pi_{1x}^r = \frac{I_0 k_1}{4\pi j} \int_\Gamma \frac{\sin\xi \cos\xi}{\cos\xi + \sqrt{\kappa - \sin^2\xi}} \, H_0^{(2)}(k_1 \rho_2 \sin\xi)$$

$$\cdot \, e^{-jk_1 z_2 \cos\xi} \, d\xi \qquad (2.40)$$

and

$$\Pi_{1z}^r = -\frac{I_0 k_1}{4\pi} \cos\phi_2 \int_\Gamma \sin^2\xi \cos\xi \, \frac{\cos\xi - \sqrt{\kappa - \sin^2\xi}}{\kappa \cos\xi + \sqrt{\kappa - \sin^2\xi}}$$

$$\cdot \, H_1^{(2)}(k_1 \rho_2 \sin\xi) e^{-jk_1 z_2 \cos\xi} \, d\xi \quad , \qquad (2.41)$$

where the integration path Γ is depicted in Fig. 2, and on this path the

following conditions are enforced

$$Im(\cos\xi) \leq 0 \; ; \; Im(\sqrt{\kappa - \sin^2\xi}) \leq 0 \quad . \qquad (2.42)$$

Some discussions on the proper interpretation of the location of poles

and branch cuts of the integrands of (2.41) and (2.42) in the proper

Riemann sheet are given in Section 3. Since in constructing the integral

equation for the horizontal antenna problem the knowledge of $\frac{\partial}{\partial z} \Pi_{1z}^r$ is

important, one evaluates this term using (2.41) along with the fact that

$z_2 = z + h$ to obtain

20
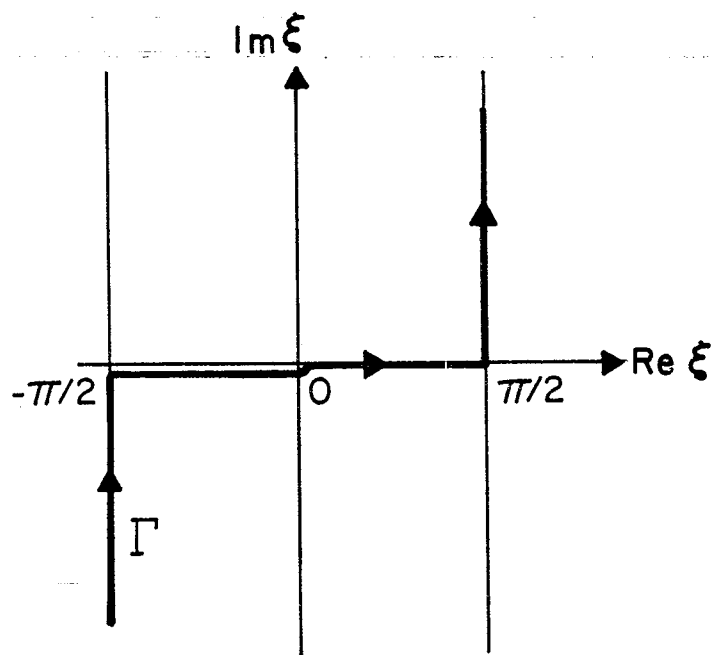
Fig. 2.   Integration path Γ in the complex ξ-plane.

$$\frac{\partial}{\partial z} \; \Pi_{1z}^{r} = \frac{j I_0 k_1^2}{4\pi} \; \cos\phi_2 \int_\Gamma \sin^2 \xi \cos^2 \xi \; \frac{\cos \xi - \sqrt{\kappa - \sin^2 \xi}}{\kappa \, \cos \xi + \sqrt{\kappa - \sin^2 \xi}}$$

$$\cdot \, H_1^{(2)}(k_1 \rho_2 \, \sin\xi) \; e^{-j k_1 z_2 \, \cos \xi} \; d\xi \quad . \qquad (2.43)$$

In the following section, asymptotic and numerical evaluations of (2.40-43) are presented.

22

3. EVALUATION OF THE INTEGRALS

In this section, an analysis is given for asymptotic and numerical evaluation of the integrals obtained in the preceding sections. In particular, a novel numerical procedure is presented for the evalution of (2.40) - (2.43). A comparison is then made between asymptotic and numerical results to evaluate the domain of their validities.

3.1 Asymptotic Evaluation

The asymptotic expansion of (2.40) is obtained by employing the results summarized in Appendix I. Using (2.27) in (2.40), one may express it as

$$
{}_0\Pi^r_{1x} = \frac{I_0 k_1}{4\pi j} \int_\Gamma P(\xi) \ e^{-jk_1 r_2 \cos(\xi - \theta_2)} \ d\xi \tag{3.1}
$$

where

$$
P(\xi) = \frac{\sin \xi \cos \xi}{\cos \xi + \sqrt{\kappa - \sin^2 \xi}} H_0^{(2)} (k_1 r_2 \sin \theta_2 \sin \xi)
$$

$$
\cdot \ e^{jk_1 r_2 \sin\theta_2 \sin\xi} \tag{3.2}
$$

Let $\theta_2 = \theta_c$ designate a critical angle for which the steepest descent path (SDP) of (3.1) is near the branch points of $\sqrt{\kappa - \sin^2 \xi}$ (see Section 3.2). For the situation in which $k_1 r_2$ is large and the domain of θ_2 belongs to $0 < \theta_2 < \theta_c$, one may use the results given in Appendix I to determine the dominant asymptotic expression of (3.1). In this Appendix the result of the higher-order asymptotic terms is included along with a discussion regarding the behavior of the asymptotic solution at $\theta_2 = 0$. The final result for the dominant term, which is commonly referred to as the Fresnel reflection result, takes the following form

23

$$_0\Pi^r_{1x} \sim I_0 \frac{2\cos\theta_2}{\cos\theta_2 + \sqrt{\kappa - \sin^2\theta_2}} \frac{e^{-jk_1r_2}}{4\pi r_2} \quad . \tag{3.3}$$

Similarly, one can determine the asymptotic expansion of Π^r_{1z} and $\frac{\partial}{\partial z}\Pi^r_{1z}$ from (2.41) and (2.43), respectively, to arrive at

$$\Pi^r_{1z} \sim 2I_0 \cos\phi_2 \sin\theta_2 \cos\theta_2 \frac{\cos\theta_2 - \sqrt{\kappa - \sin^2\theta_2}}{\kappa\cos\theta_2 + \sqrt{\kappa - \sin^2\theta_2}} \frac{e^{-jk_1r_2}}{4\pi r_2} \tag{3.4}$$

and

$$\frac{\partial}{\partial z}\Pi^r_{1z} \sim -jk_1 \cos\theta_2 \, \Pi^r_{1z} \quad . \tag{3.5}$$

The preceding results are valid when k_1r_2 is large and $\theta_2 < \theta_c < \pi/2$. For cases in which k_1r_2 is sufficiently large, one may extend the domain of (3.2) – (3.4) to $\theta_2 < \pi/2$ by noting that the contribution to the integral from the portion of the path near the branch points is of the second order [14].

3.2 Numerical Evaluation

A survey in the literature reveals that numerous attempts have been concentrated on the numerical evaluation of $_0\Pi^r_{1x}$ and Π^r_{1z}. Most of the available techniques are based on the application of Sommerfeld's integrals, given in (2.34) and (2.35). It is noted that the integrand of these integrals is highly oscillatory for large ρ_2 or z_2, and, therefore, special consideration must be given for an accurate evaluation of the integrals. In order to avoid the inaccuracy observed in the results when the pole of the integrand of (2.35) approaches the real axis (integration path), some authors [3,4,6] have deformed this path to one which first travels along the imaginary axis and then runs parallel to the real axis. Though on this new path the effect of the pole singularity will be decreased, nevertheless, the decay rate and the oscillatory nature of the integrand would not be

24

changed appreciably. It is worth mentioning that for solving the antenna problem, one has to evaluate $_0\Pi^r_{1x}$ and Π^r_{1z} repeatedly. Therefore, application of an accurate and efficient numerical technique is indeed of great importance.

In this section a novel numerical technique is presented for determining $_0\Pi^r_{1x}$ and Π^r_{1z} in a highly accurate and efficient manner. This technique is also advantageous to other available techniques as it can be easily related to the asymptotic results given in the previous section. In contrast to other techniques, $_0\Pi^r_{1x}$, Π^r_{1z} and $\frac{\partial}{\partial z}\Pi^r_{1z}$ are evaluated using their integral representations as given in (2.40), (2.41) and (2.43), respectively. Here, computational details are given only for $_0\Pi^r_{1x}$.

At first, $_0\Pi^r_{1x}$ from (2.40) is expressed in the form given in (3.1), then the integration path Γ is deformed to the steepest descent path (SDP) passing through $\xi = \theta_2$. Since in this deformation one has to guard against intercepting any of the branch points of $\sqrt{\kappa - \sin^2 \xi}$, the location of these branch points is derived as

$$\xi_b = \pm[\pi/2 \pm jLn(\sqrt{\kappa} + \sqrt{\kappa - 1})] \tag{3.6}$$

where, as before, $\kappa = \varepsilon_{2r}/\varepsilon_{1r}$. Taking region 1 as air and region 2 as a lossy ground with a relative dielectric constant ε_g and conductivity σ, one finds

$$\kappa = \varepsilon_g - j\frac{\sigma}{\omega\varepsilon_0} = \varepsilon_g - j18000(\sigma/f) \tag{3.7}$$

where σ and f are in mho/m and MHz, respectively. It is clearly evident that ξ_b is a function of frequency. For different sets of (ξ_g,σ) the location of the ξ_b's are plotted versus frequency in Fig. 3. In evaluating (2.41) and (2.43) care must also be exercised in locating the poles of their

25
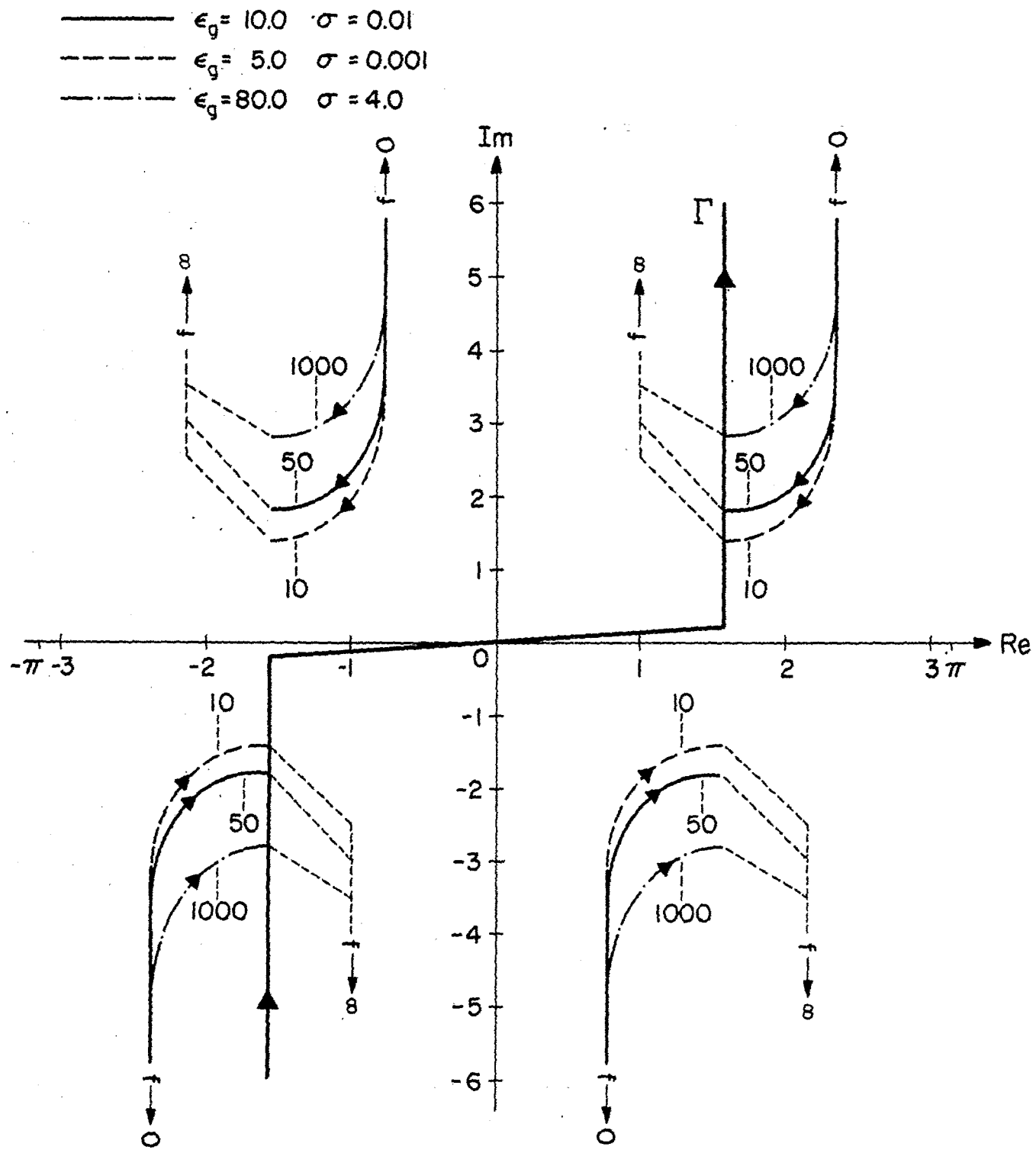
Figure 3. Branch point locations as a function of frequency for three sets
of ground parameters.

integrands. These poles are the roots of $\kappa \cos \xi + \sqrt{\kappa - \sin^2 \xi} = 0$, and a simple calculation allows one to express them as

$$\xi_p = \pm j \left\{ \text{Ln} \left(\pm 1 + j\sqrt{\kappa} \right) - \text{Ln} \left(\sqrt{\kappa + 1} \right) \right\} \tag{3.8}$$

The location of ξ_p's versus frequency for different choices of (ε_g, σ) are shown in Fig. 4 .

Assuming that no poles or branch points are intercepted, one deforms the integration path Γ into the steepest descent path (SDP) defined by $\text{Re}[\cos (\xi - \theta_2)] = 1$. On this path, the following change of variable is introduced

$$\cos (\xi - \theta_2) = 1 - jt^2 \tag{3.9}$$

allowing one to finally express (3.1) as

$$_0\Pi^r_{1x} = \frac{I_0 k_1}{2\sqrt{2\pi}} e^{-jk_1 r_2 - j\pi/4} \int_{-\infty}^{\infty} Q(t) e^{-k_1 r_2 t^2} dt \tag{3.10a}$$

where

$$Q(t) = P(\xi) \sec \frac{\xi - \theta_2}{2} \tag{3.10b}$$

in which ξ is replaced by

$$\xi = \pm \left[\frac{\pi}{2} + j\text{Ln} \left(t^2 + j + |t| \sqrt{t^2 + 2j} \right) \right] + \theta_2 \ ; \quad t \gtrless 0 \quad . \tag{3.11}$$

Expression (3.11) is used to construct a universal plot for steepest descent path (SDP) in the complex plane ξ with θ_2 as a parameter. This plot is depicted in Fig. 5 , and can be used in conjunction with Figs. 3,4 to determine the critical angle θ_c, beyond which (3.10a) would not hold in general. For $\theta_2 = 0$, $P(\xi)$ from (3.2) diverges and therefore, (3.10a) is not defined. To circumvent the difficulty, one can use the result of
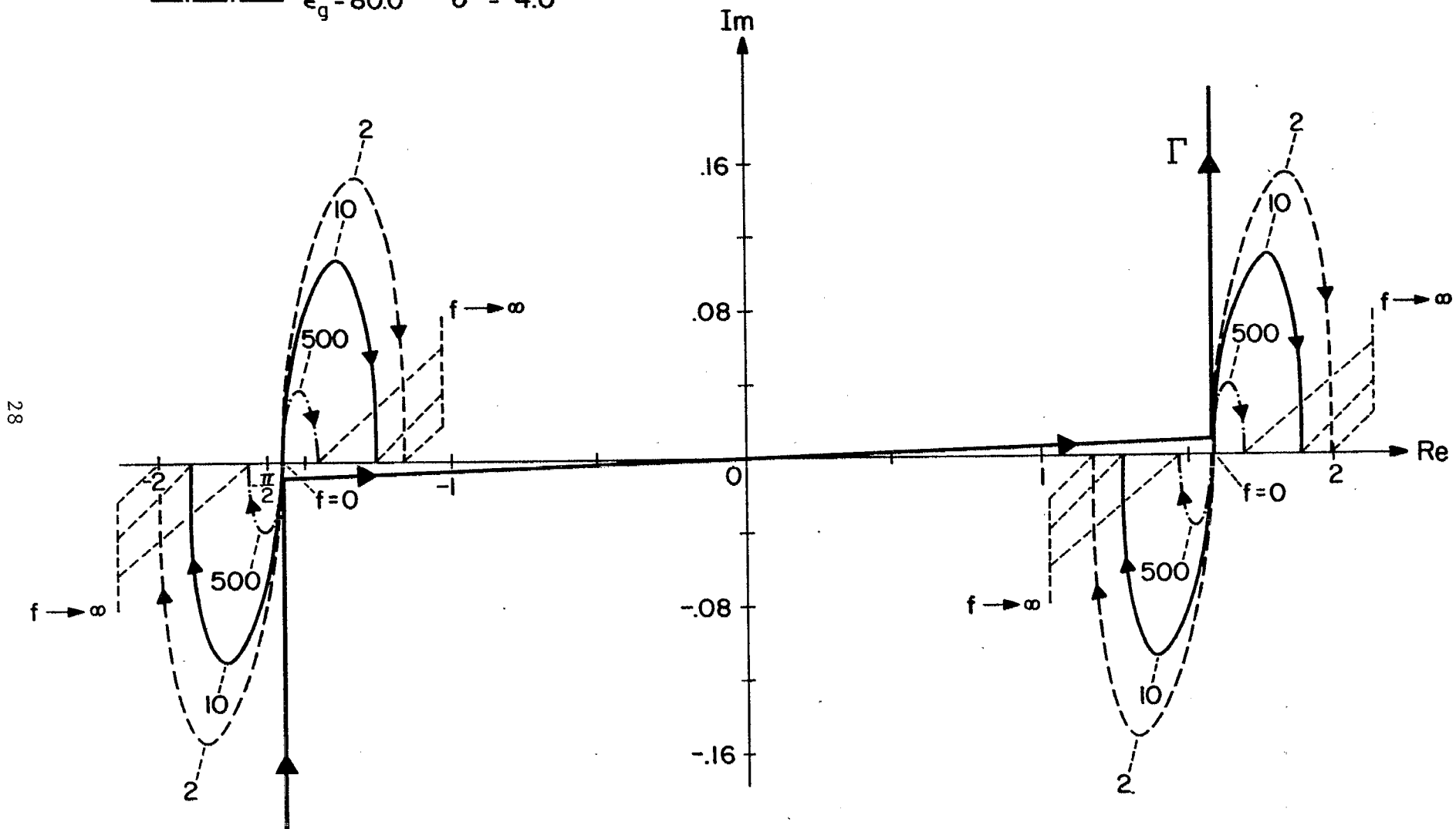
Figure 4. Pole locations as a function of frequency, for three sets of ground parameters.
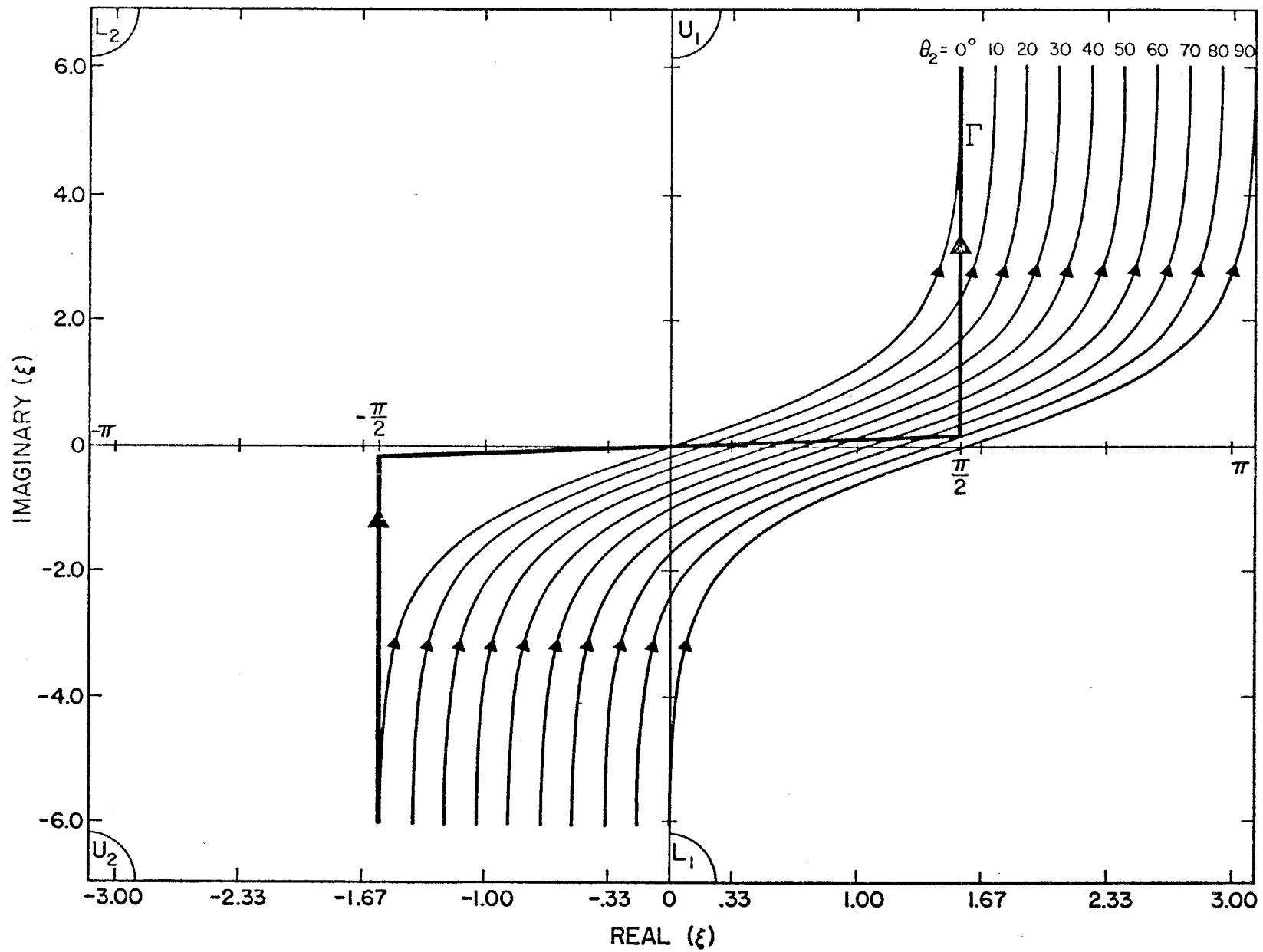
Figure 5. The steepest descent path (SDP) as a function of θ_2. The condition $\text{Im}(\cos \xi) < 0$ is satisfied in the U_1 and U_2 regions.

Appendix II to rewrite (3.10a) in a more suitable fashion by employing $P(\xi)$ as

$$P(\xi) = \frac{\sin \xi \cos \xi}{\cos \xi + \sqrt{\kappa - \sin^2 \xi}} \frac{-2j}{\pi} \text{Ln}(k_1 r_2 \sin \xi) \ , \quad \text{for } \theta_2 = 0 \ . \qquad (3.12)$$

Clearly for $\theta_2 = 0$ and $\xi = 0$, one obtains $P(\xi) = 0$. This fact can be used when evaluating the integrand of (3.10a) for $\theta_2 = 0$ and $t = 0$.

Similarly, one can construct integral representations in the form (3.10a) for both Π_{1z}^r and $\frac{\partial}{\partial z} \Pi_{1z}^r$. Using (2.41) and (2.43), one finds that

$$\left\{ \begin{array}{c} \Pi_{1z}^r \\ \\ \frac{\partial}{\partial z} \Pi_{1z}^r \end{array} \right\} = \frac{I_0 k_1}{2\sqrt{2}\pi} e^{-jk_1 r_2 - j\pi/4} \cos \phi_2 \int_{-\infty}^{\infty} \left\{ \begin{array}{c} Q_1(t) \\ \\ Q_2(t) \end{array} \right\} e^{-k_1 r_2 t^2} dt \qquad (3.13a)$$

where

$$\left\{ \begin{array}{c} Q_1(t) \\ \\ Q_2(t) \end{array} \right\} = \left\{ \begin{array}{c} -j \\ \\ -k_1 \cos \xi \end{array} \right\} \sin^2 \xi \cos \xi \ \frac{\cos \xi - \sqrt{\kappa - \sin^2 \xi}}{\kappa \cos \xi + \sqrt{\kappa - \sin^2 \xi}}$$

$$\cdot H_1^{(2)} (k_1 r_2 \sin \theta_2 \sin \xi) e^{jk_1 r_2 \sin\theta_2 \sin\xi} \sec \frac{\xi - \theta_2}{2} \ ,$$

$$(3.13b)$$

and ξ is replaced with t from (3.11). Though at $\theta_2 = 0$, the preceding expression diverges, nevertheless, the result of the integration is bounded and as observed from (2.35) would be zero.

For a sufficiently large $k_1 r_2$, integrations (3.10a) and (3.13b) can be asymptotically evaluated to give the results obtained in Section 3.1. For other values of $k_1 r_2$ one has to evaluate these integrals numerically. In order to demonstrate the accuracy achieved in the numerical integration,

the integrands of the aforementioned integrals are plotted as a function of t for different values of $k_1 r_2$ and θ_2 in Figs. 6 - 17. For this evaluation, a newly developed routine for the computation of the Hankel functions with complex argument was used [15]. The plots of the integrands clearly demonstrate that these integrands decay very rapidly with relatively smooth behavior. Due to these observations, integrations (3.11a) and (3.13a) can be evaluated very accurately and efficiently by employing the Gaussian quadrature integration algorithm. Also in Figs. 18 - 19, the integration results are compared with the corresponding asymptotic values for a wide range of frequencies. Note that the difference error between the exact and the symptotic evaluations of the vector potentials vanishes rapidly as the frequency is increased, and for the examples in Figs. 18, 19, the error is consistently below 5% for frequencies above 60 MHz.

The computation time on a CDC-CYBER-175 digital computer is less than 1000 μs for an asymptotic evaluation, for a given point on Figs. 18 and 19, and about 35 ms for the integration result using a 50 point Gaussian quadrature approximation. Even though the integration time is improved by that of reported in [13], the computation time can be further reduced by relaxing the number of points needed for the integral evaluation since, as seen in Figs. 6-17, the integrands are smooth and well behaved.

31
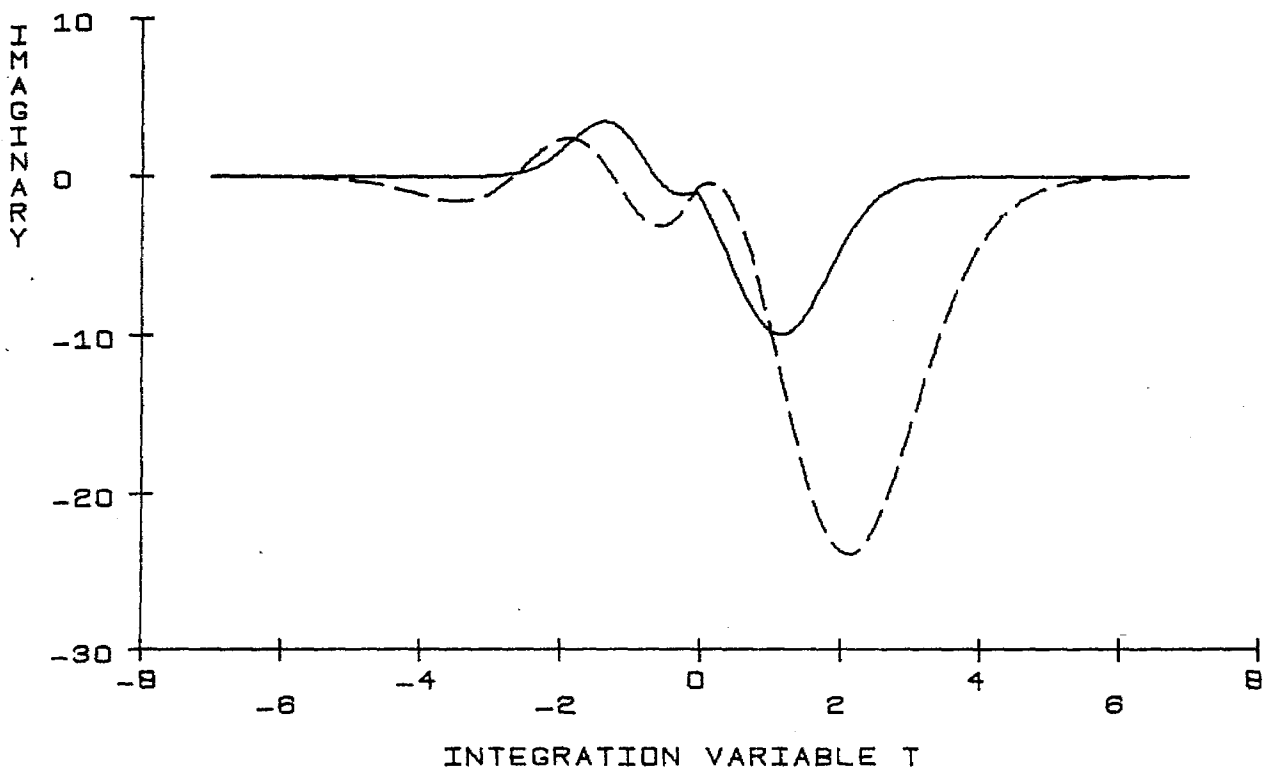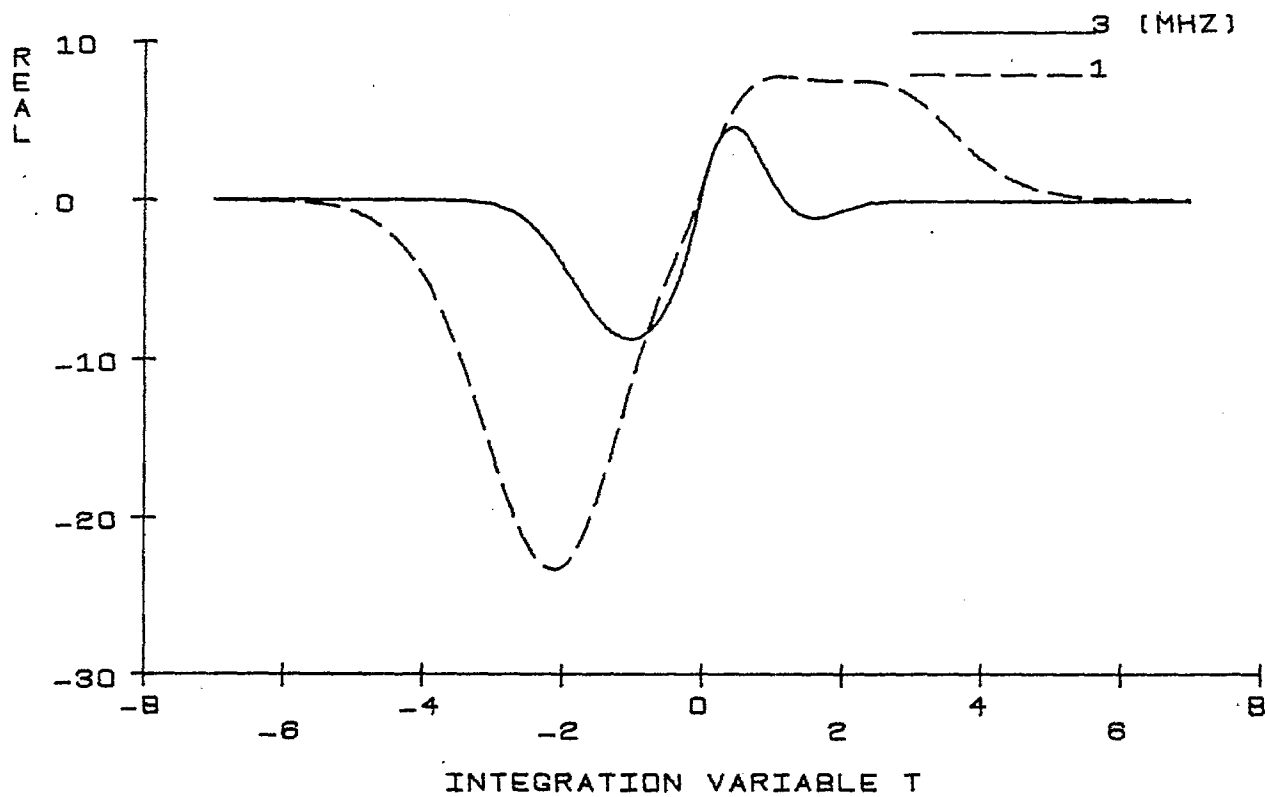
Figure 6. Low frequency examples of the $_0\Pi_{1x}$ integrand. For these cases, $\theta_2 = 5°$, h = 5m, $\varepsilon_g = 10.$, and $\sigma = .01$ mhos/m.

32
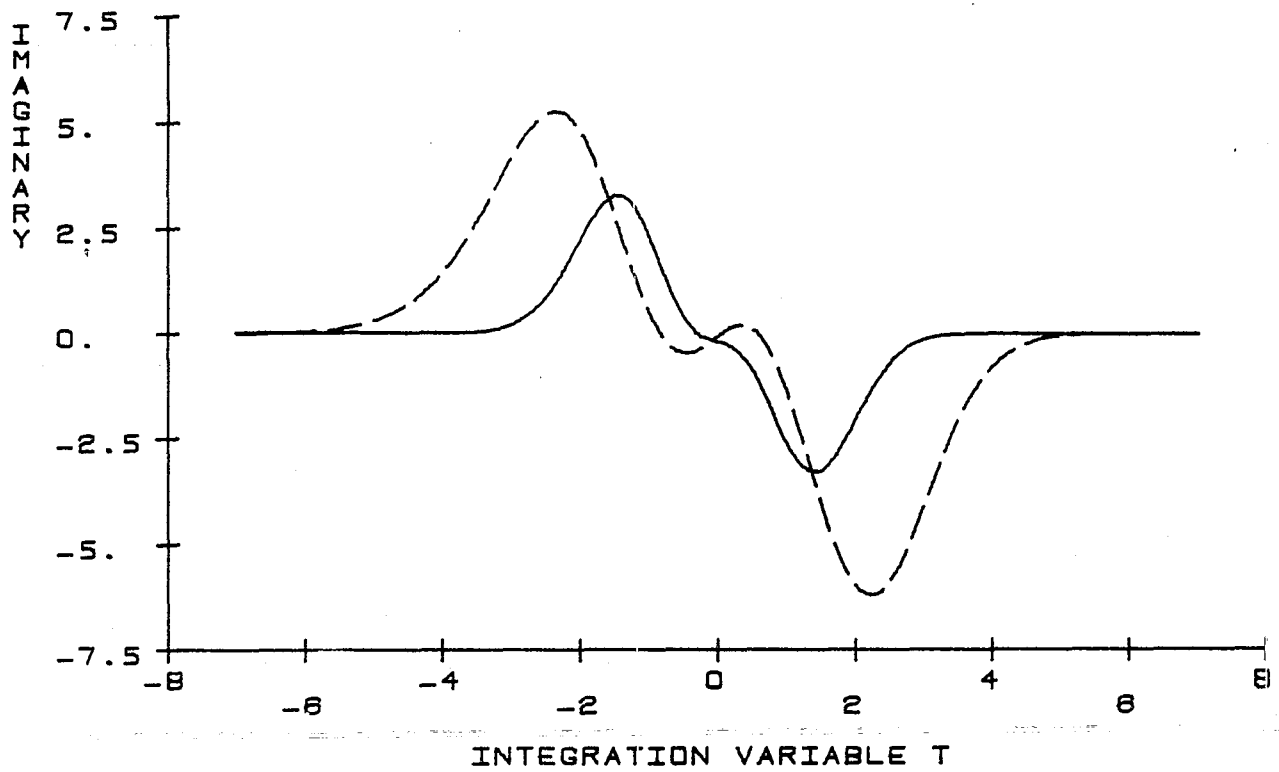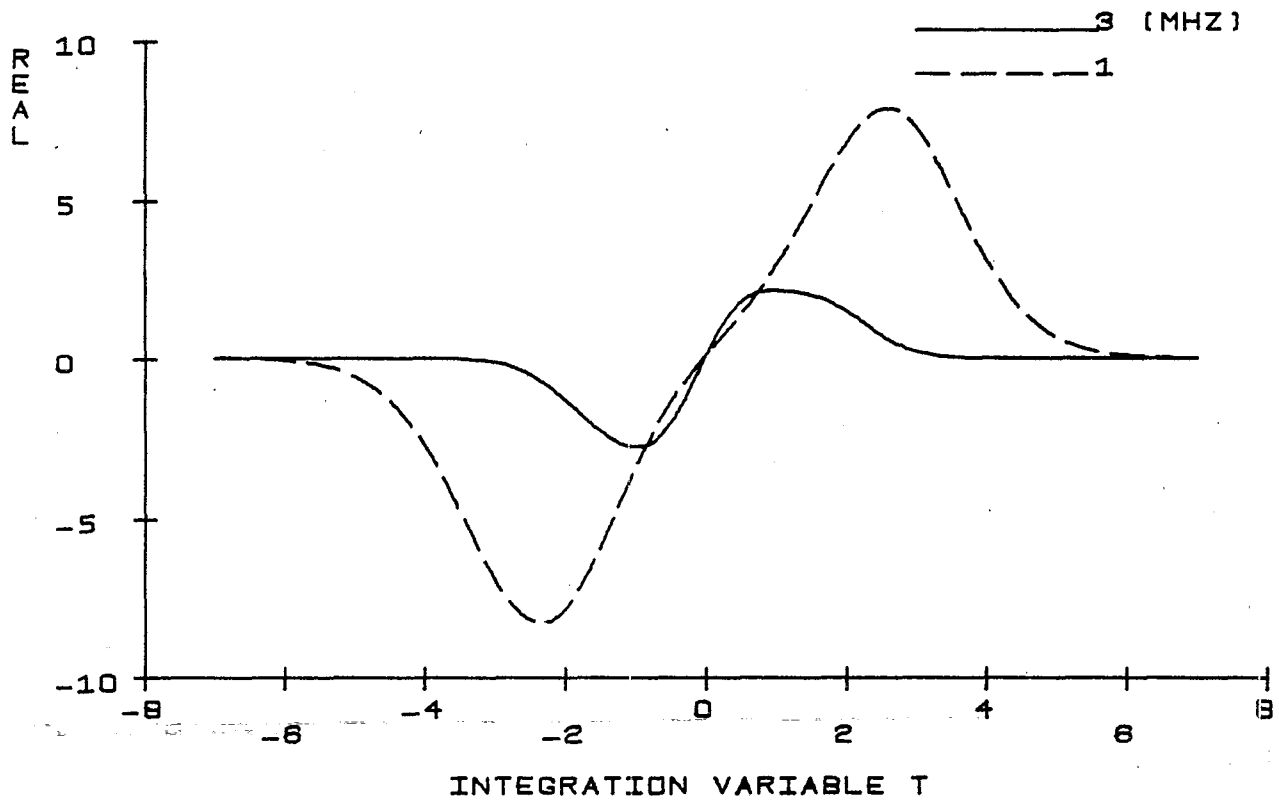
Figure 7.   Low frequency examples of the $\partial_z \Pi^r_{1z}$ integrand.   For these cases, $\theta_2 = 5°$, $h = 5m$, $\varepsilon_g = 10.$, and $\sigma = .01$ mhos/m.

33
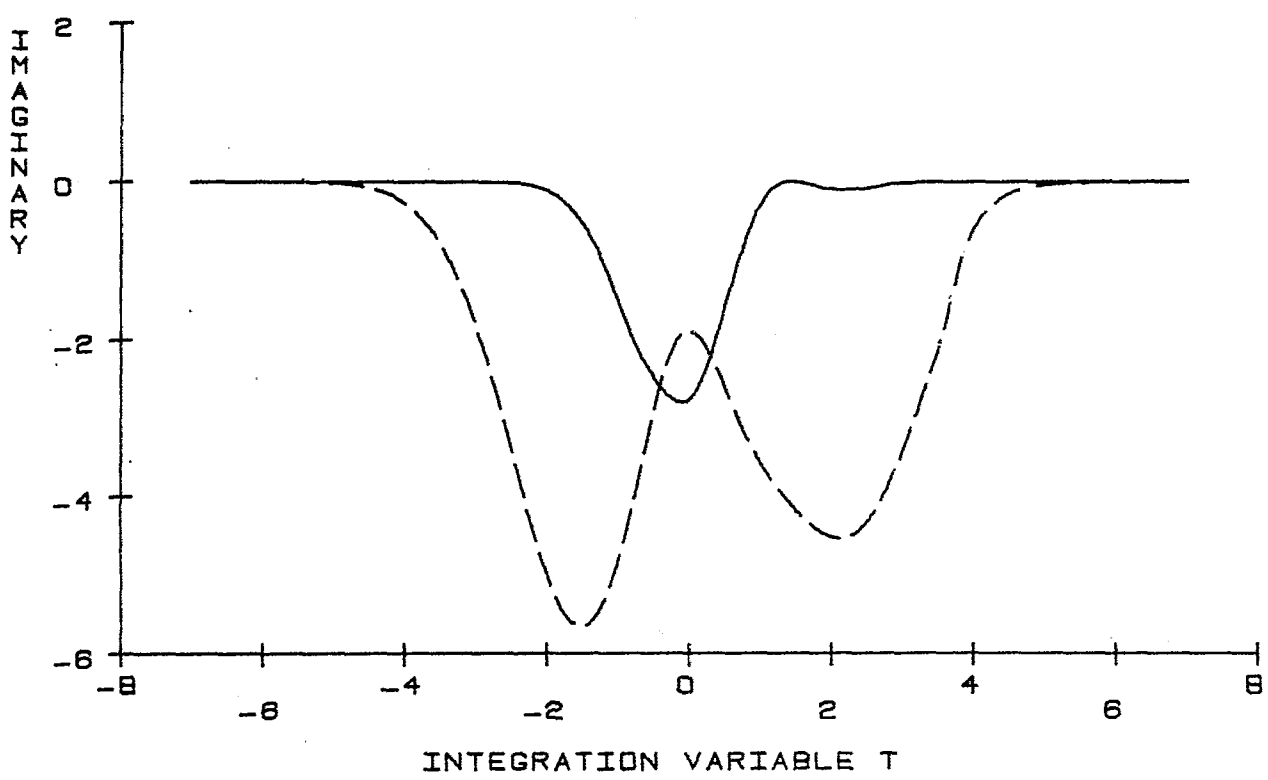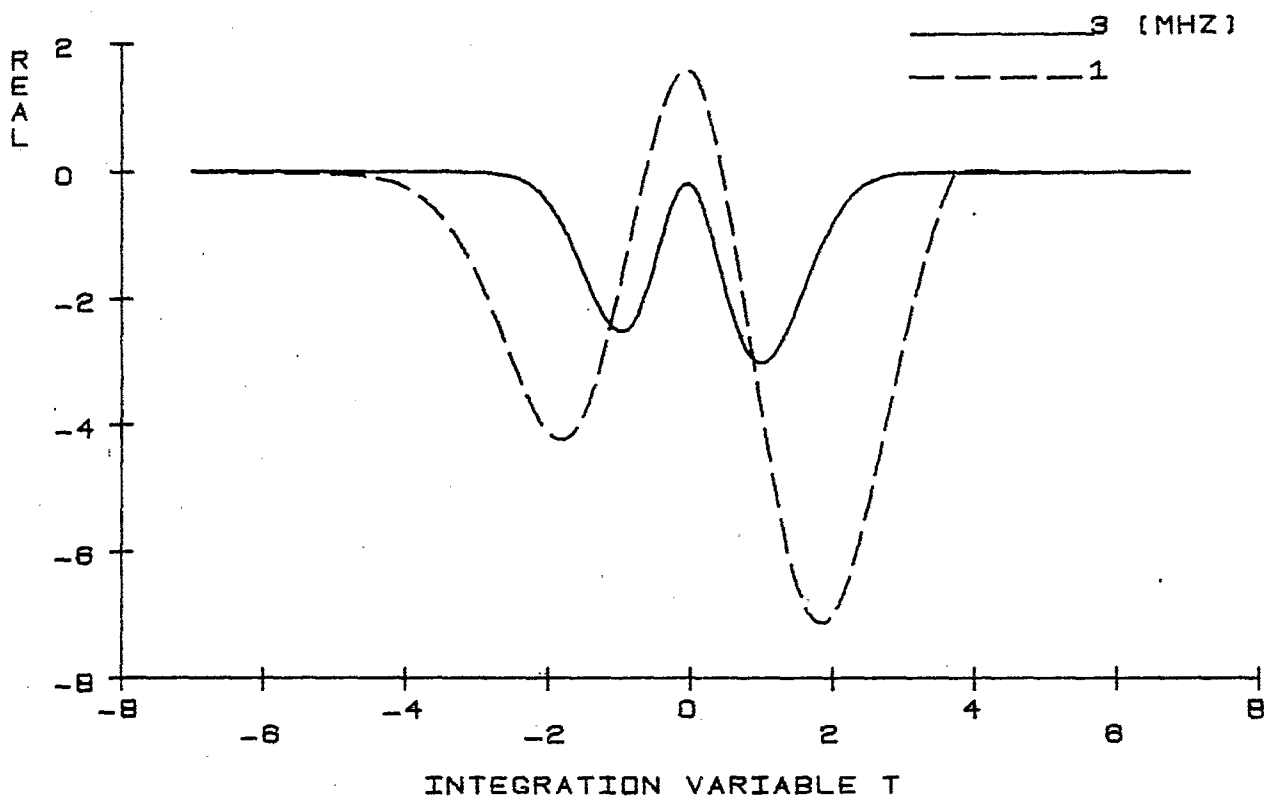
Figure 8. Low frequency examples of the $_0\Pi_{1x}^r$ integrand. For these cases, $\theta_2 = 45°$, h = 5m, ε_g = 10, and $\sigma \approx$ .01 mhos/m.
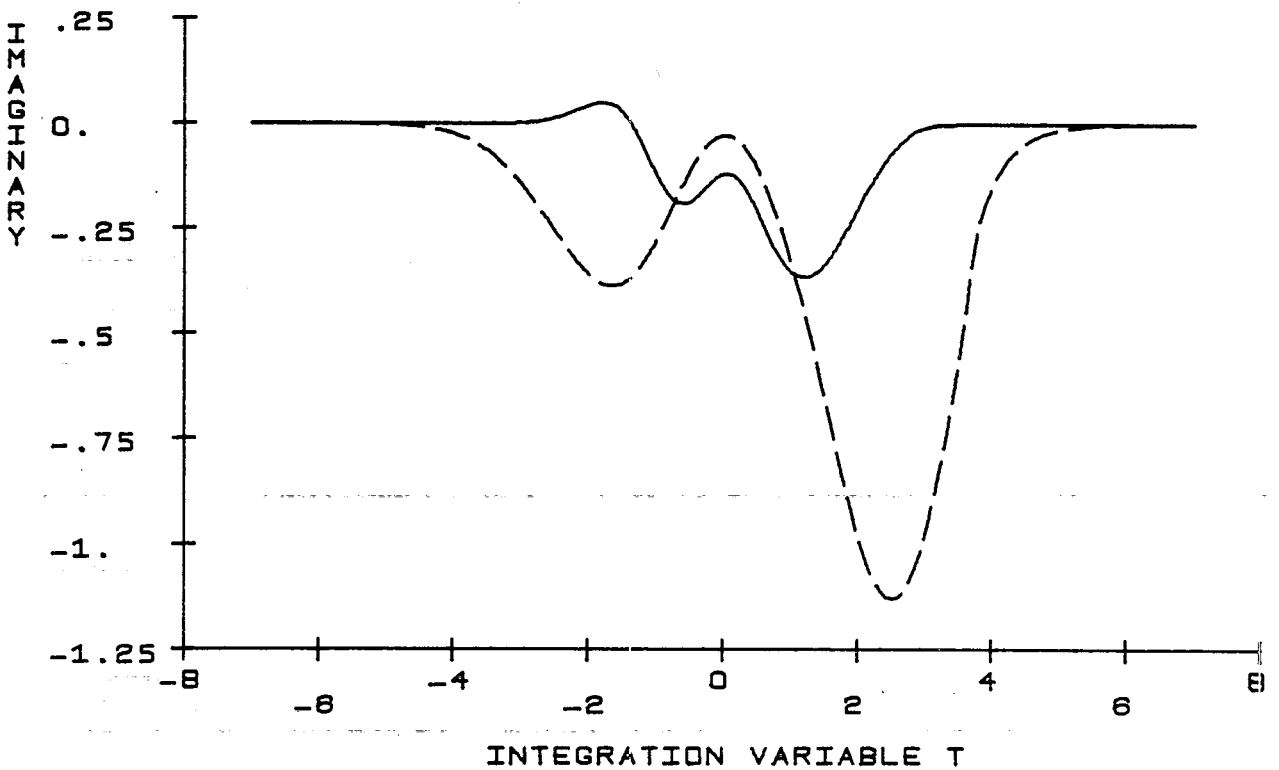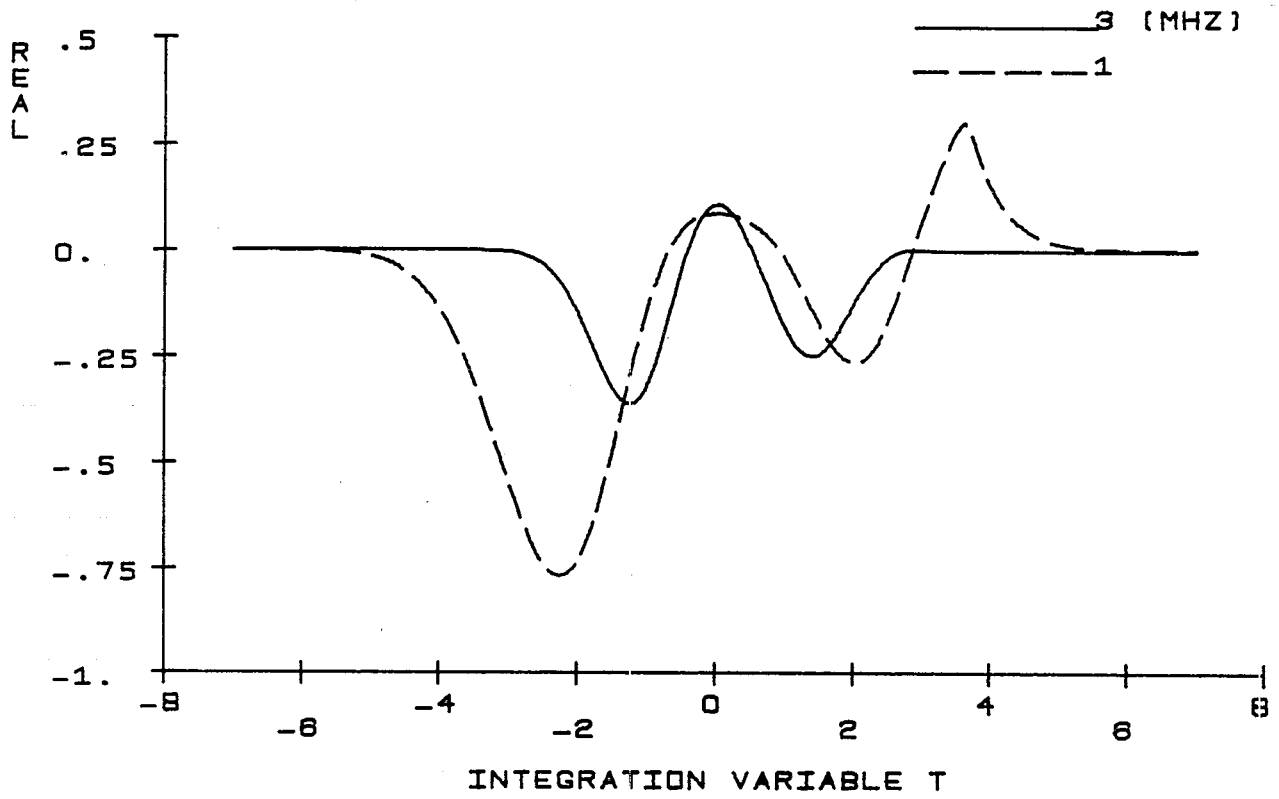
Figure 9. Low frequency examples of the $\partial_z \Pi_{1z}^r$ integrand. For these cases, $\theta_2 = 45°$, $h = 5m$, $\varepsilon_g = 10$, and $\sigma = .01$ mhos/m.
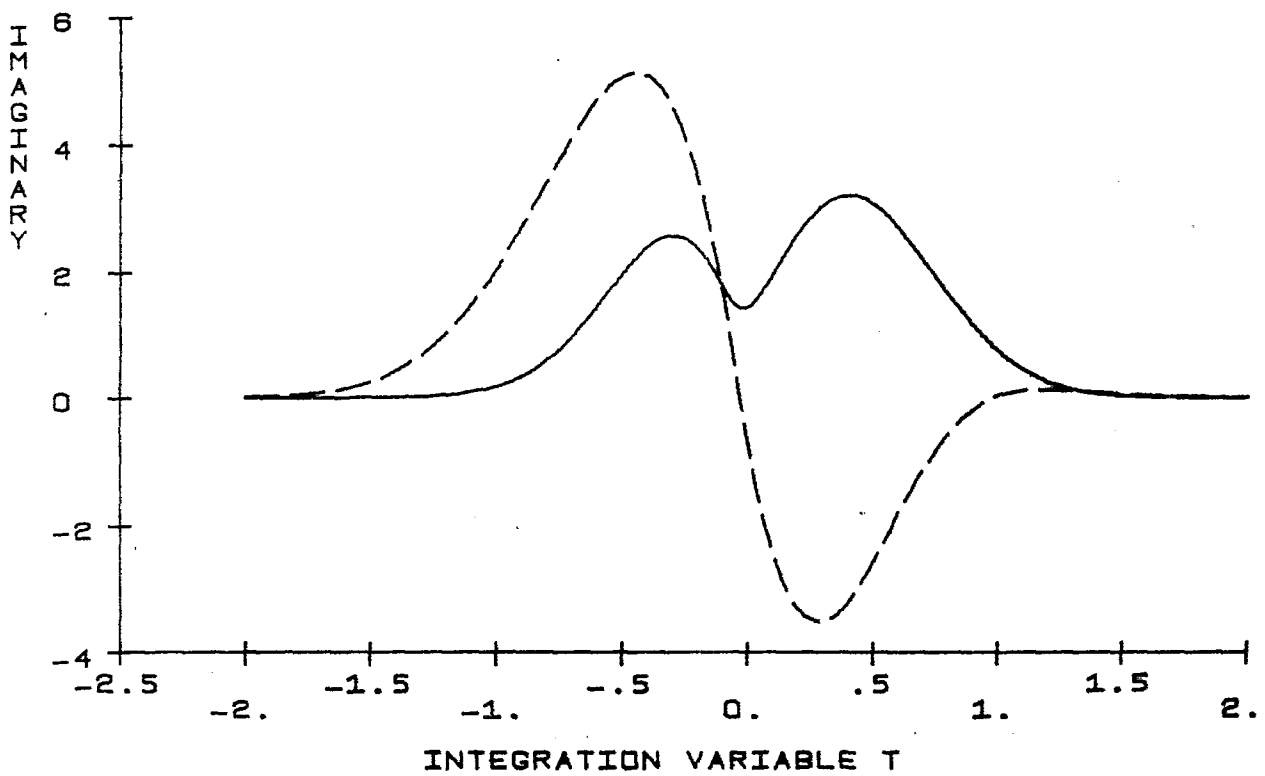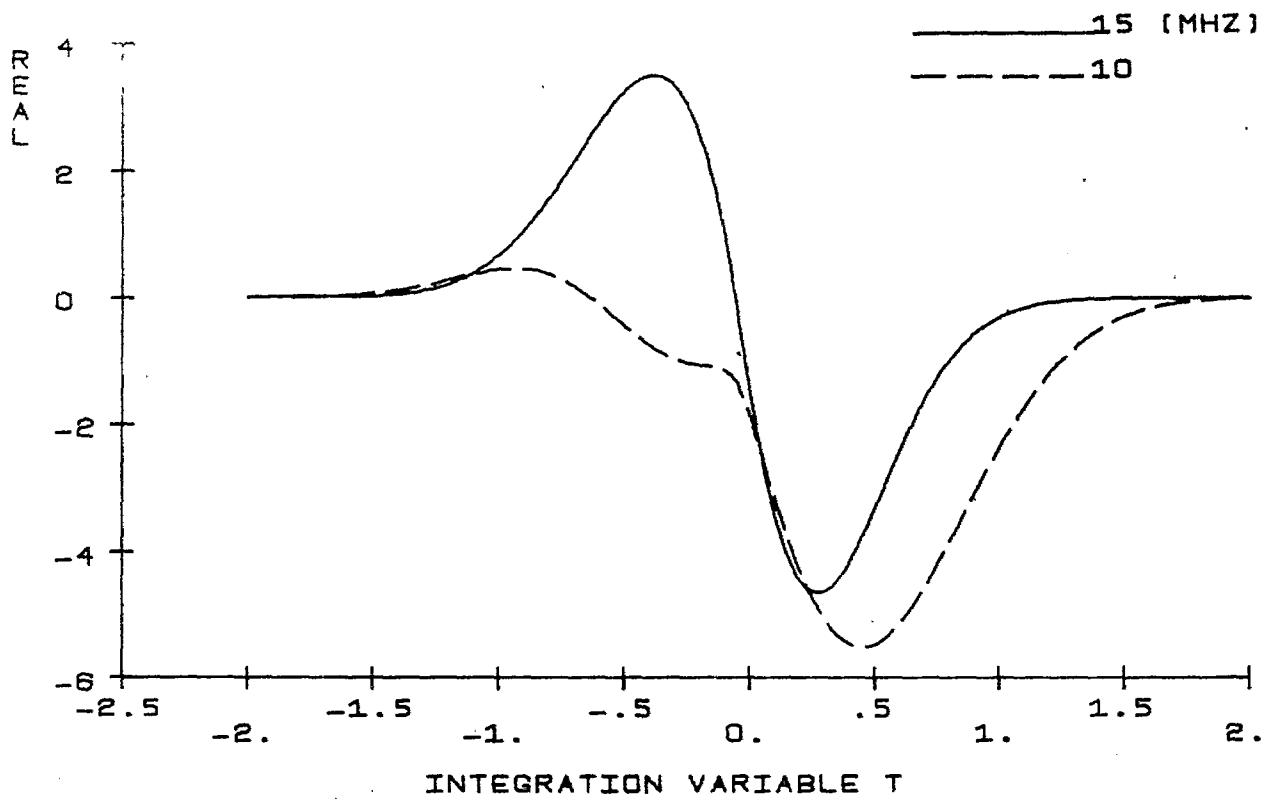
Figure 10. Mid frequency examples of the $_0\Pi_{1x}^r$ integrand. For these cases, $\theta_2 = 5°$, h = 5m, $\varepsilon_g = 10$, and $\sigma = .01$ mhos/m.

36
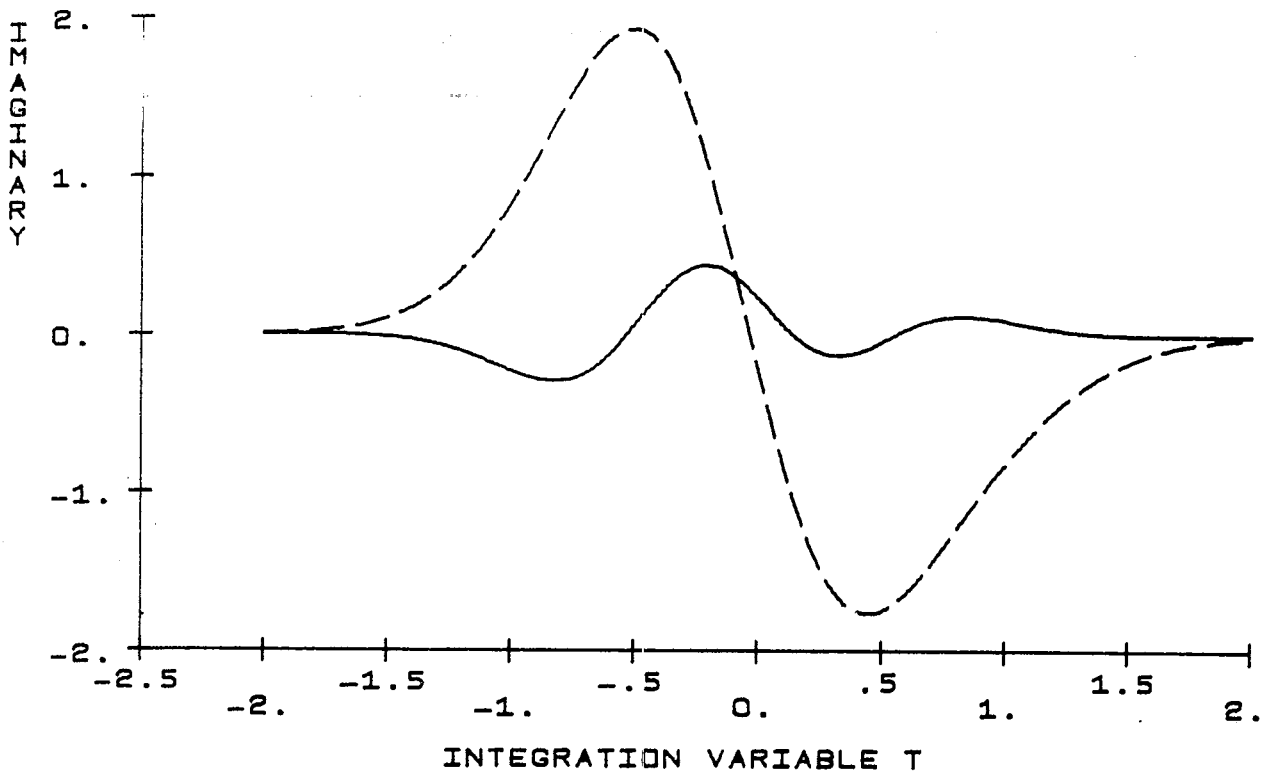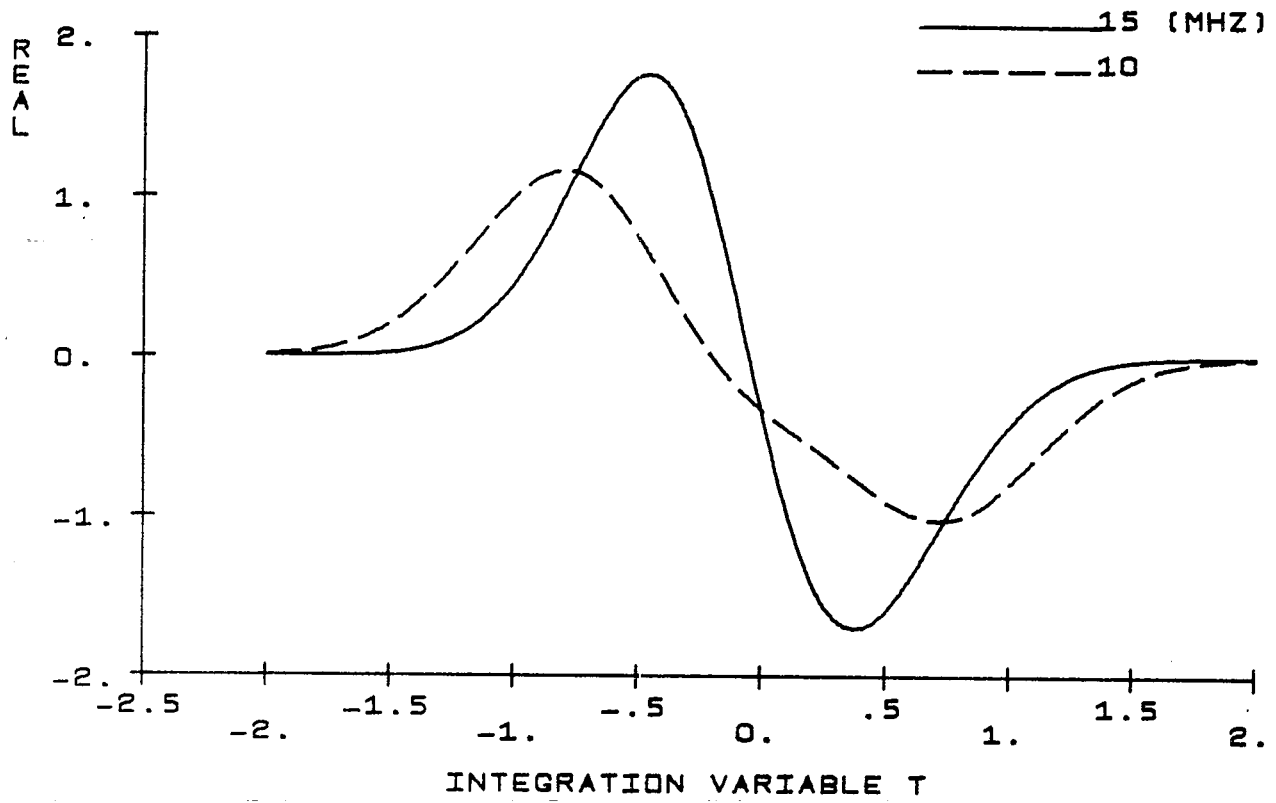
Figure 11. Mid frequency examples of the $\partial_z \Pi_{1z}^r$ integrand. For these cases, $\theta_2 = 5°$, h = 5m, ε_g = 10, and σ = .01 mhos/m.
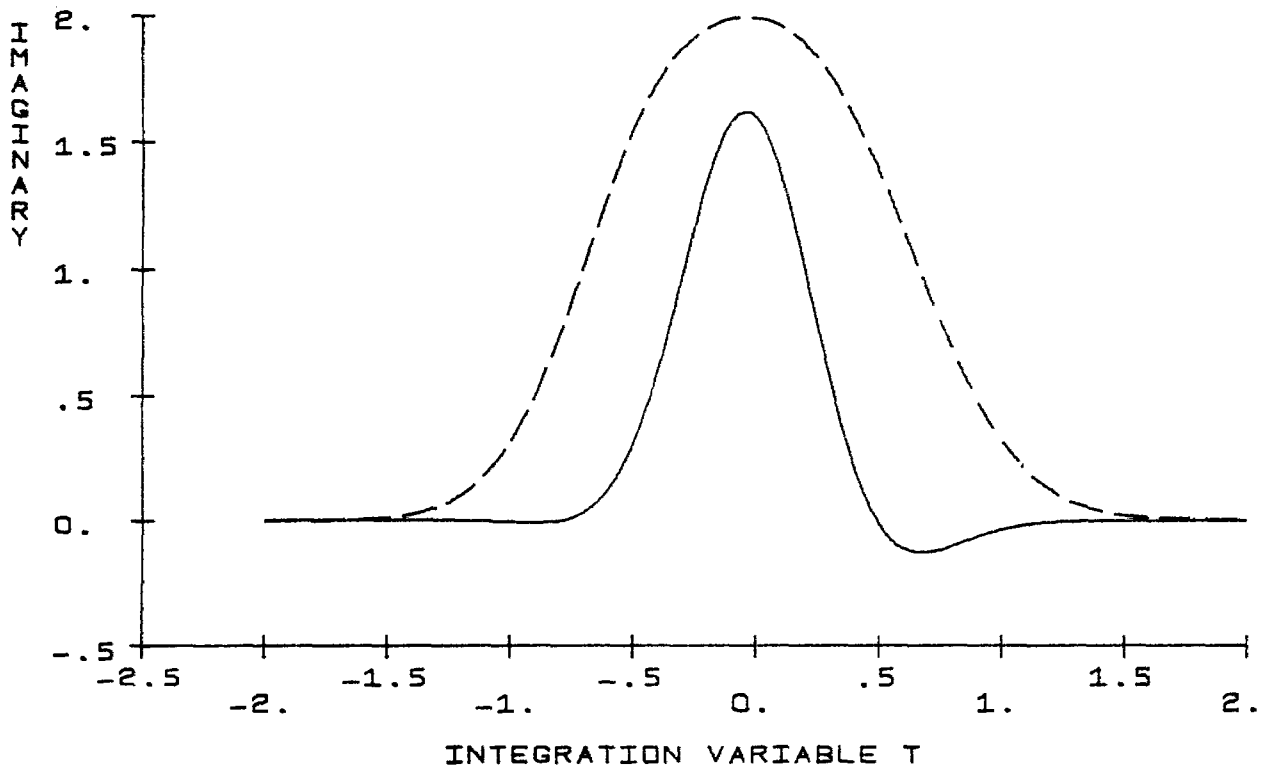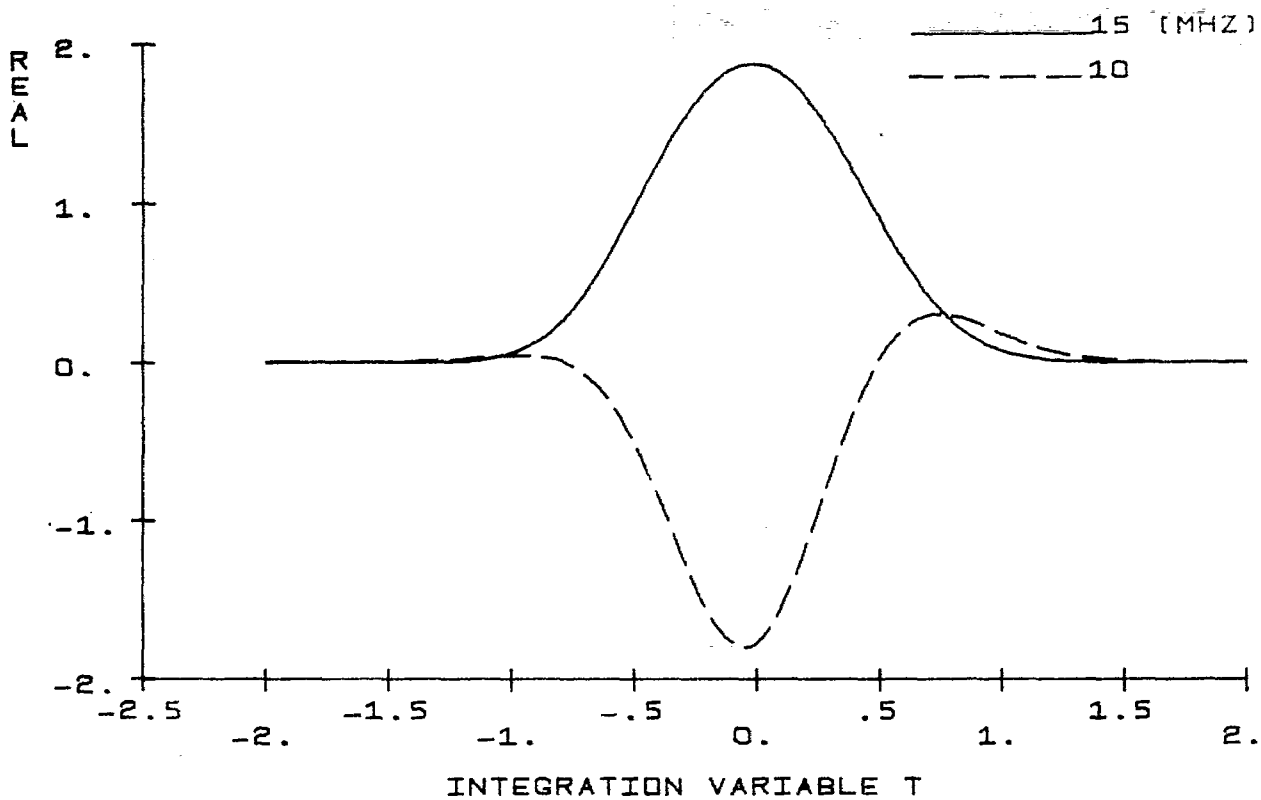
Figure 12. Mid frequency examples of the $_0\Pi^r_{1x}$ integrand. For these cases, $\theta_2 = 45°$, h = 5m, $\varepsilon_g = 10$, and $\sigma = .01$ mhos/m.
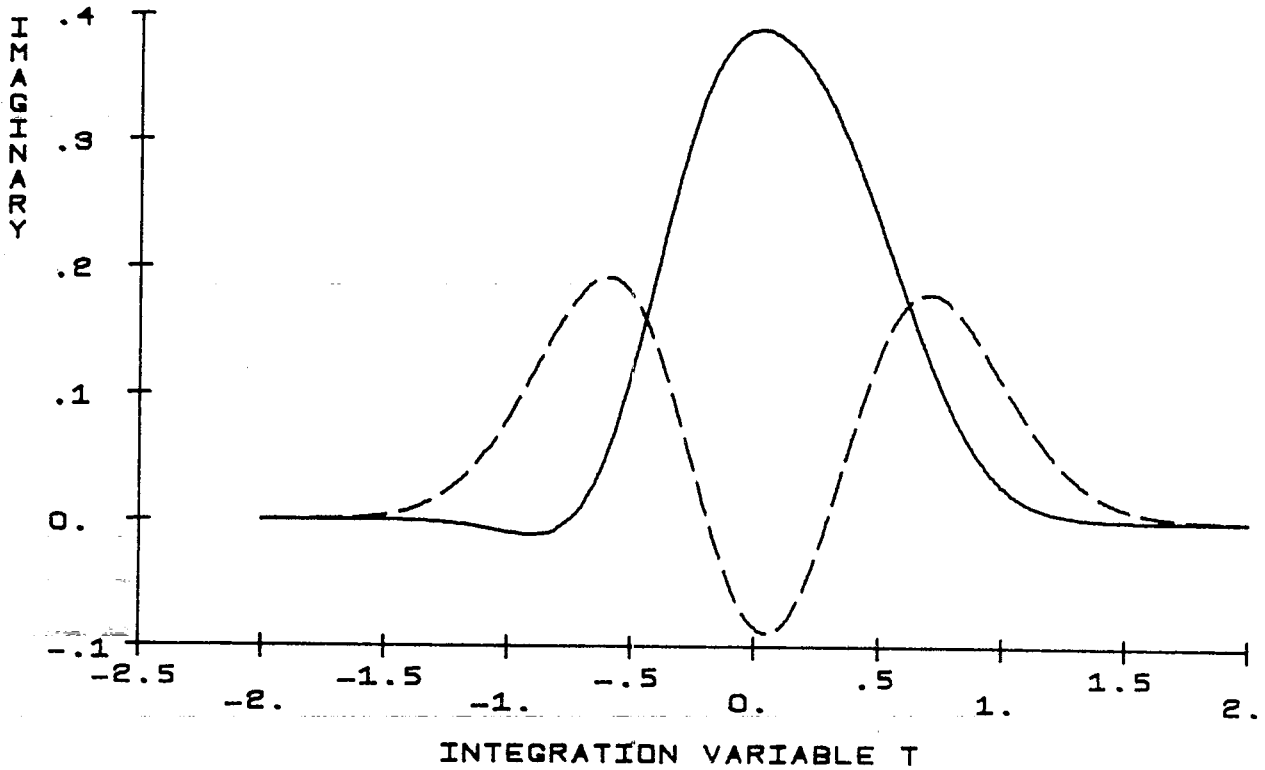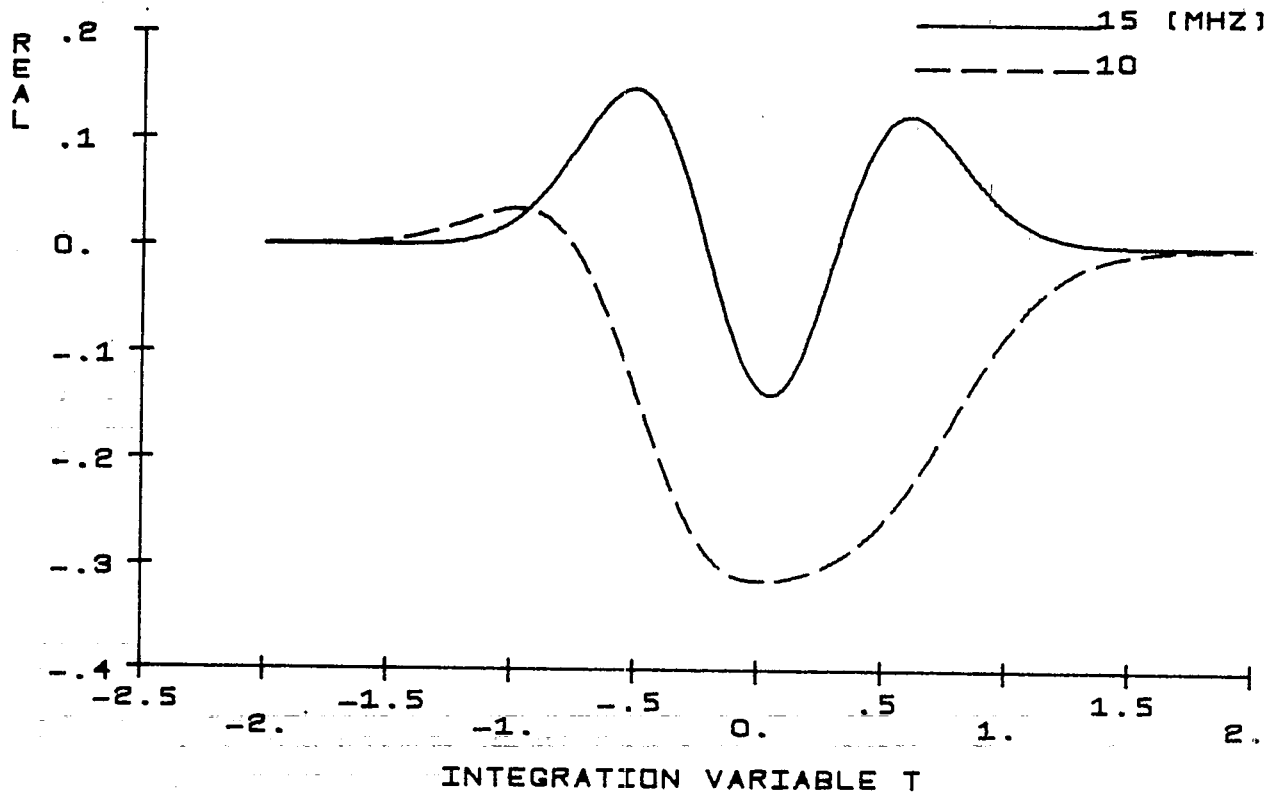
Figure 13. Mid frequency examples of the $\partial_z \Pi_{1z}^r$ integrand. For these cases, $\theta_2 = 45°$, $h = 5m$, $\varepsilon_g = 10$, and $\sigma = .01$ mhos/m.

39
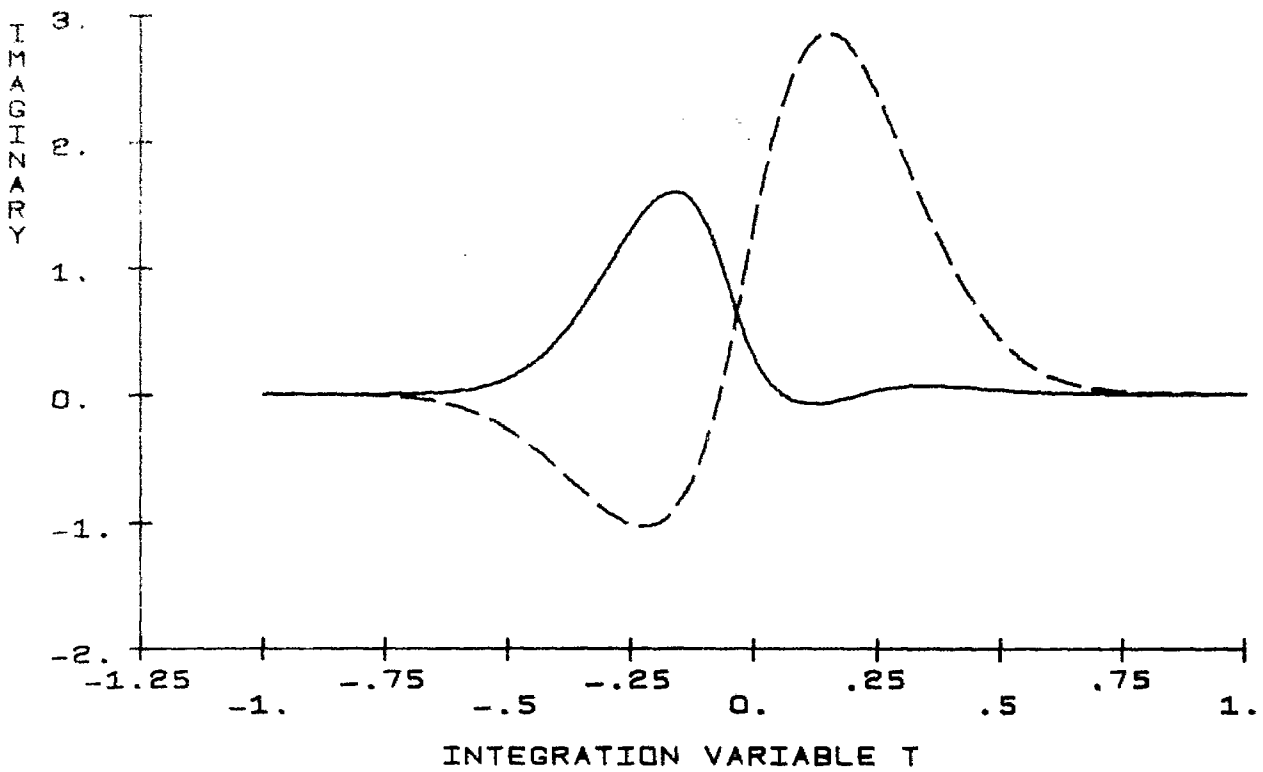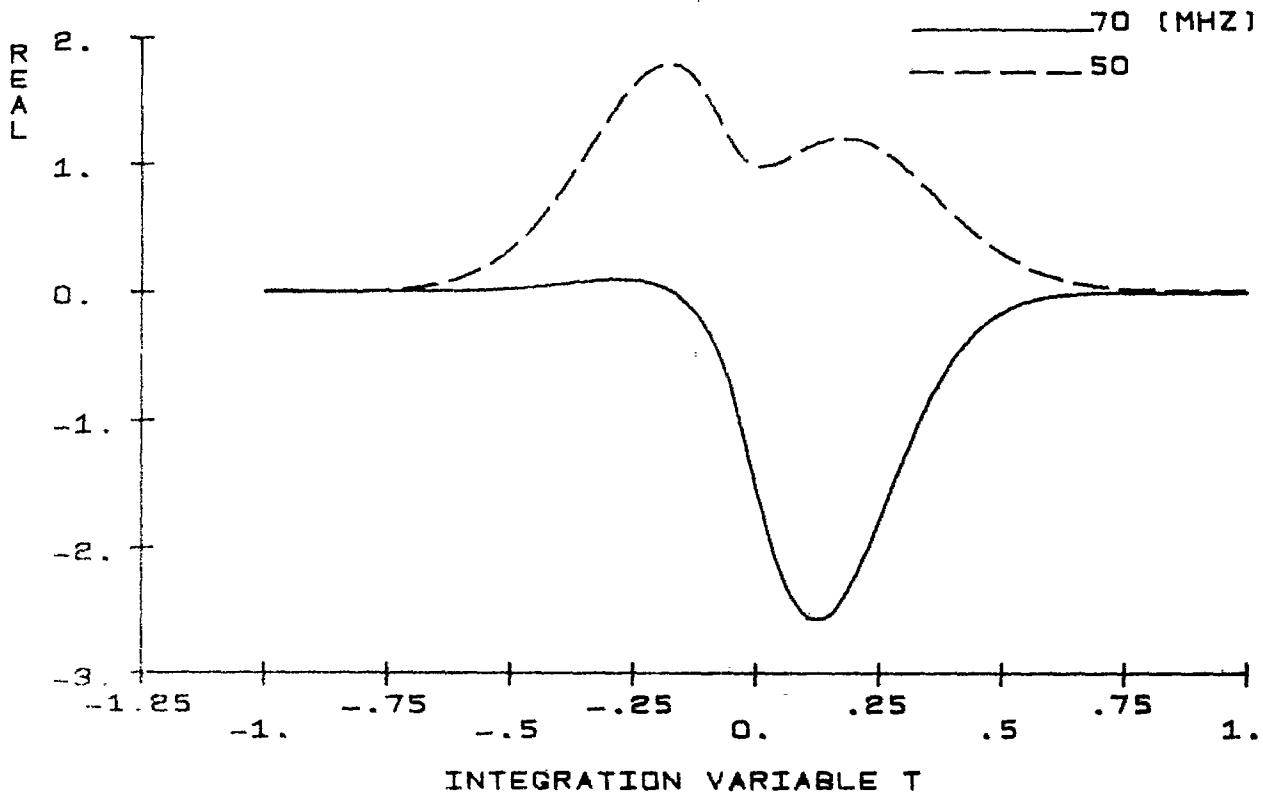
Figure 14. High frequency examples of the $\Pi^r_{0_{1x}}$ integrand. For these cases, $\theta_2 = 5°$, h = 5m, $\varepsilon_g = 10$, and $\sigma_0 = .01$ mhos/m.
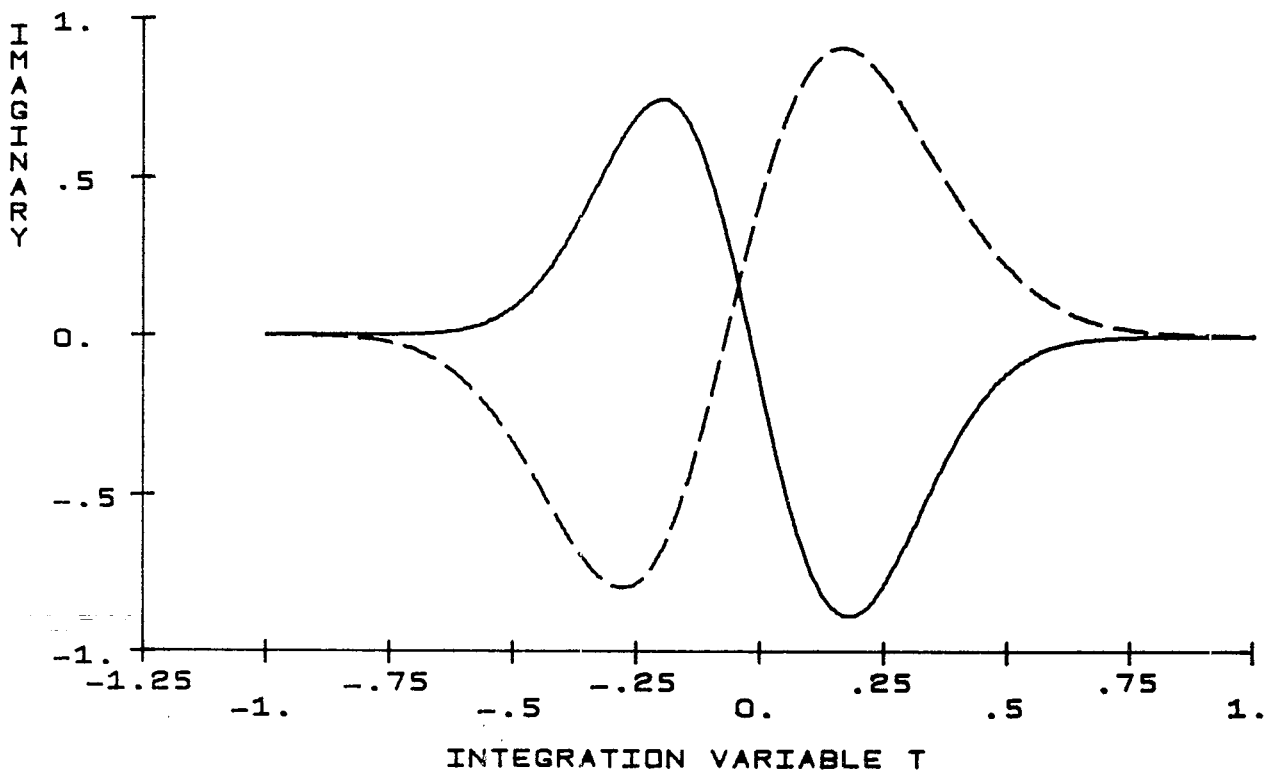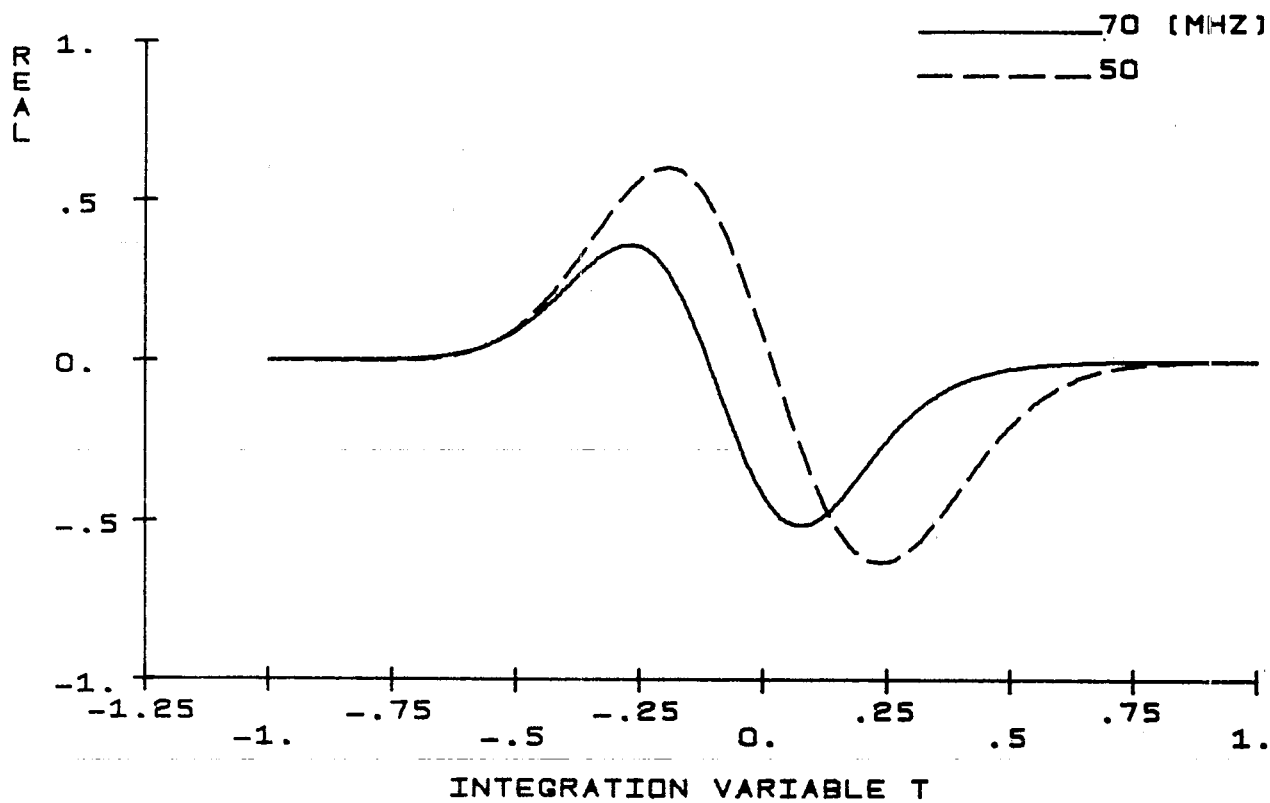
Figure 15. High frequency examples of the $\partial_z \Pi^r_{1z}$ integrand. For these cases, $\theta_2 = 5°$, h = 5m, ε_g = 10, and σ = .01 mhos/m.

41
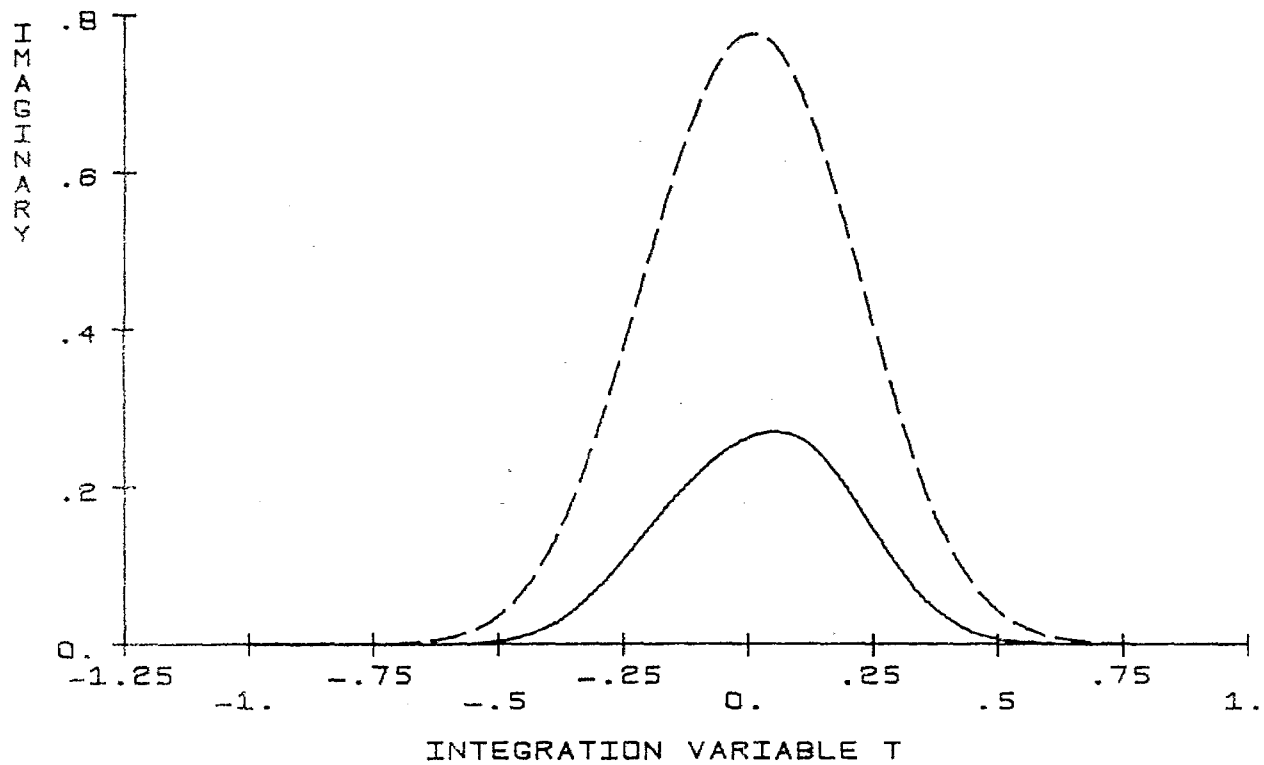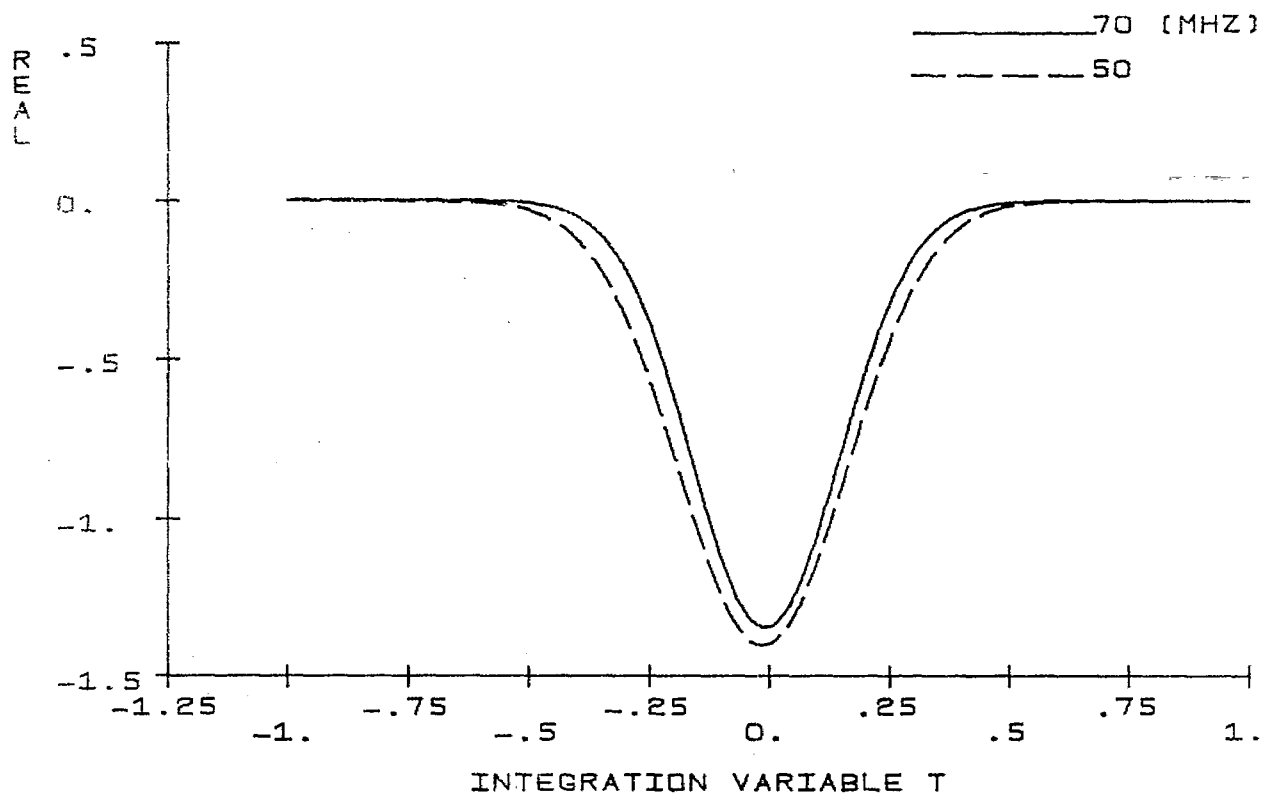
Figure 16. High frequency examples of the Π^r_{1x} integrand. For these cases $\theta_2 = 45°$, h = 5m, $\varepsilon_g = 10$, and $\sigma = .01$ mhos/m.

42
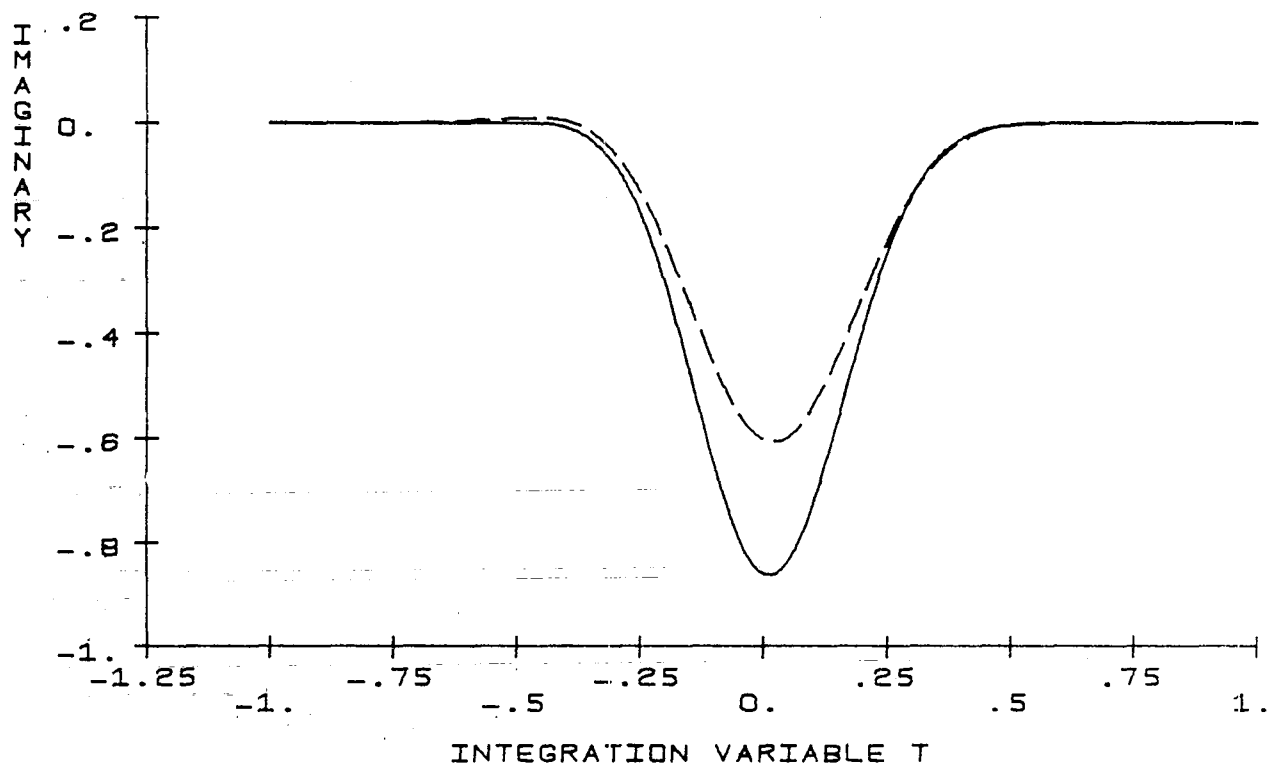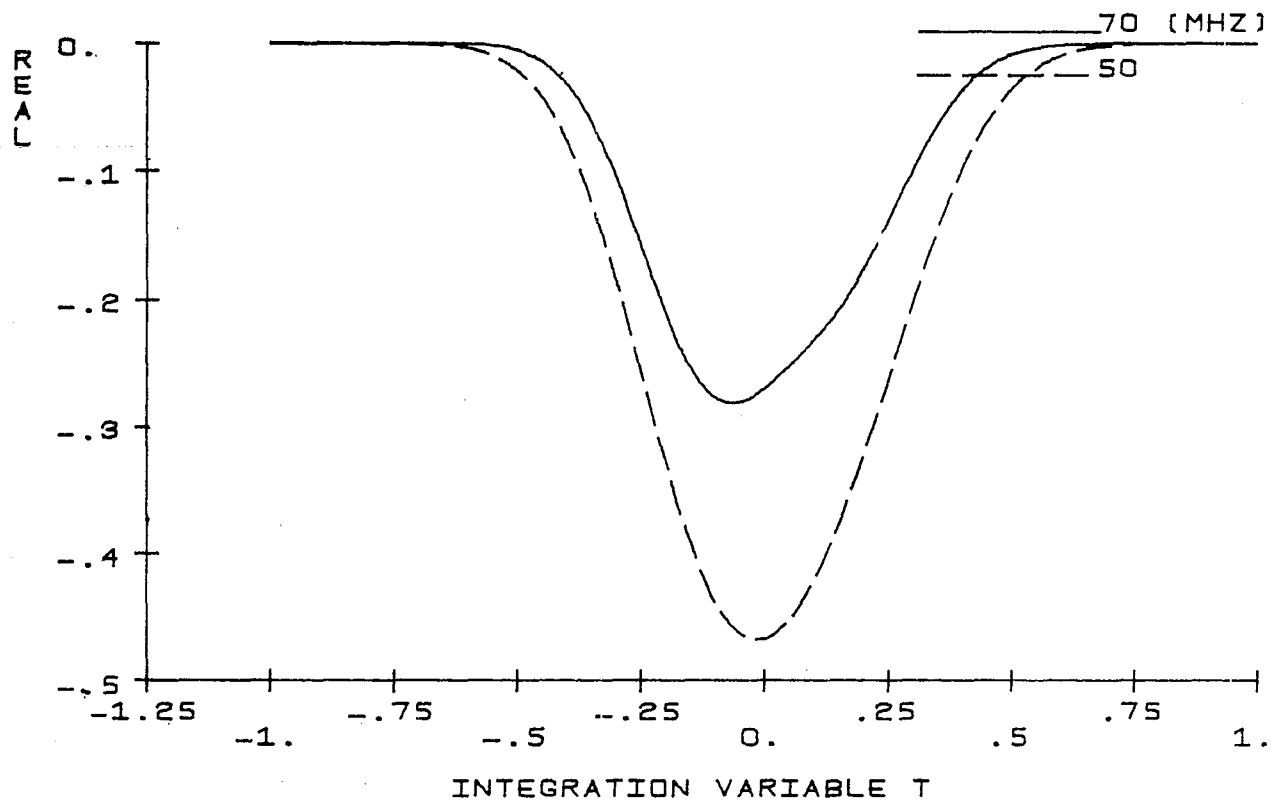
Figure 17. High frequency examples of the $\partial_z \Pi_{1z}^r$ integrand. For these cases, $\theta_2 = 45°$, h = 5m, ε_g = 10, and $\sigma = .01$ mhos/m.
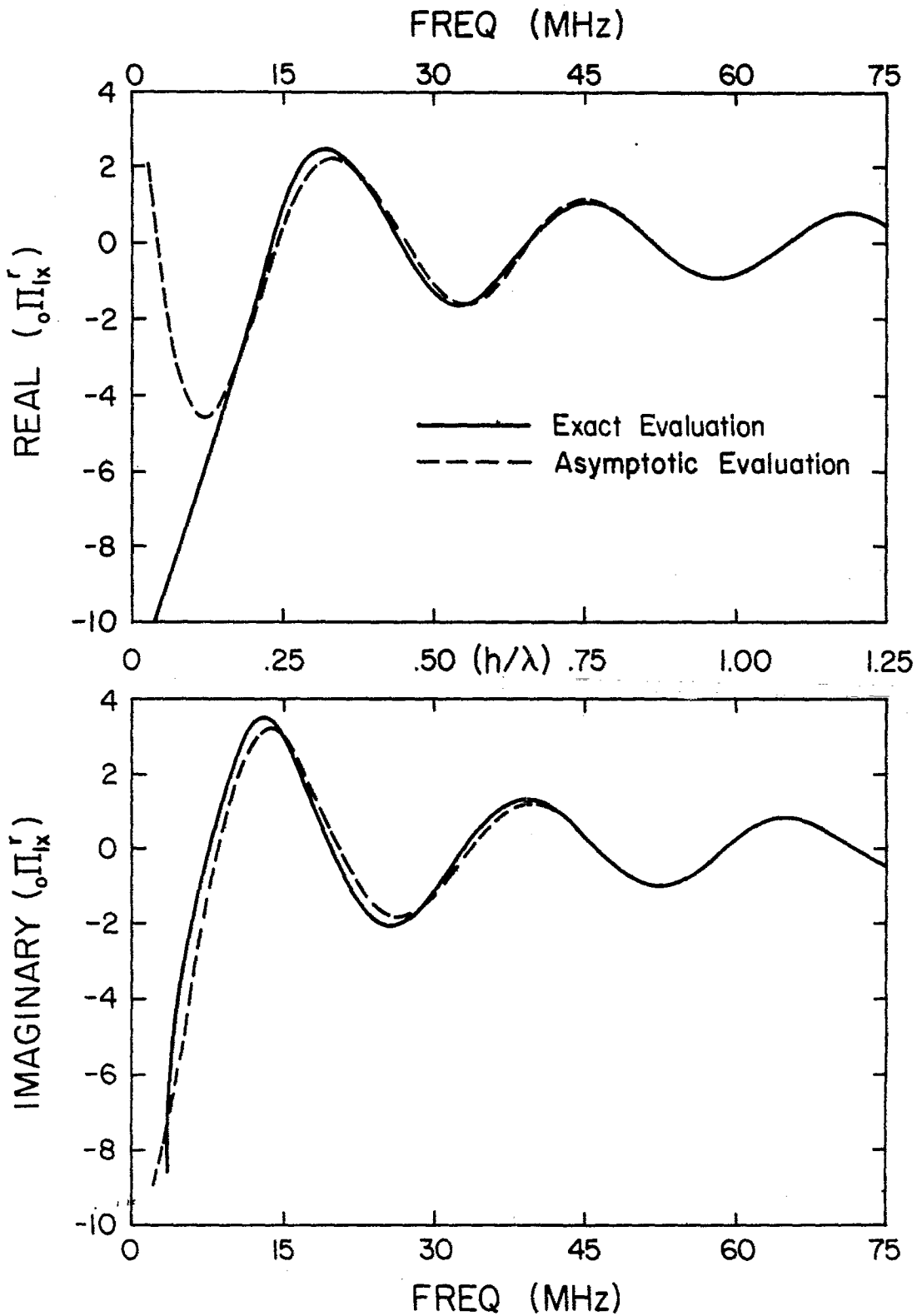
Figure 18. Exact and asymptotic evaluation of $_0\Pi^r_{1x}$. Note that $\theta_2 = 15°$, $h = 5m$, $\varepsilon_r = 10$, and $\sigma = .01$ mhos/m.
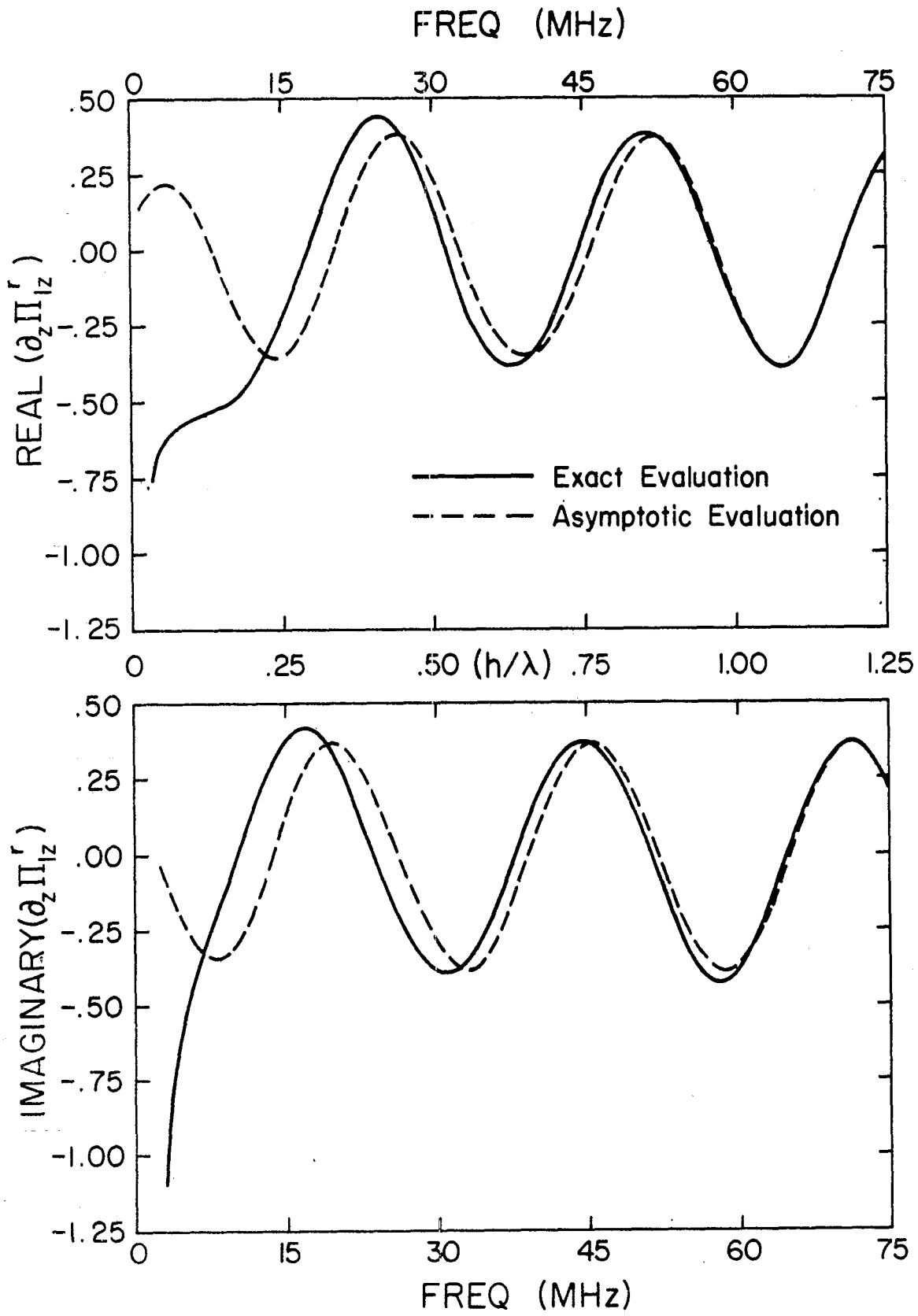
Figure 19. Exact and asymptotic evaluation of $\partial_z \Pi^r_{1z}$. Note that $\theta_2 = 15°$, $h = 5m$, $\varepsilon_r = 10$, and $\sigma = .01$ mhos/m.

4. LOADED HORIZONTAL ANTENNA OVER AN IMPERFECT GROUND

In the previous sections, detailed discussion was given for deriving the vector potentials due to a horizontal current element radiating over imperfect ground. A numerically accurate and efficient method was developed for evaluating the Sommerfeld-type integrals which were encountered. Also presented was an asymptotic evaluation of these integrals and their comparisons with the exact integration results. At this point, we will formulate an integral equation for an arbitrarily loaded horizontal antenna over imperfect (lossy) ground. The method of moments will then be applied to transform the integral equation into a numerically manageable matrix form. Finally, our procedure will be tested by comparing some selected results with those reported in the literature.

4.1 Integral Equation Formulation

The geometry of a thin, linear, horizontal antenna of length 2L, radius a, and mounted with height h over imperfect ground (ε_g, σ) is shown in Fig. 20. The antenna is assumed to be resistively loaded with a functional distribution of $\Lambda(x)$ along the antenna, and is driven by a finite gap source located at the midpoint of the antenna. Let E^{inc} and E^{sca} refer to the tangential electric field components of the incident field (the gap source) and the scattered field on the antenna, respectively. The total tangential electric field may then be written as

$$E^{tot}(x) = E^{inc}(x) + E^{sca}(x) \ .$$ (4.1)

Application of Ohm's law allows one to relate E^{tot} and the induced current $I(x)$ as

$$E^{tot}(x) = \Lambda(x)I(x)$$ (4.2)
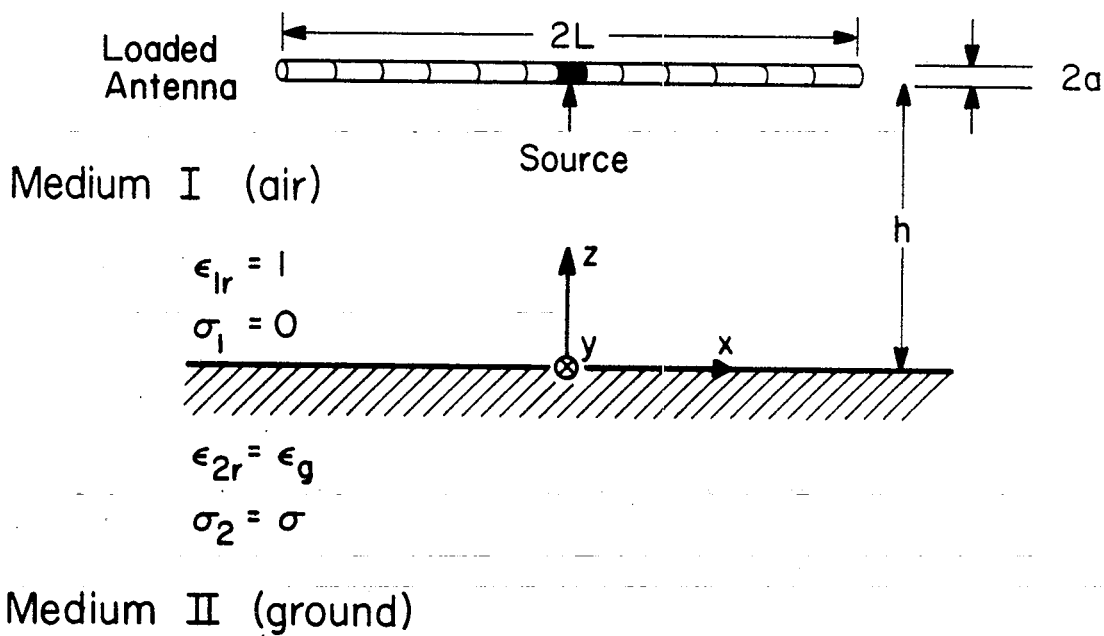
Figure 20. Loaded horizontal antenna over imperfect ground.

where $\Lambda(x)$ is the loading function. Using (2.7), one can express the x

component of the electric field of the current element defined in (2.9) as

$$E_x(x) = \left(\frac{\partial^2}{\partial x^2} + k^2\right) \Pi_{1x} + \frac{\partial^2}{\partial x \partial z} \Pi_{1z} \quad .$$

(4.3)

A simple application of the superposition theorem allows one to finally

determine the integral equation for the induced current $I(x)$

$$E^{inc}(x) = -(j\omega\epsilon 0)^{-1} \left(\frac{d^2}{dx^2} + k^2\right) \int_{-L}^{L} G_h(x,x') I(x') dx' - (j\omega\epsilon_0)^{-1}$$

$$\cdot \frac{d}{dx} \int_{-L}^{L} G_v(x,x') I(x) dx' + \Lambda(x) I(x) \quad ; \qquad -L \leq x \leq L.$$

(4.4)

In the above equation, G_h and G_v are the following functions

$$G_h(x,x') = I_0^{-1} \left(\Pi_{1x}^i + {}_\infty\Pi_{1x}^r + {}_0\Pi_{1x}^r\right)$$

(4.5)

$$G_v(x,x') = I_0^{-1} \frac{\partial}{\partial z} \Pi_{1z}^r$$

(4.6)

where Π_{1x}'s, $\frac{\partial}{\partial z} \Pi_{1z}^r$ and I_0 are defined in (2.31), (2.33), (2.40), (2.43)

and (2.15), respectively. The numerical and asymptotic evaluations of

these expressions have already been discussed in great detail in the previous

section.

4.2 Matrix Equation Formulation

As in many similar problems, the method of moments is employed to

recast (4.4) into a numerically manageable matrix form [16]. Based on our

previous successful results with the half-patch finite difference scheme

[17], this technique is here applied to the $\frac{d}{dx}$ and $\frac{d^2}{dx^2}$ operators. Further-

more pulse and delta functions are used as the basis and weighting functions,

respectively. The resultant matrix equation can then be written as

$$[V^{inc}] = \left\{[Z^{ant}] + [\Lambda]\right\} [I]$$

(4.7)

48

where $[V^{inc}]$ and $[I]$ are column vectors containing the gap voltage and the induced current on the antenna, respectively. Furthermore, $[\Lambda]$ is a diagonal matrix representing the loading function, and finally $[Z^{ant}]$ is the impedance matrix in which element Z_{ij}^{ant} is defined as

$$Z_{ij}^{ant} = -(j\omega\varepsilon_0)^{-1}\,\Delta x\,\left\{\left(\frac{d^2}{dx^2}+k_1^2\right)\cdot\int_{x_j-\Delta x/2}^{x_j+\Delta x/2} G_h(x,x')\,dx' + \frac{d}{dx}\int_{x_j-\Delta x/2}^{x_j+\Delta x/2} G_v(x,x')\,dx'\right\}\Bigg|_{x=x_i}$$

(4.8)

Note that the $\dfrac{d}{dx_i^2}$ and $\dfrac{d}{dx_i}$ operators are approximates such that

$$\frac{d}{dx_i}[f(x)] = \frac{f(x+\Delta x/2) - f(x-\Delta x/2)}{\Delta x}\Bigg|_{x=x_i}$$

(4.9)

$$\frac{d^2}{dx_i^2}[f(x)] = \frac{f(x+\Delta x/2) - 2f(x) + f(x-\Delta x/2)}{(\Delta x/2)^2}\Bigg|_{x=x_i}$$

(4.10)

Expressions (4.9) and (4.10) are the results of the direct application of the half-patch finite difference scheme where Δx is the full patch size used in the method of moments approximation. In evaluating G_h from (4.5), we use the thin wire approximation to express $I_0^{-1}\Pi_{1x}$ along the antenna as

$$I_0^{-1}\,{}^i\Pi_{1x} = \frac{e^{-jkr}}{4\pi r}\,;\quad r = \sqrt{(x-x')^2 + a^2}$$

(4.11a)

$$I_0^{-1}\,{}_\infty\Pi_{1x}^r = \frac{e^{-jkr}}{4\pi r}\,;\quad r = \sqrt{(x-x')^2 + 4h^2}$$

(4.11b)

where a is the antenna radius and h is its height from the ground. These approximations allow one to compute the direct and perfect reflection components of Z_{ij}^{ant}'s, which are the results of integrating (4.11a) and (4.11b) over a patch, in a closed form as described by Harrington [18].

Performing a simple matrix inversion, one can finally solve (4.7) for

[I] to arrive at

$$[I] = [Y^{ant}][V^{inc}] \qquad (4.12)$$

where

$$[Y^{ant}] = \left\{ [Z^{ant}] + [\Lambda] \right\}^{-1} \quad . \qquad (4.13)$$

4.3 Numerical Results and Discussion

Based on the analytical developments in the previous sections, a

Fortran digital computer program has been developed for calculating the

current along a loaded horizontal wire antenna mounted over lossy ground.

To conserve computing time, only one row of the impedance matrix has been

computed, since $[Z^{ant}]$ takes the following general form (Toeplits matrix)

$$[Z^{ant}] = \begin{bmatrix} a_1 & a_2 & a_3 \cdots a_n \\ a_2 & a_1 & a_2 \cdots a_{n-1} \\ a_3 & a_2 & a_1 \cdots a_{n-2} \\ \cdot & \cdot & \cdot & \cdot \\ \cdot & \cdot & \cdot & \cdot \\ \cdot & \cdot & \cdot & \cdot \\ a_n & a_{n-1} & a_{n-2} \cdots a_1 \end{bmatrix} \qquad (4.14)$$

and thus expresses the inherent symmetry of the problem. Also note that

when (4.14) is modified by the diagonal loading matrix, it still remains

symmetric, so a more efficient inversion routine has been employed in

obtaining $[Y^{ant}]$.

In order to test our integral equation formulation, the case of a

linear antenna in free space ($\varepsilon_g = 1$, $\sigma = 0$) is considered. Figures 21 and

22 show the input impedance values as a function of frequency. These

results agree well with available reported data [19], therefore, indicating

that the finite difference approximation does indeed provide an accurate

result. The perfect ground case ($\sigma = \infty$) is investigated next; Fig. 23

50
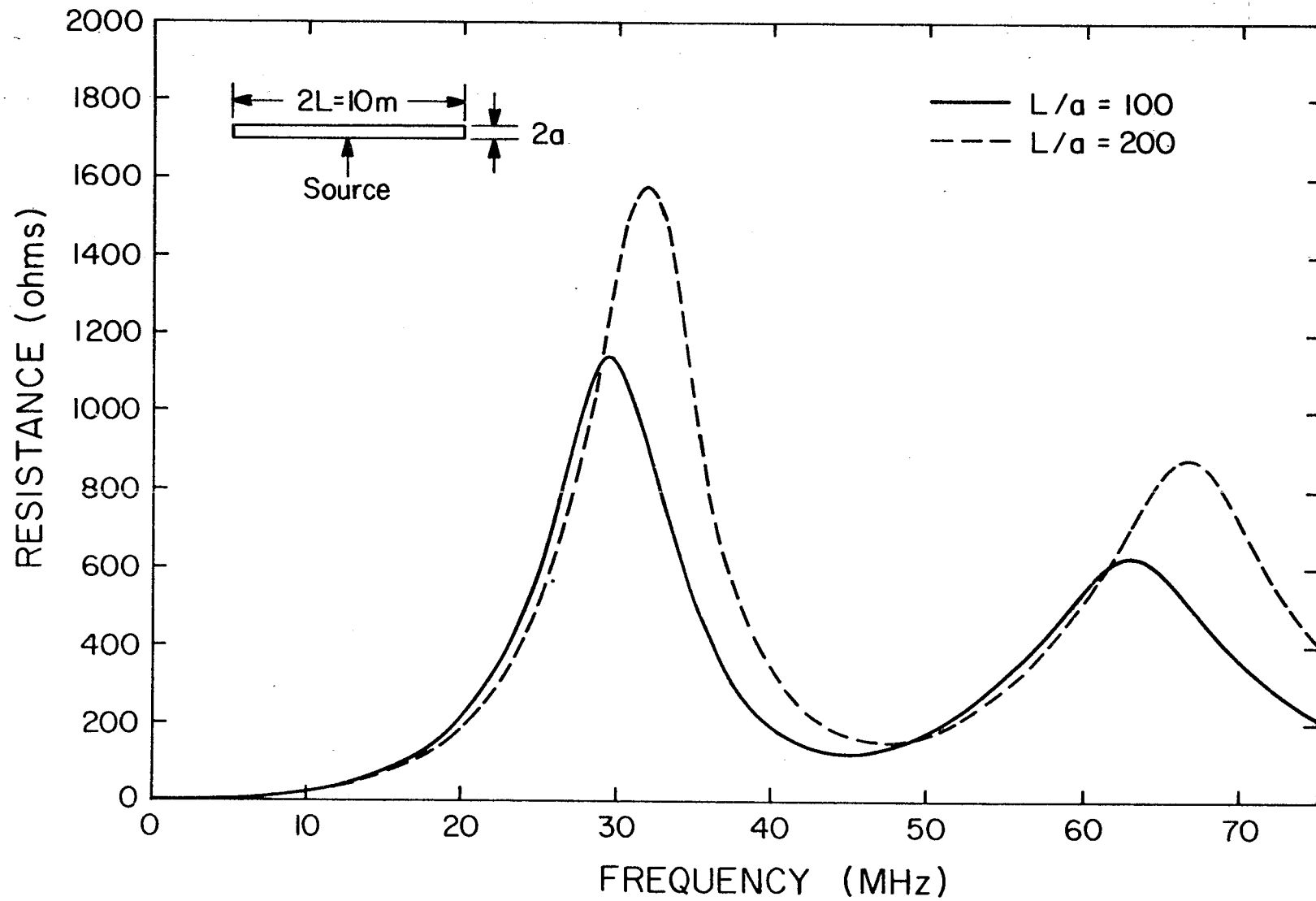
Figure 21.   Input resistance of an unloaded dipole antenna (2L = 10m) radiating in free space.
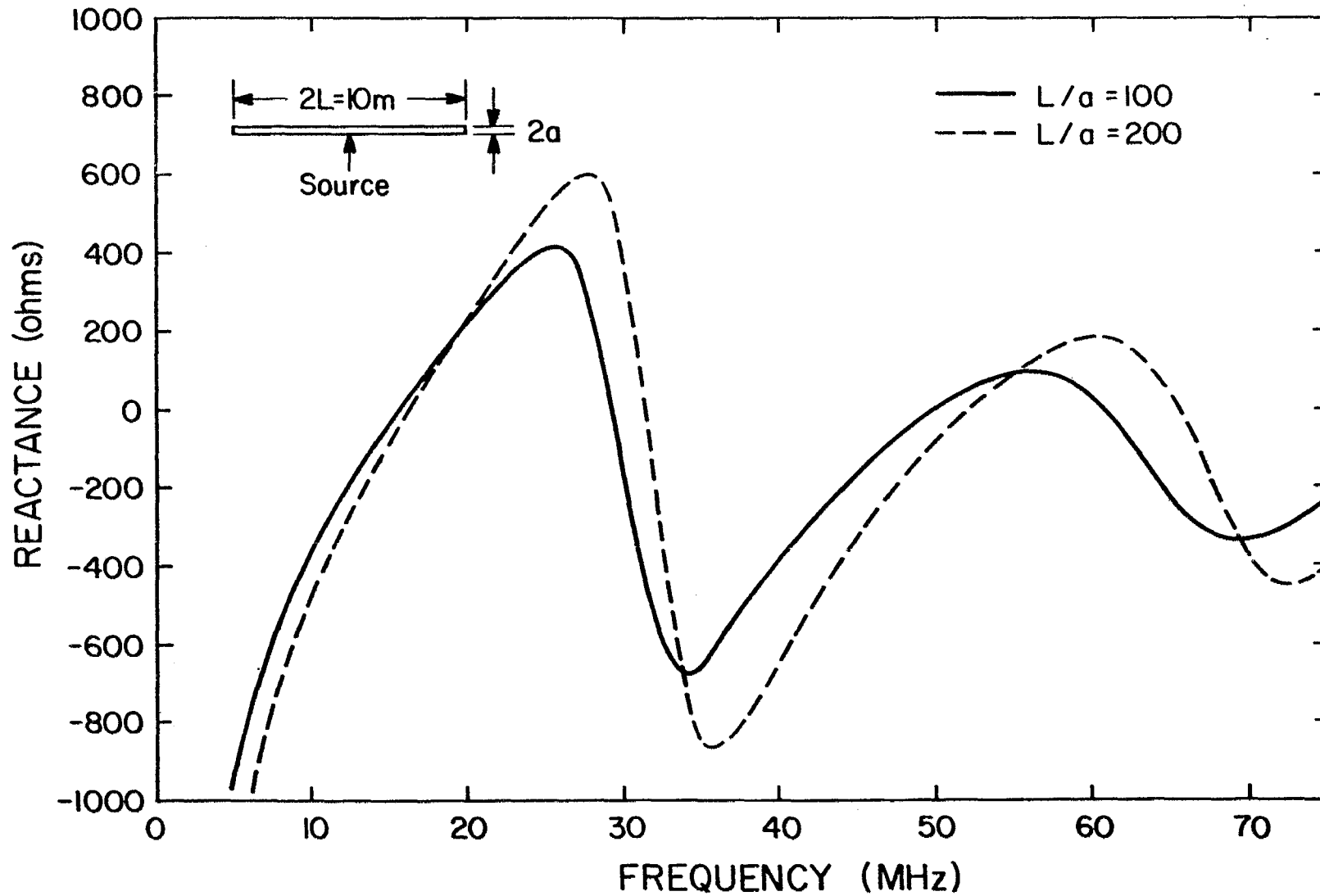
Figure 22.   Input reactance of an unloaded dipole antenna (2L = 10m) radiating in free space.
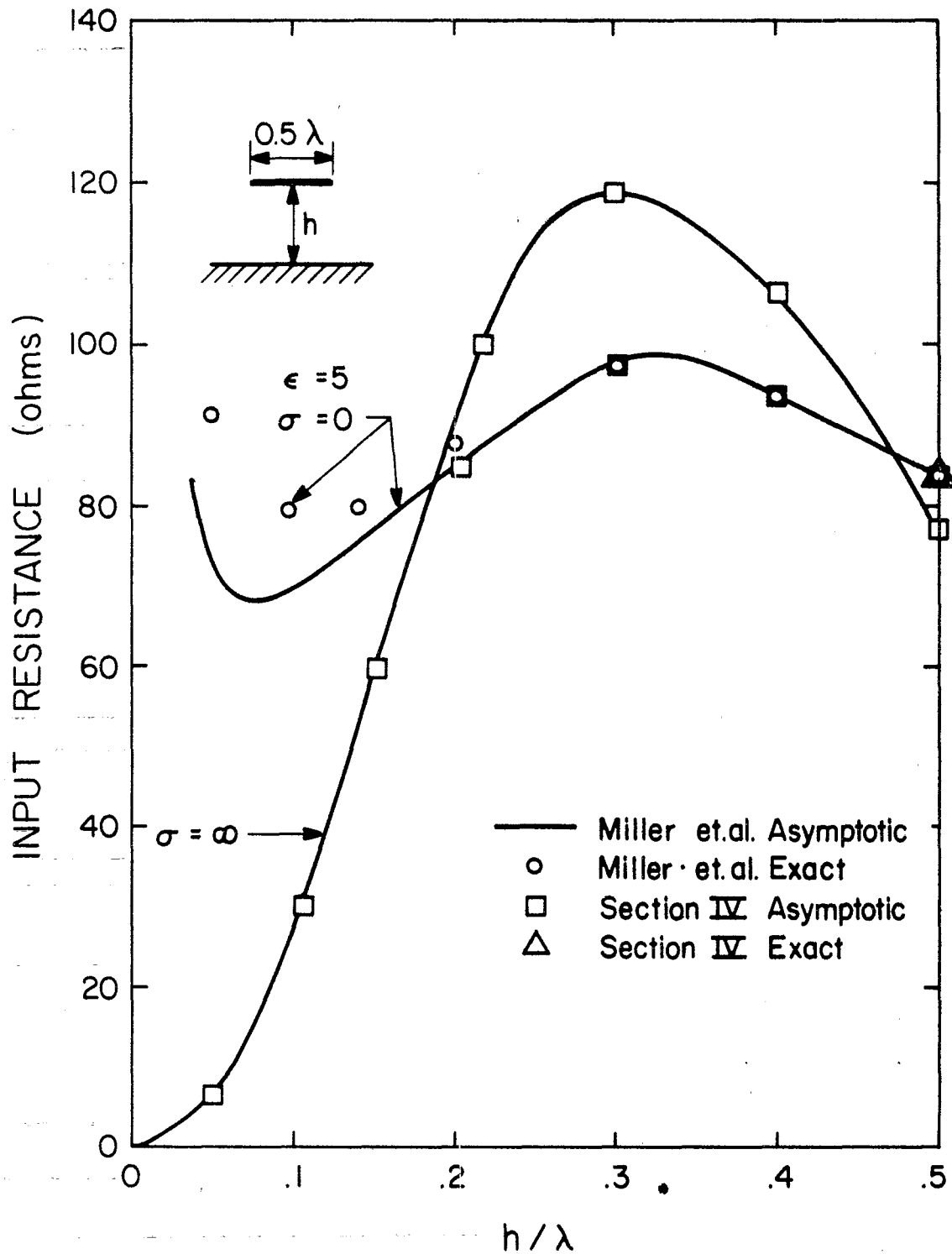
Figure 23.   Comparison of the presented techniques with that of Miller et
al. Note that the frequency = 3.0 MHz, and the antenna radius
= .005 λ.

53

clearly demonstrates excellent agreement between our result and that
reported by Miller et al., [4], in which a three-term sinusoidal current
expansion with delta matching was used to generate the matrix equation.
This result is quite compatible with the conclusion drawn in [20] where
it was shown that the procedure based on finite difference and pulse
expansion is closely related to the three-term sinusoidal expansion
approximation.

There are not many experimental and/or numerical data available
for the linear horizontal antenna over an imperfect ground. Miller et al.
[4] have reported some numerical results using three-term sinusoidal
expansion functions and a different approach in evaluating the Sommerfeld
integral. Here, we compare the results of our method with those of
Miller's in Figs. 23, 24. The agreement is excellent and provides a good
check for both of the numerical methods.
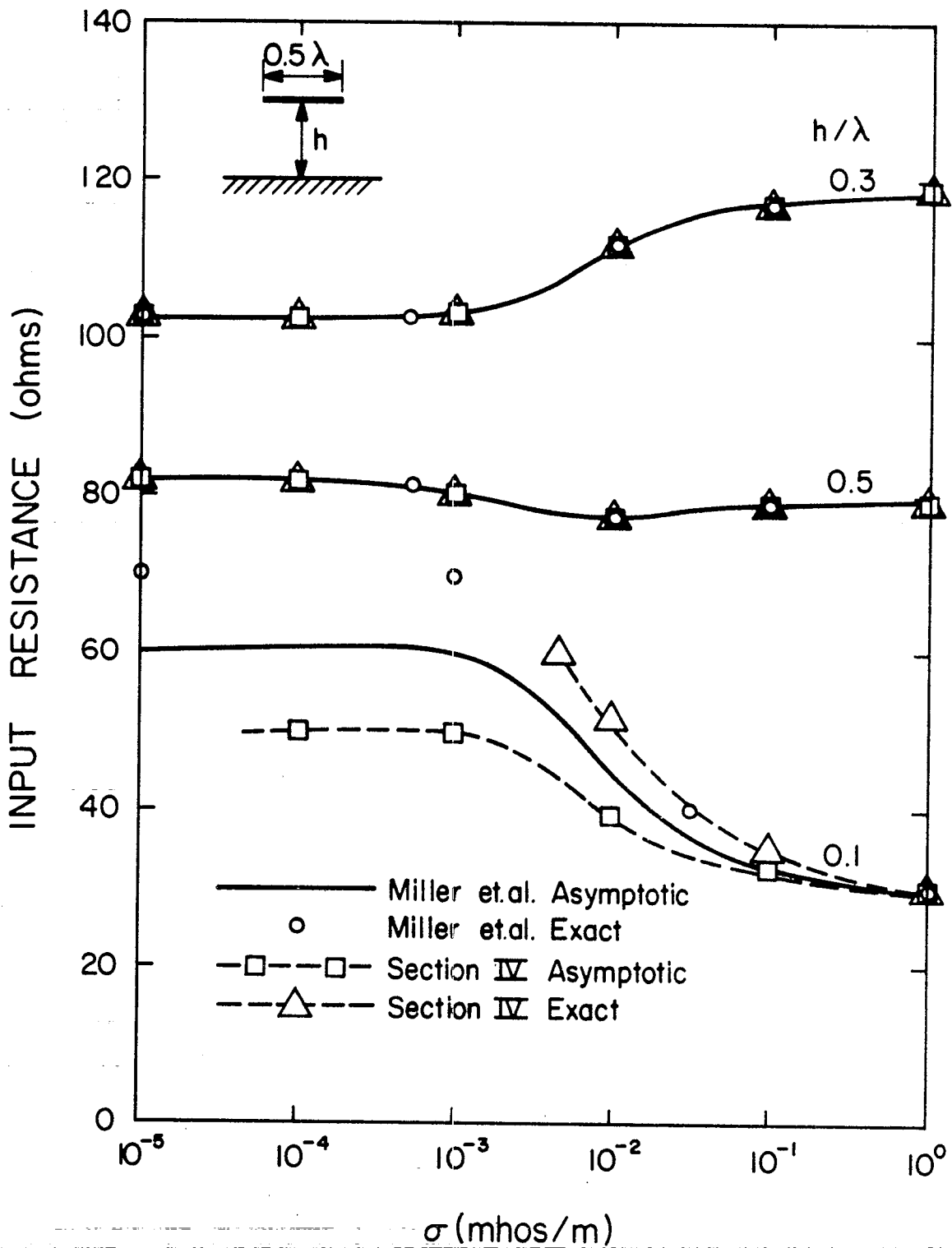
Figure 24. Comparison of the presented technique with that of Miller et al. Note that the frequency = 3.0 MHz, and the antenna radius = .005 λ.

$\epsilon_r = 10.$

5. TRANSIENT BEHAVIOR OF THE ANTENNA CURRENT

In this section the frequency domain results of the previous sections are used to investigate the transient behavior of the antenna current mounted over lossy ground and driven by a pulser. As a first step, the transfer function (impulse response) of the antenna current is computed using the results of Section 4. This transfer function is then multiplied by the spectrum of the input pulse, and finally the Fourier inversion is performed numerically via a Fast Fourier Transform (FFT) routine to obtain the transient response.

The pulser is assumed to drive the antenna at the mid-point with the following Gaussian Form

$$v(t) = \exp[-(t - \tau)^2/\sigma_p] \quad . \tag{5.1}$$

Using the transform pairs defined below

$$V(f) = \int_{-\infty}^{\infty} v(t)e^{-j2\pi ft} \, dt \tag{5.2a}$$

$$v(t) = \int_{-\infty}^{\infty} V(f)e^{j2\pi ft} \, dt \tag{5.2b}$$

one readily finds that

$$V(f) = \sqrt{2\pi} \, \sigma_p \, \exp[-\omega^2\sigma_p^2/2]\exp[-j2\pi f\tau] \tag{5.3}$$

where $f = \omega_0/2\pi$ designates the frequency. Figure 25 displays $v(t)$ and $V(f)$ for $\tau = 0$ and two different values of σ_p.

At a point x on the antenna the current transfer function may be defined by $H(x,f)$, which is the delta-response of the antenna at point x. The transfer function can be constructed discretely using the developments of the previous sections. Using the superposition theorem,

56

$$v(t) = \exp\left[-t^2 \big/ 2\sigma_p^2\right]$$

σ_p = 1.0 ns
= 0.471 ns

1.0

0.5

t (ns)

−5 −4 −3 −2 −1 0 1 2 3 4 5

$$V(f) = \sqrt{2\pi}\ \sigma_p \exp\left[-\omega^2 \sigma_p^2 \big/ 2\right]$$

× 10⁻⁹

2

1

−800 −400 0 400 800 f (MHz)
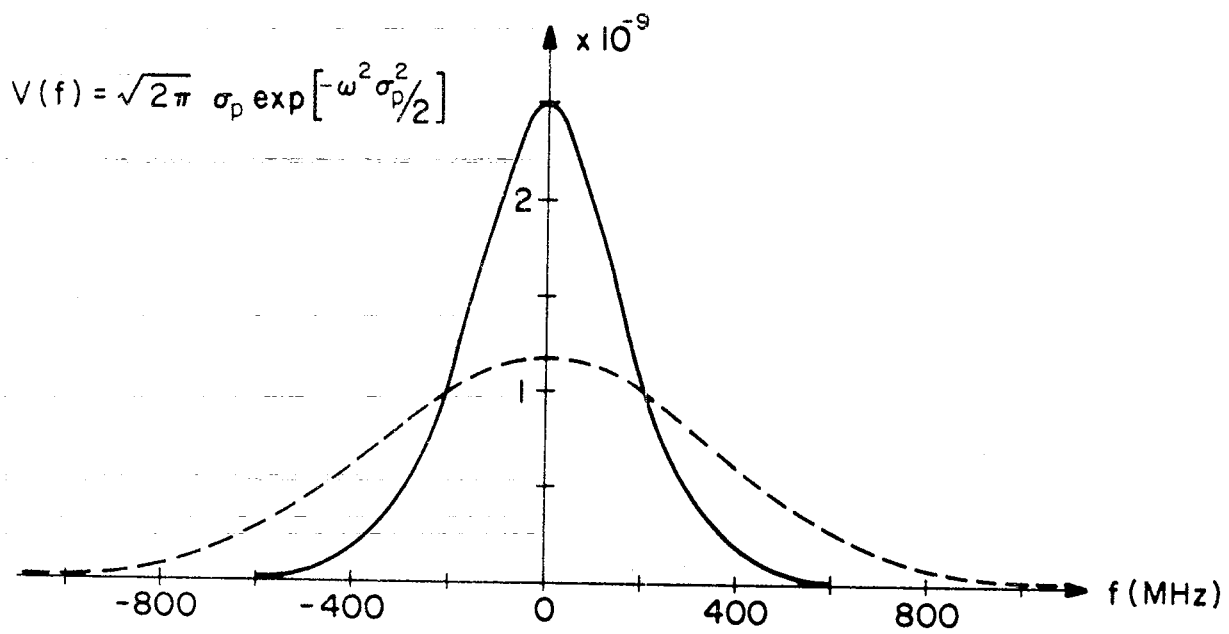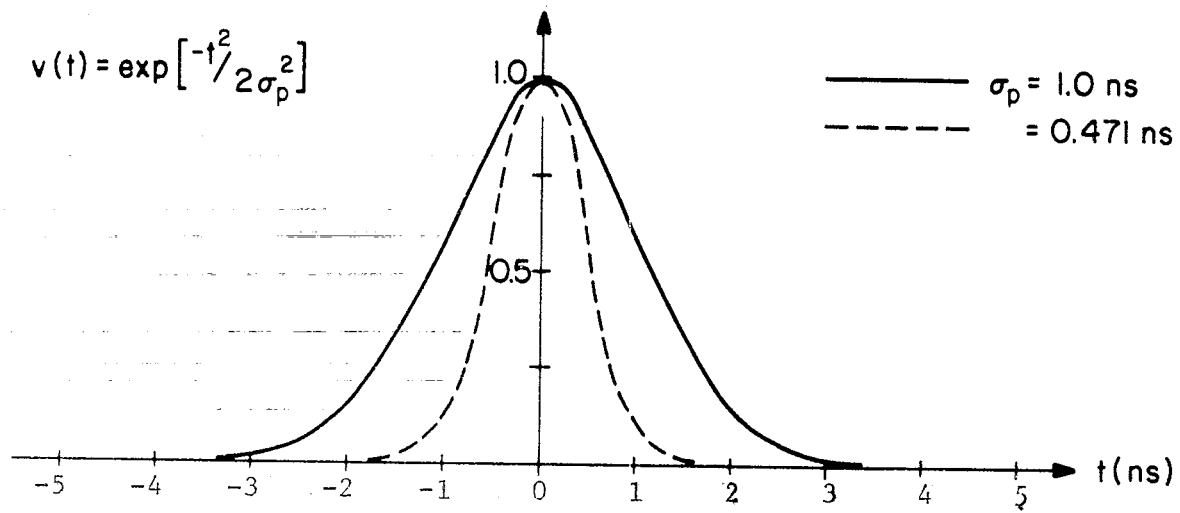
Figure 25. The Gaussian pulse used for excitation.

57

the transform of the current at point x due to the input pulse V(t)

can be written as

$$I(x,f) = V(f) H(x,f) .$$ (5.4)

Using the transform convention in (5.22), the transient response of the

antenna current at point x can be expressed as

$$i(x,t) = \int_{-\infty}^{\infty} I(x,f)e^{j2\pi ft} df .$$ (5.5)

Since i(x,t) is a real function, one concludes that

$$I(x,-f) = I^*(x,f)$$ (5.6)

where * denotes conjugation. Furthermore, because v(t) is itself a real

function the following is true

$$V(-f) = V^*(f)$$ (5.7)

which finally results in

$$H(x,-f) = H^*(x,f) .$$ (5.8)

In other words the knowledge of I(x,f) for positive frequencies is enough

to enable one to determine i(t) from (5.5). This final step is done

numerically using the FFT routine. Note that nowhere in our development

have we enforced the causality condition which, for example, states that

for an input pulse starting at t = 0, there cannot be any current excited

at a distance x before time x/c, where c is the velocity of light. This

fact can be used as a valuable check point for the final result, i(x,t),

and as seen later on, is indeed satisfied by our results.

As previously discussed, by loading antennas one can shape their

time domain responses. It has been found that a resistive loading with the

following functional distribution

$$\Lambda(x) = \frac{\Lambda_0}{1 - |x|/L}$$ (5.9)

58

provides the most desirable control for reducing the end point reflections at a given frequency. References [21] and [22] discuss the suitability of (5.9) for loading antennas in free space. Appendix III is a self-contained recent report for determining the Λ_0 parameter for a horizontal antenna over imperfect ground. This appendix primarily considers the Fresnel reflection coefficient approximation for determining the antenna currents, and is used in this work for obtaining an optimal value for Λ_0.

In the following subsections, we provide extensive numerical results for a 10 m antenna of radius 0.05 m mounted 5 m above an imperfect ground characterized by $\varepsilon_g = 10$, and $\sigma = .01$ mhos/m.

5.1 Current Transfer Function H(x,f)

The current transfer function is simply the antenna current values, at a given observation point, due to one volt excitation at several frequencies. For each frequency, the impedance matrix $[Z^{ant}]$ of Equation (4.7) is computed regardless of loading. Sample integrands encountered in evaluating the impedance matrix elements are shown in Figs. 6-17. In order to conserve time, the exact numerical integration is used only up to 60 MHz, where the asymptotic approximation is shown to be within 5% error (see Figs. 18 and 19). As explained in Section 4.3, only one row of the impedance matrix is computed because of the symmetries involved.

Fortunately, for the considered parameters, no poles encounter the steepest descent path deformation (see Fig. 26) for $0 \leq \theta_2 \leq 45°$. However, as seen in Fig. 26, at higher frequencies (f > 7.5 MHz) a branch point does enter the path deformation for higher θ_2 values. Note that Figs. 12, 13, 16 and 17 demonstrate that the integrands have decayed to negligible values around where the branch cut is intercepted. It is concluded that the branch point contribution is of second order and can be neglected. This approximation is also verified and shown by [14].

59

Figure 26. A complete diagram for the pole and branch cut locations as a function of frequency and the steepest descent path for minimum and maximum θ_2 values.

The antenna transfer function $H(x,f)$ is computed at the total of 127 frequencies in the range of $1 \le f \le 400$ MHz with more samples concentrated at the resonance frequencies. Figures 27-29 show the transfer functions of the unloaded antenna at three observation points. Using the loading function given in (5.1), and choosing a proper loading of $\Lambda_0 = 40$ ohms/m, based on the results of Appendix III, the loaded transfer response is computed and shown in Figs. 30-32.

5.2 Computation of $i(x,t)$

The input pulse of Fig. 25 is shifted by $\tau = 30$ nsec so that the applied voltage would start at $t = 0$ and reach its peak at $t = 30$ nsec. The transform of the input pulse is multiplied by the antenna transfer functions shown in Figures 27-32 to obtain the corresponding $I(x,f)$'s which are shown in Figs. 33-38. Note that at $f = 400$ MHz, the resultant frequency domain currents have decayed sufficiently so that zeros can be added for $f > 400$ MHz. Also using (5.6 - 5.8), the negative frequency domain currents can be directly constructed as the conjugate of the positive frequency values.

Now that the entire frequency domain is constructed numerically, a Fast Fourier Transform routine is employed to obtain the time response $i(x,t)$. Since many points are needed to assure proper sampling, a linear interpolation is made through the available $I(x,f)$ data points, and from that, 2048 equi-distance samples are fed into the FFT routine. Figures 39-41 contain the unloaded time response at three observation points, while Figs. 42-47 demonstrate the corresponding current transient responses when $\Lambda_0 = 20$ ohm/m and $\Lambda_0 = 40$ ohm/m loading parameters are employed.

It is interesting to point out that the causality is satisfied very convincingly in Figs. 39-47. Also note that the sharp peaks in Figs. 39-41

61
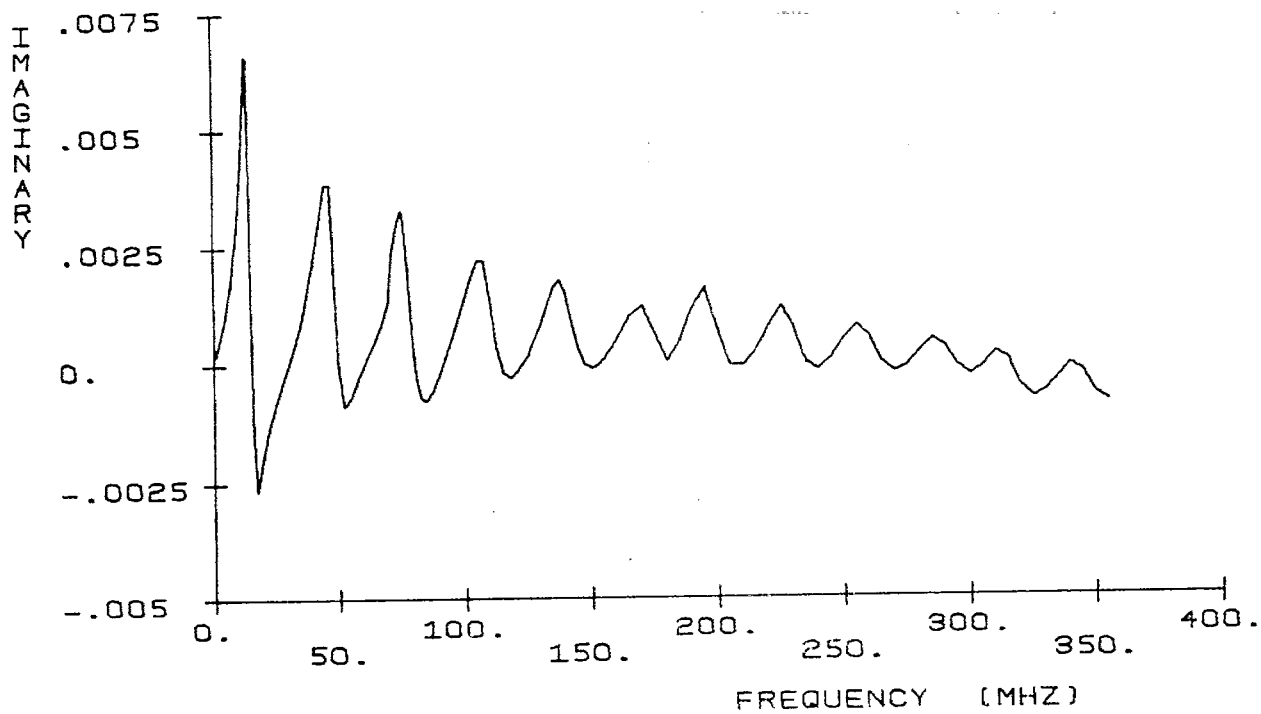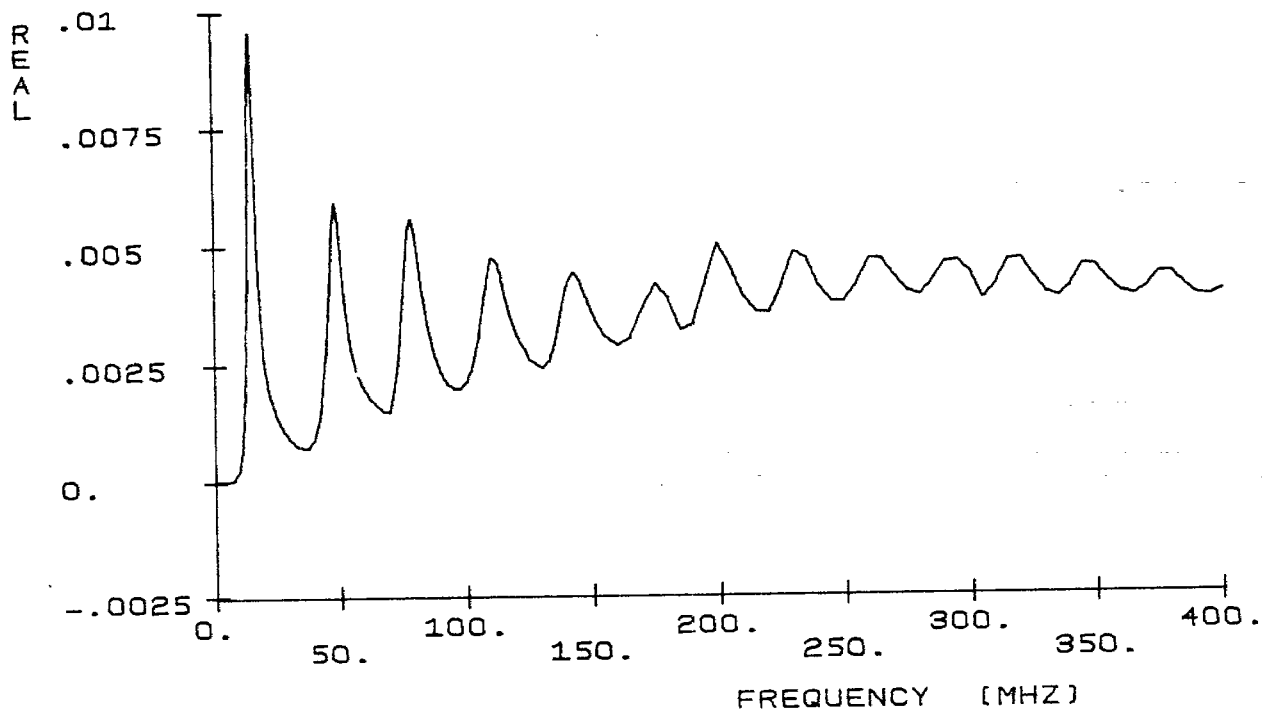
Figure 27. The unloaded transfer function H(x,f). Observation point x is on the feed patch.
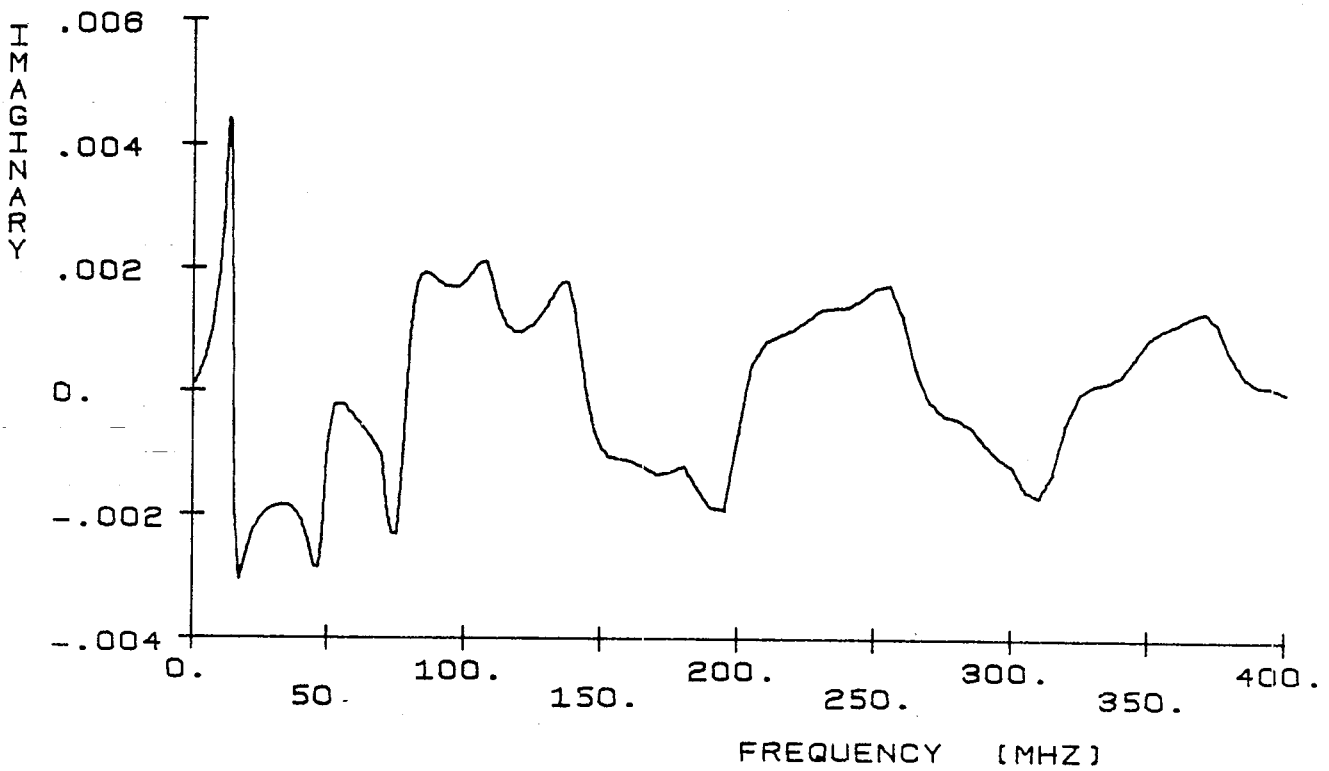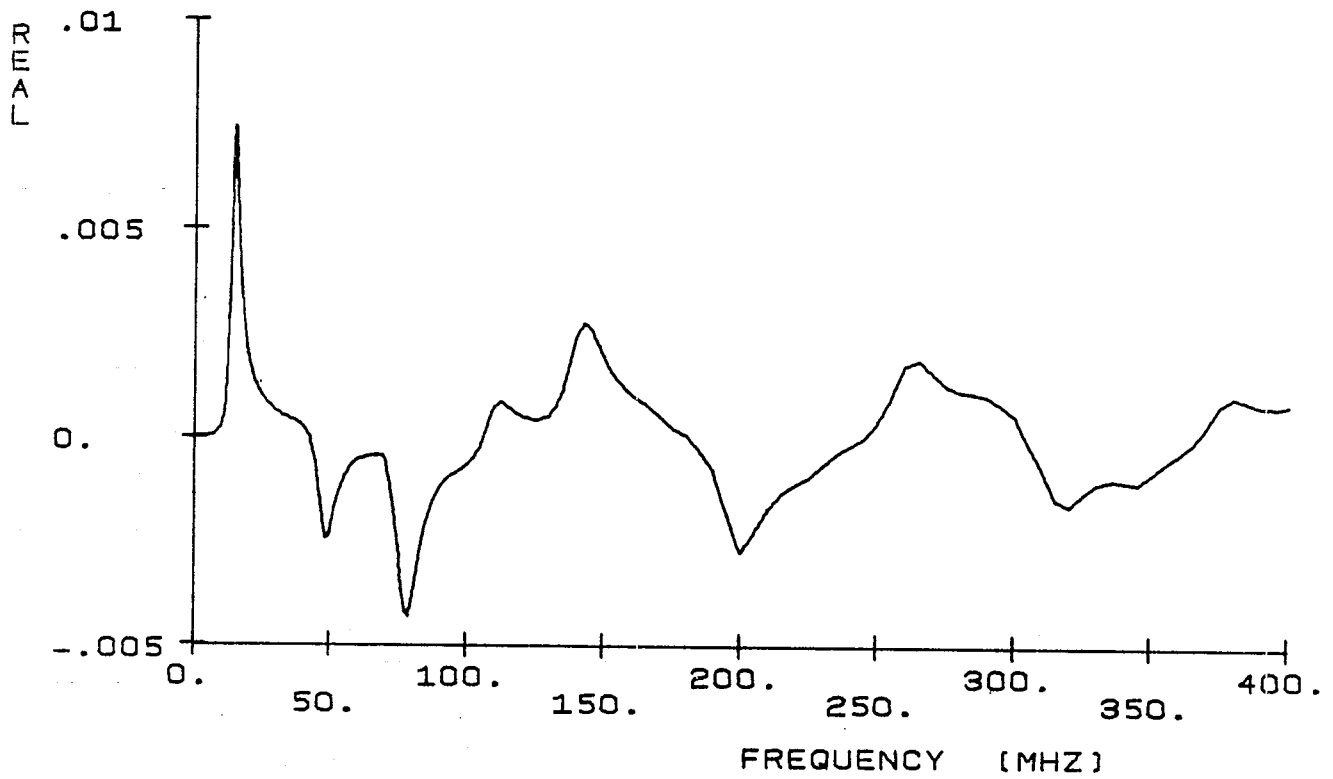
Figure 28. The unloaded transfer function H(x,f). Observation point x is midway between the feed and the end patches.

63
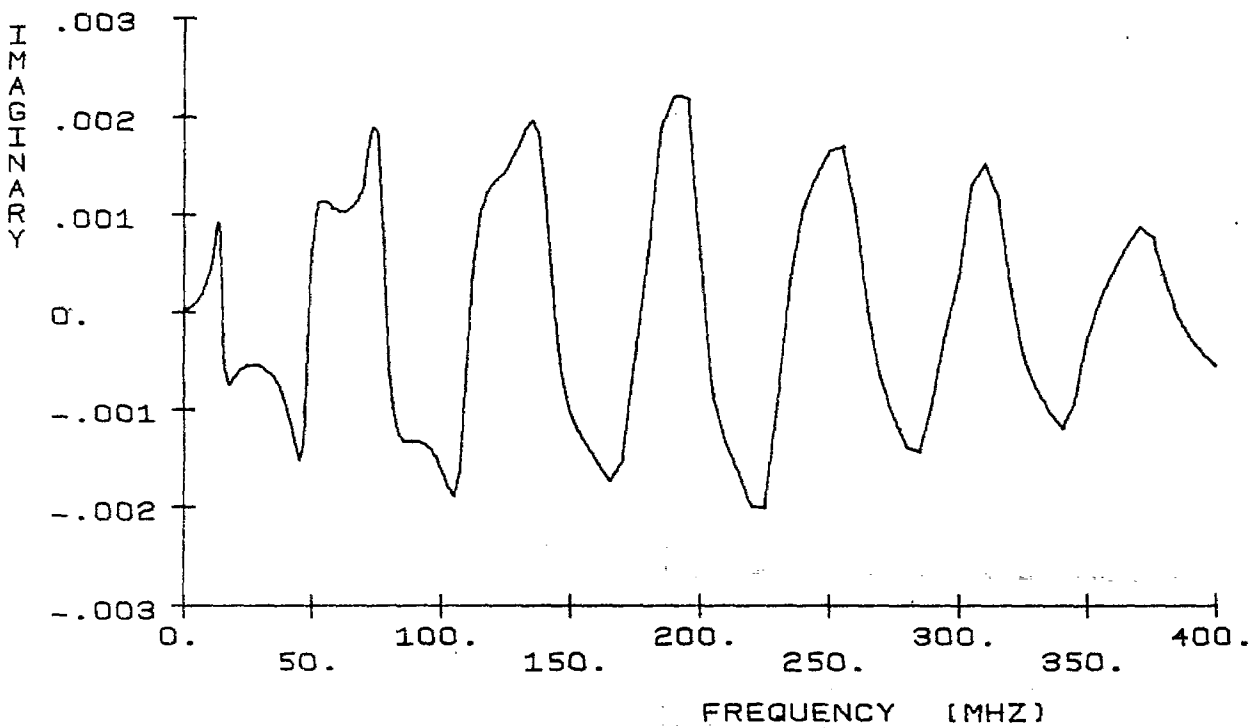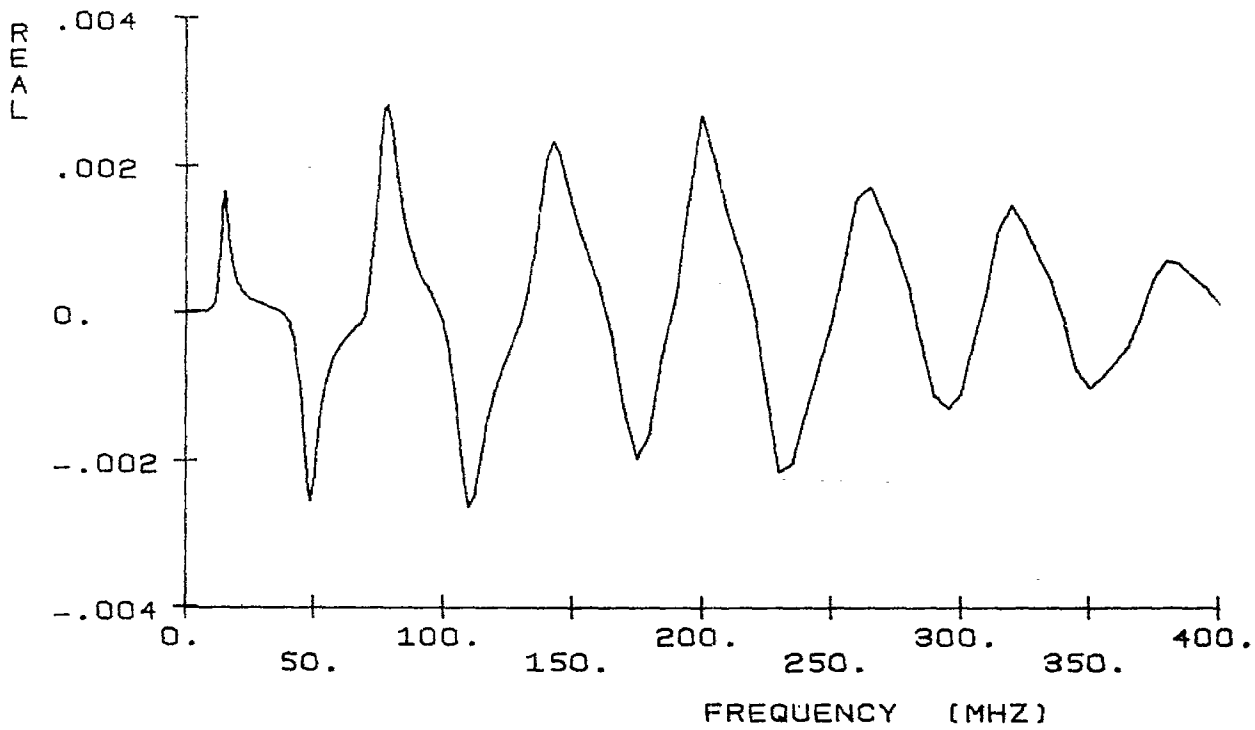
Figure 29.   The unloaded transfer function H(x,f).   Observation point x is on the center of the end patch.
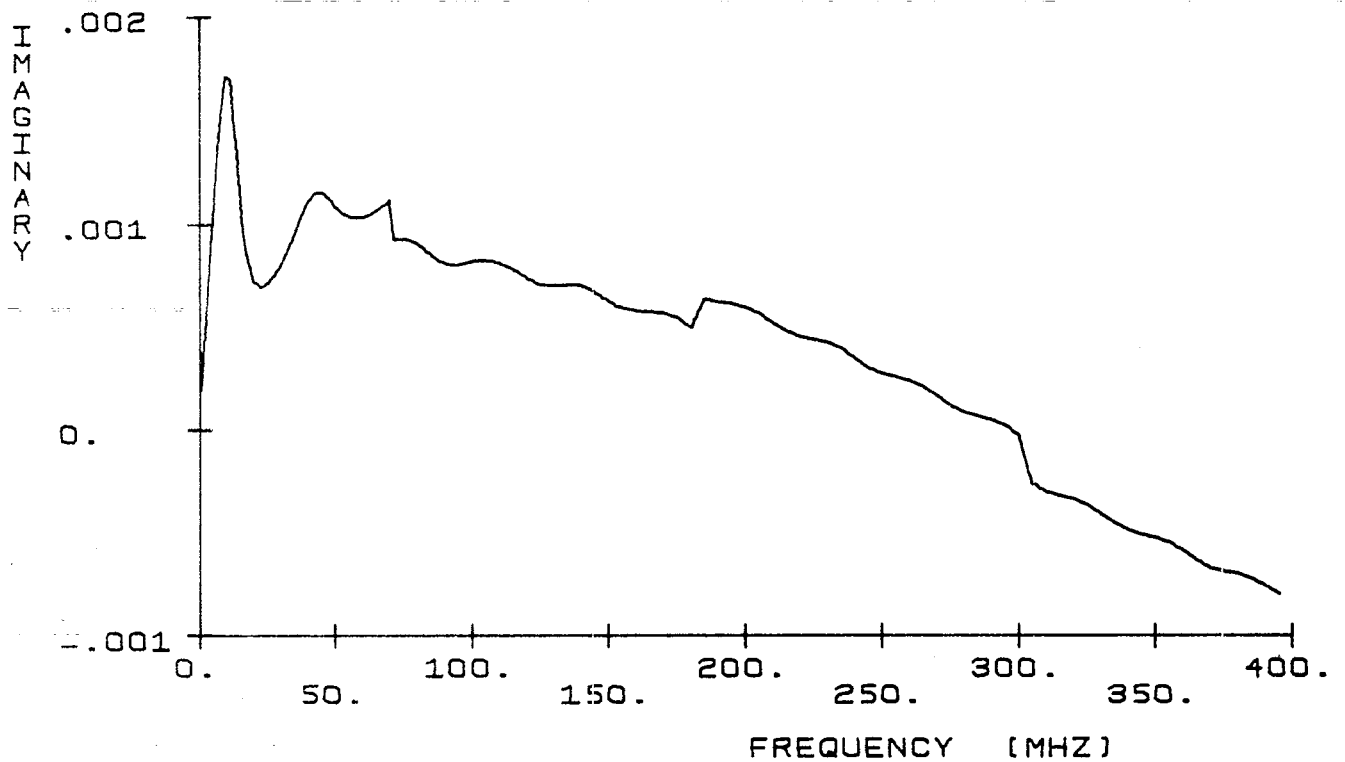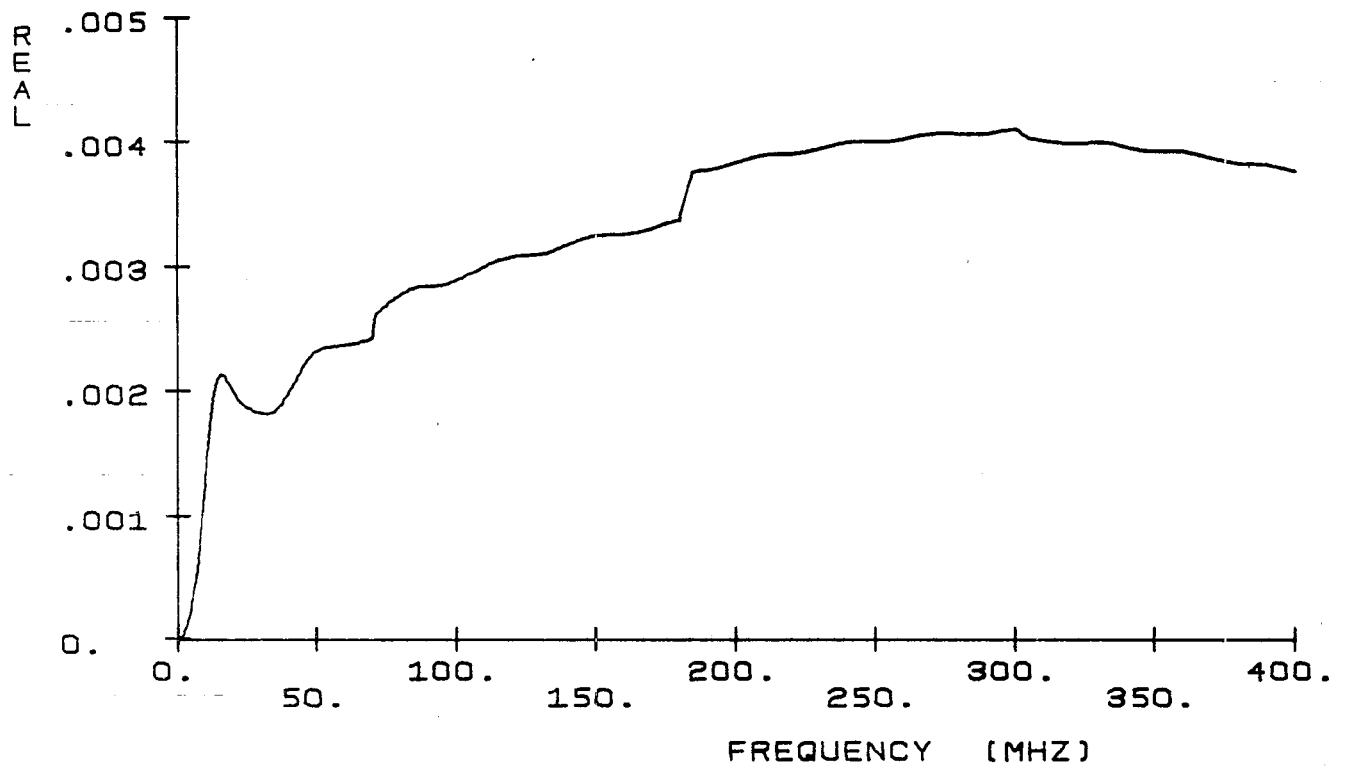
Figure 30. Loaded $(\Lambda_0 = 40$ ohms/m) transfer function $H(x,f)$. Observation point x is on the feed patch.

Figure 31. Loaded (Λ_0 = 40 ohms/m) transfer function H(x,f). Observation Point x is midway between the feed and the end patches.

Figure 32. Loaded (Λ_0 = 40 ohms/m) transfer function H(x,f). Observation point x is on the center of the end patch.
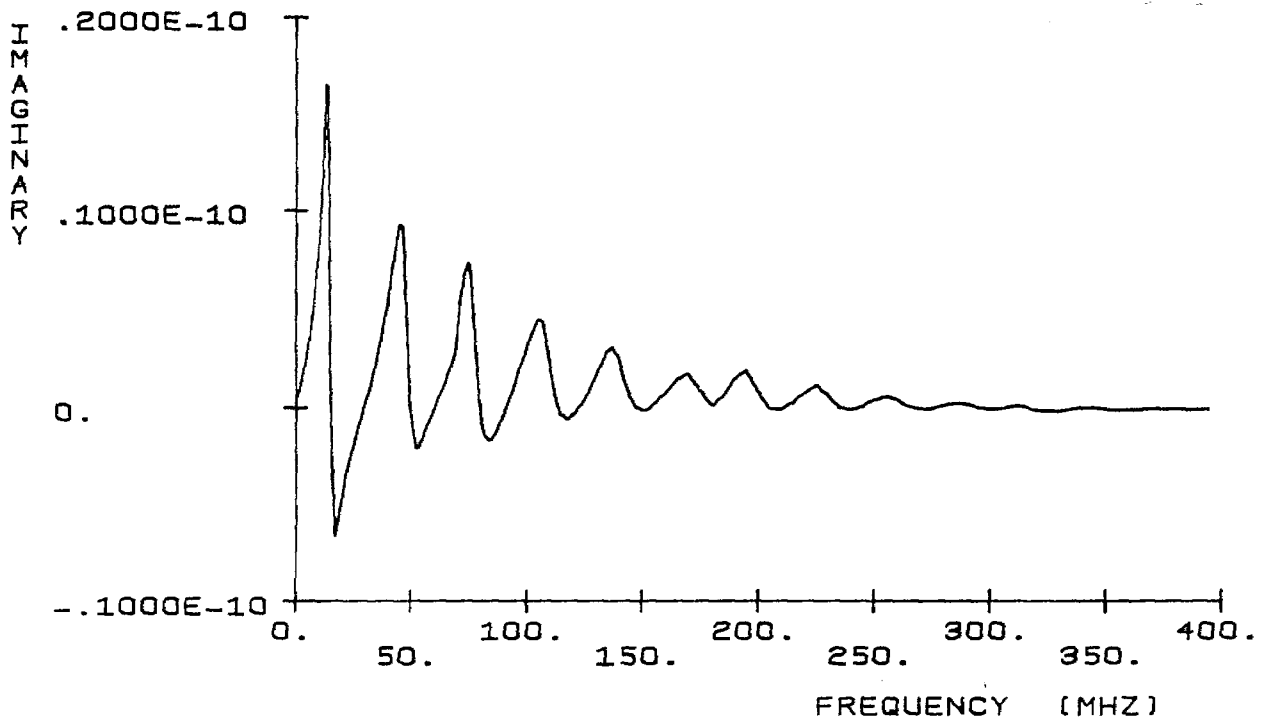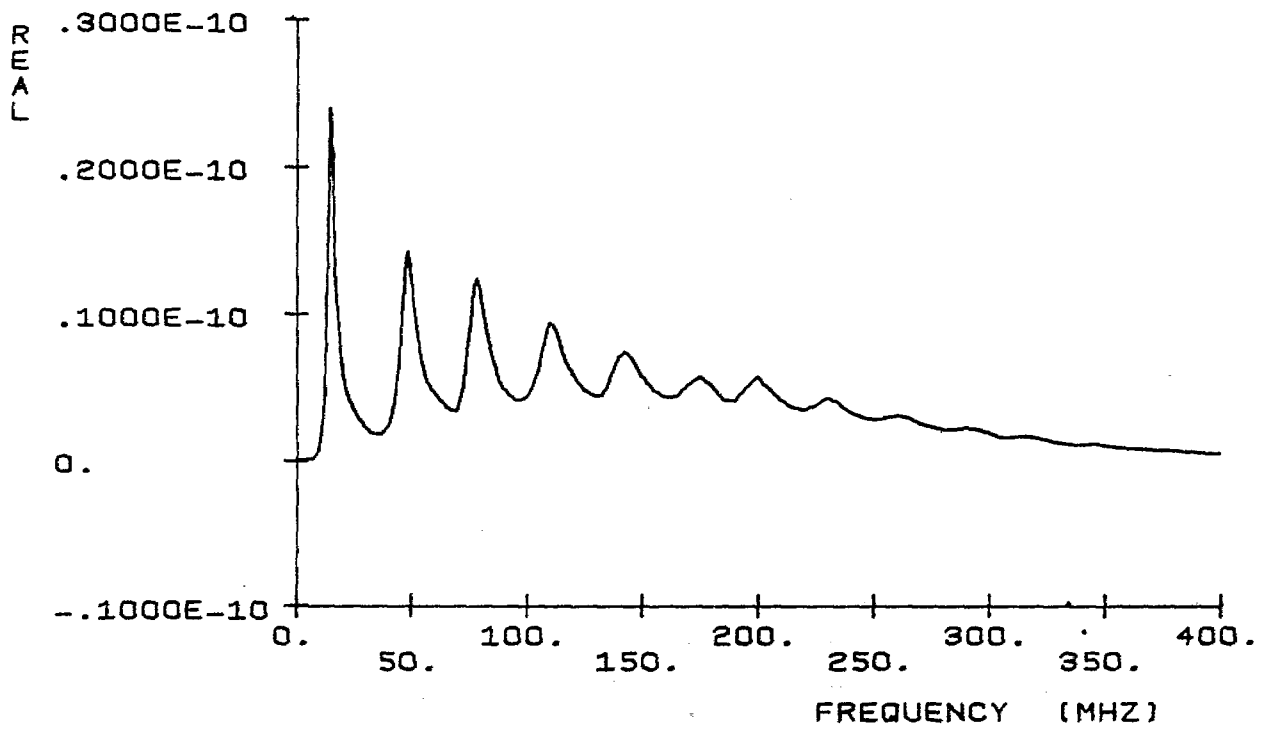
Figure 33. Unloaded frequency domain current I(x,f). Observation point x is on the feed patch.
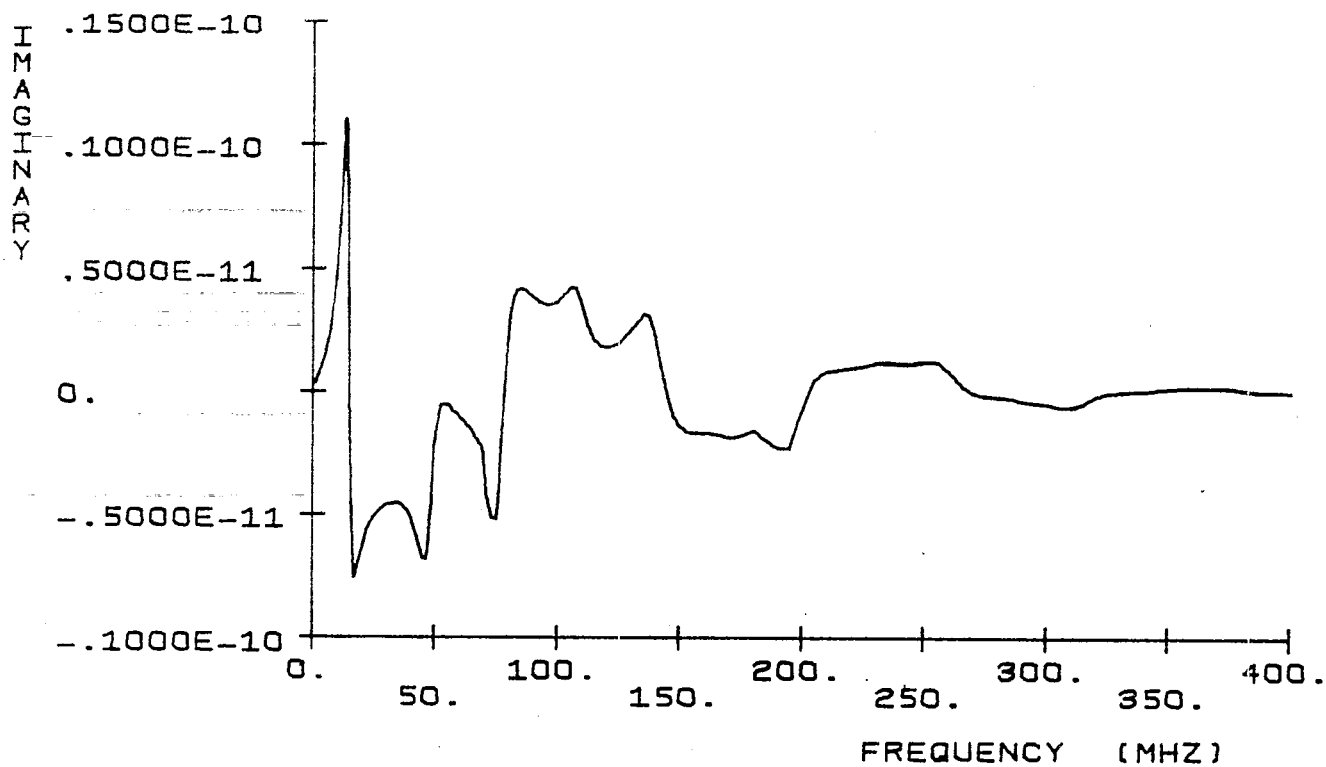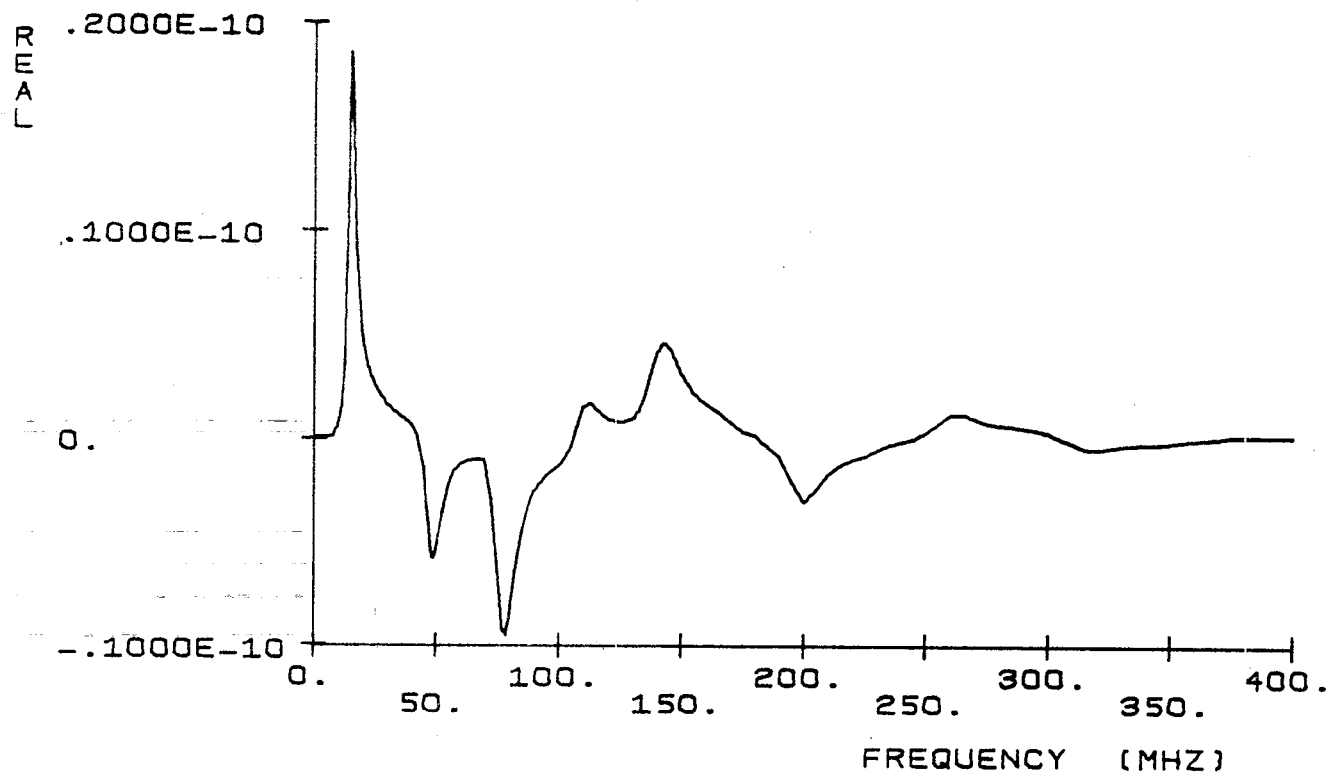
Figure 34. Unloaded frequency domain current I(x,f). Observation point x is midway between the feed and the end patches.
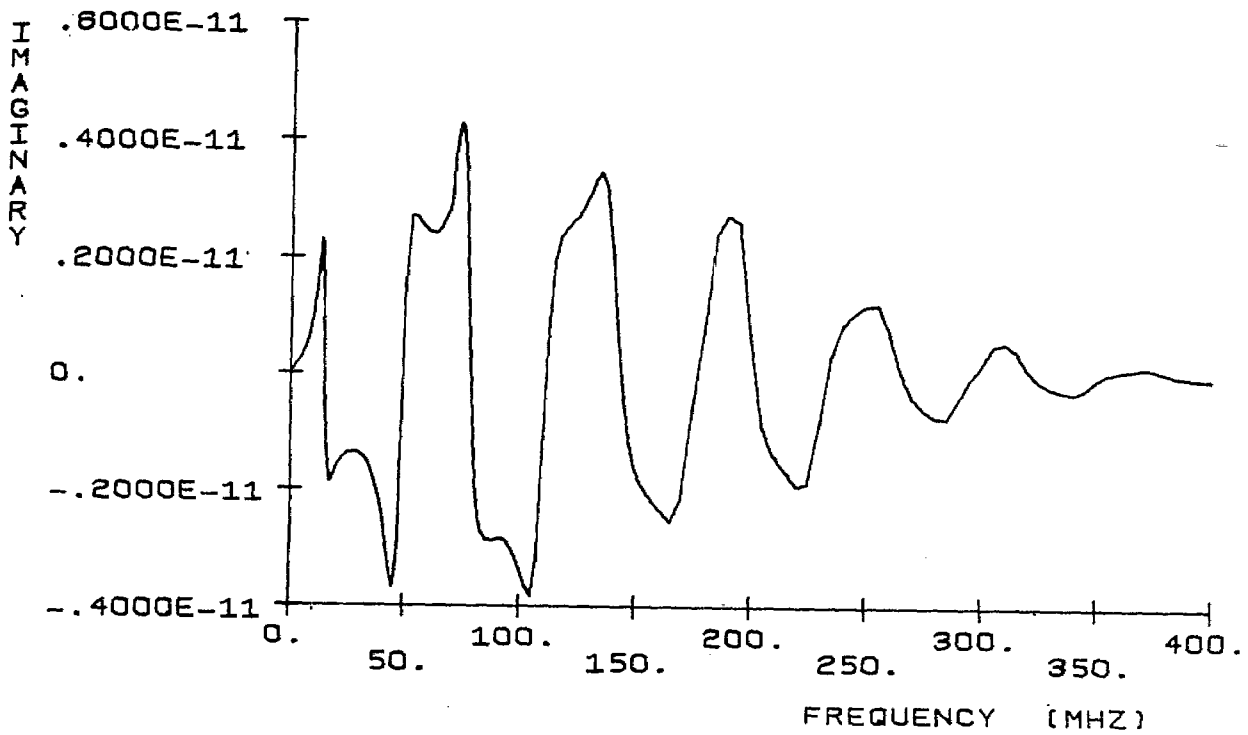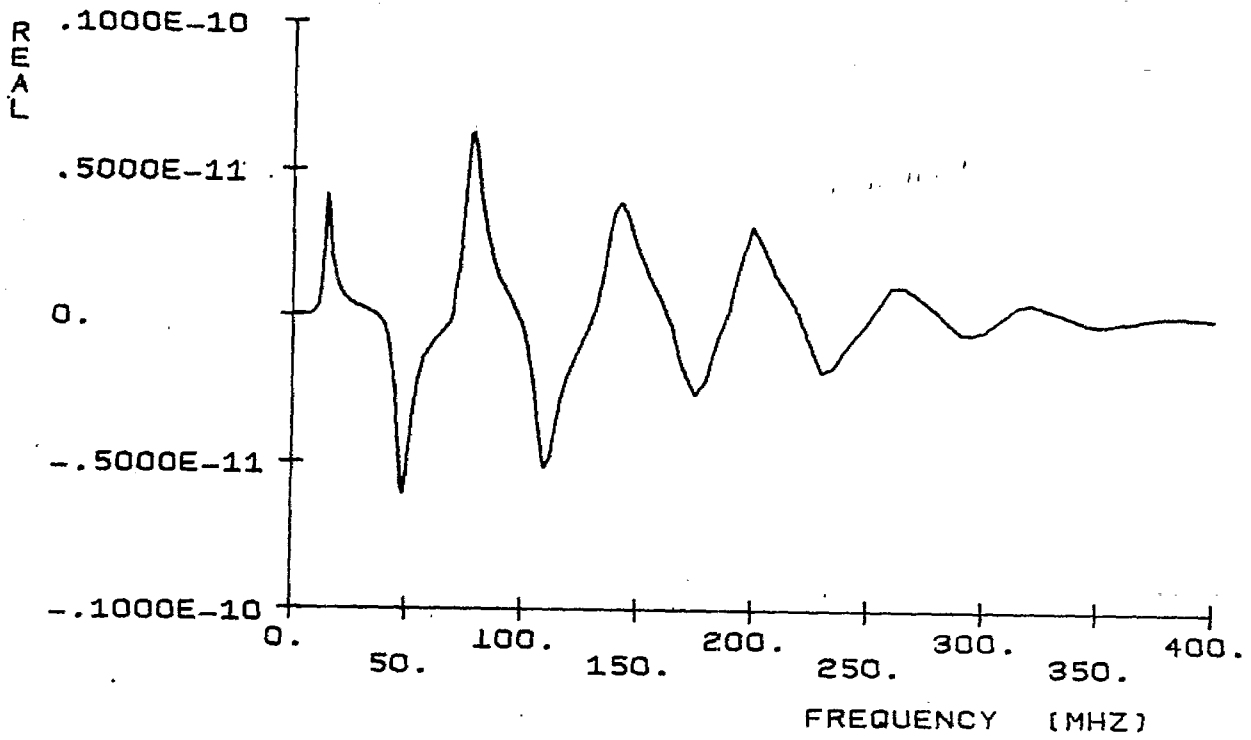
Figure 35. Unloaded frequency domain current I(x,f). Observation point x is on the center of the end patch.

Figure 36.   Loaded (Λ_0 = 40 ohms/m) frequency domain current $I(x,f)$.
Observation point x is on the feed patch.

71
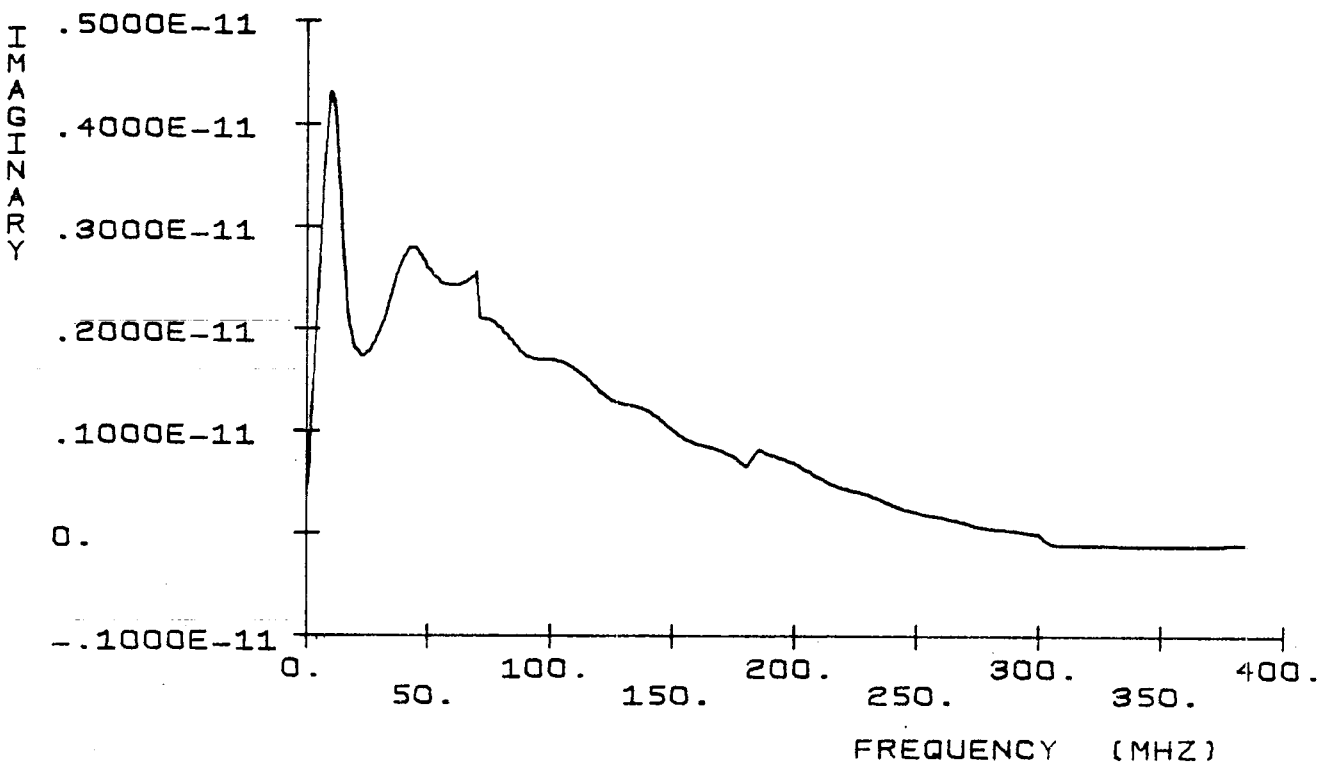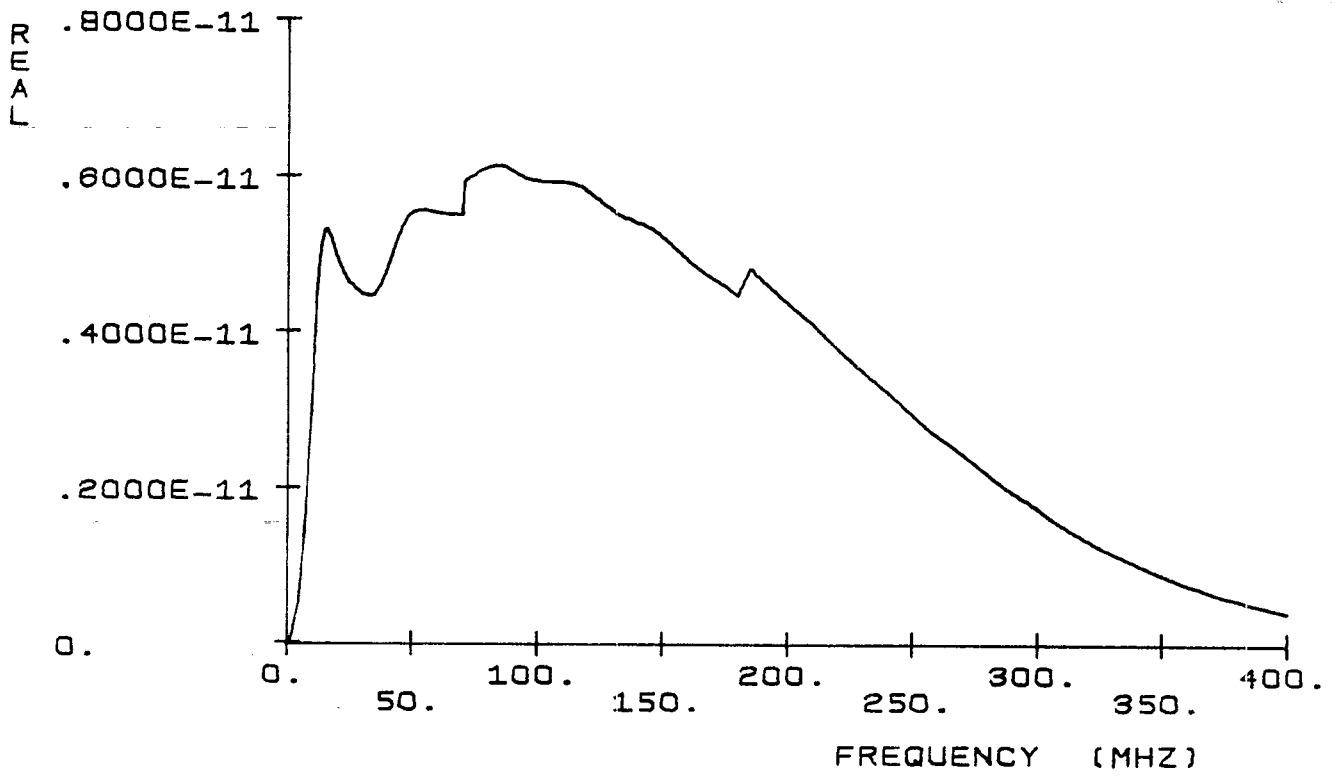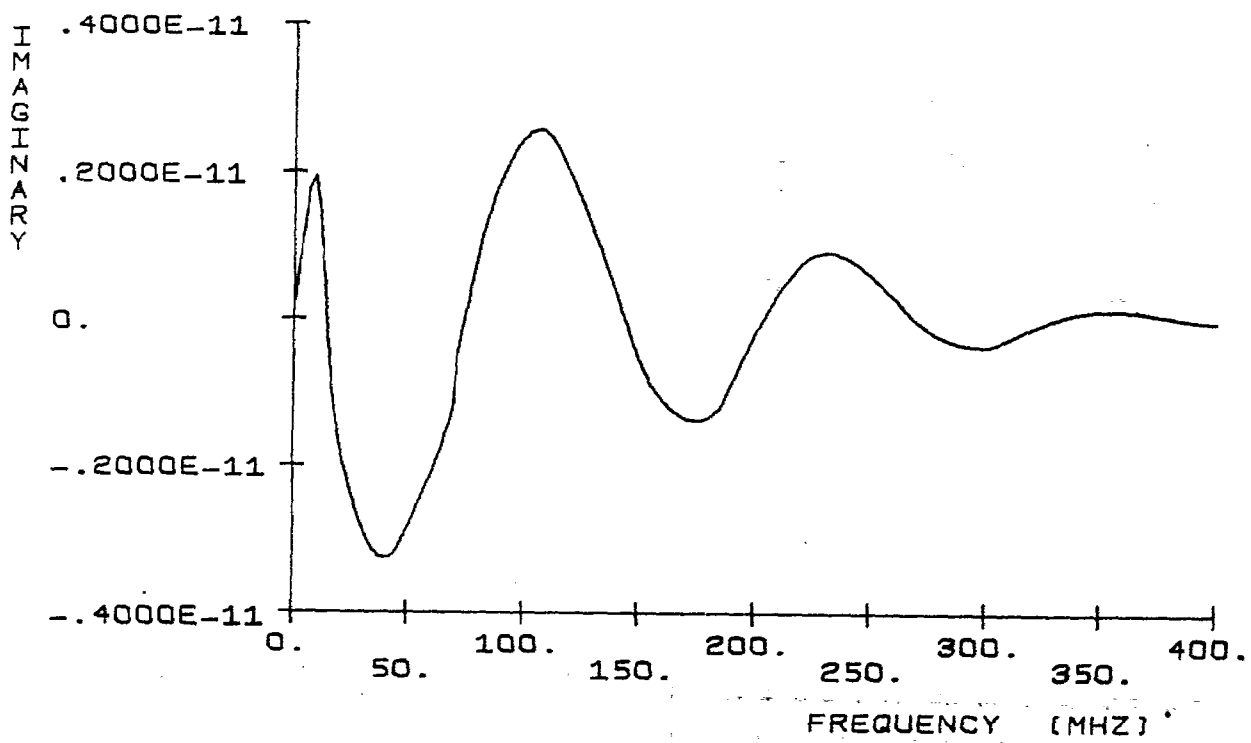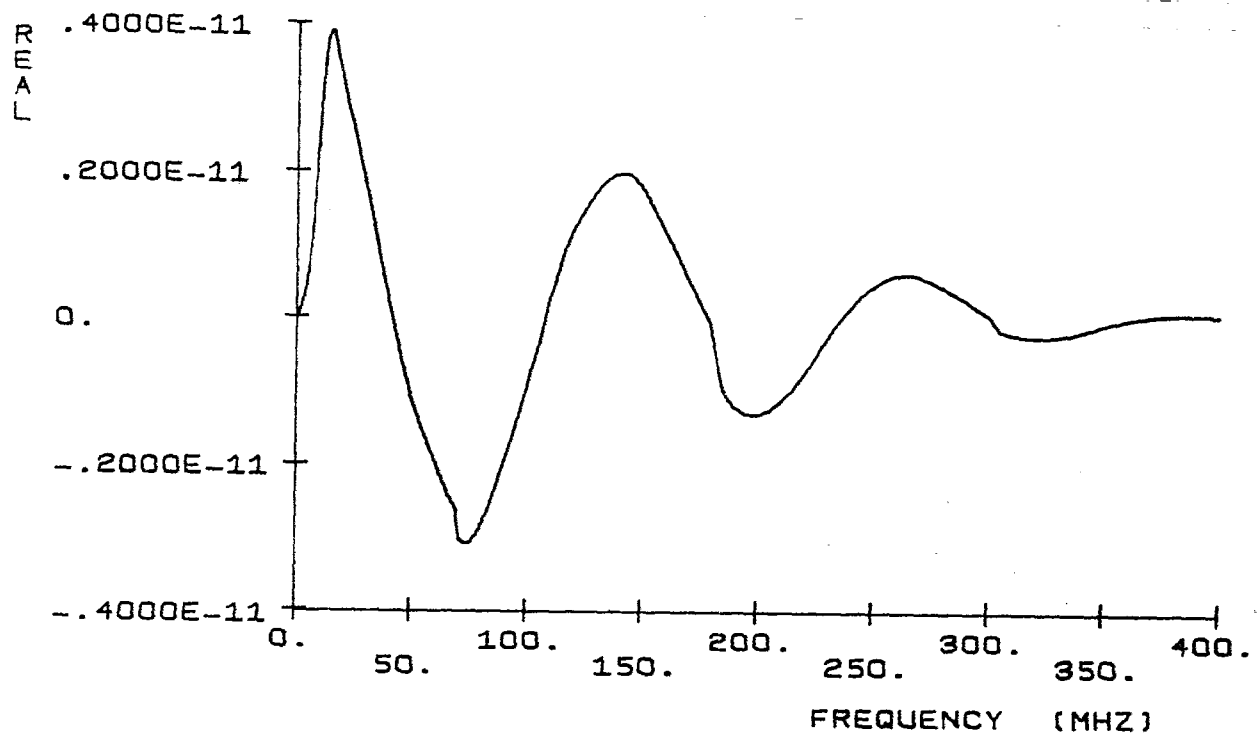
Figure 37. Loaded (Λ_0 = 40 ohms/m) frequency domain current I(x,f). Observation point x is midway between the feed and the end patches.
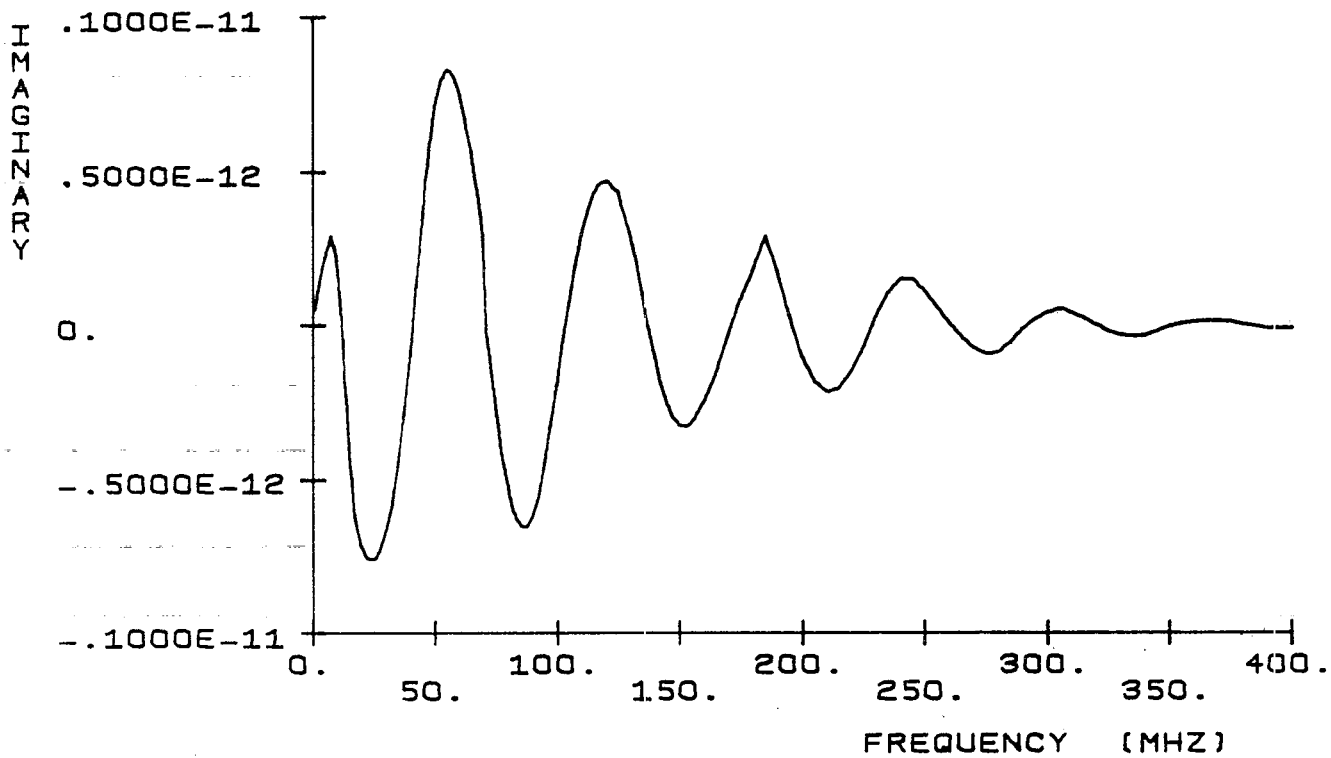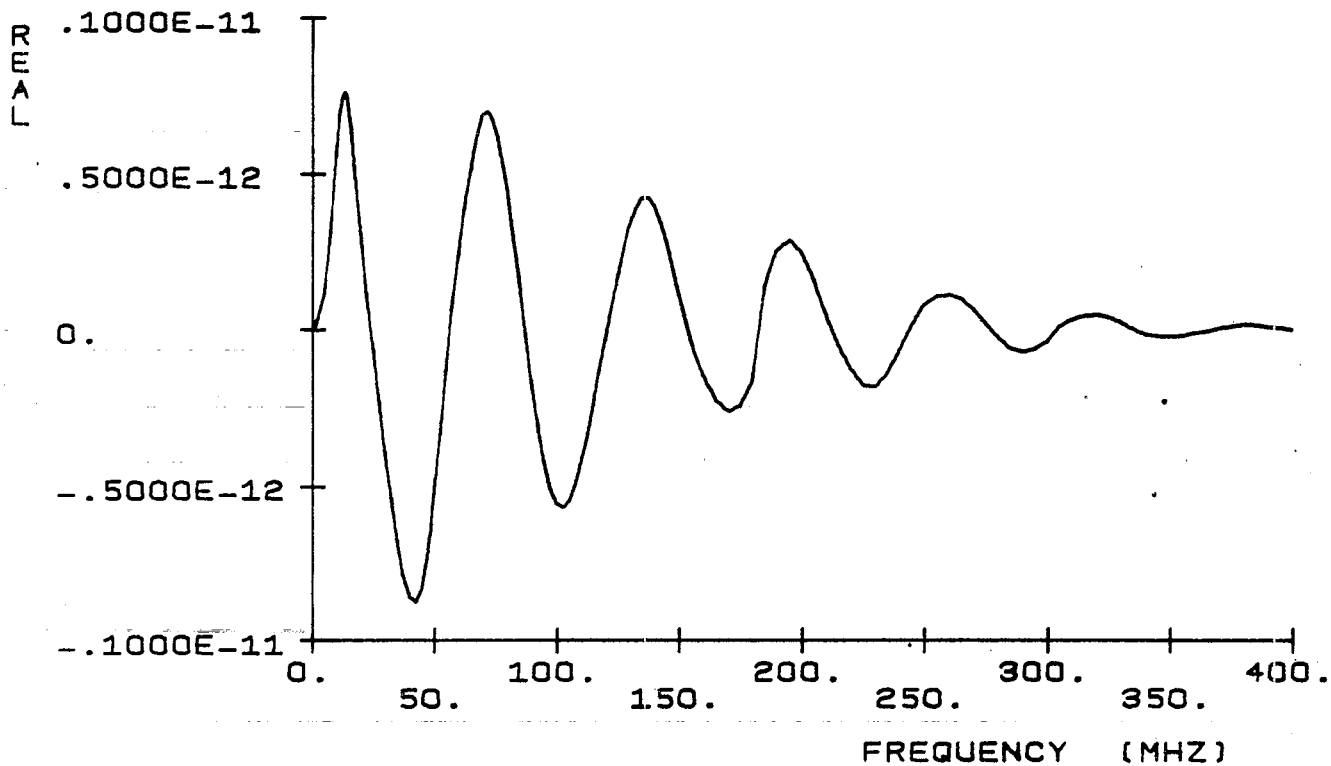
Figure 38.   Loaded (Λ_0 = 40 ohms/m) frequency domain current I(x,f).
Observation point x is on the center of the end patch.
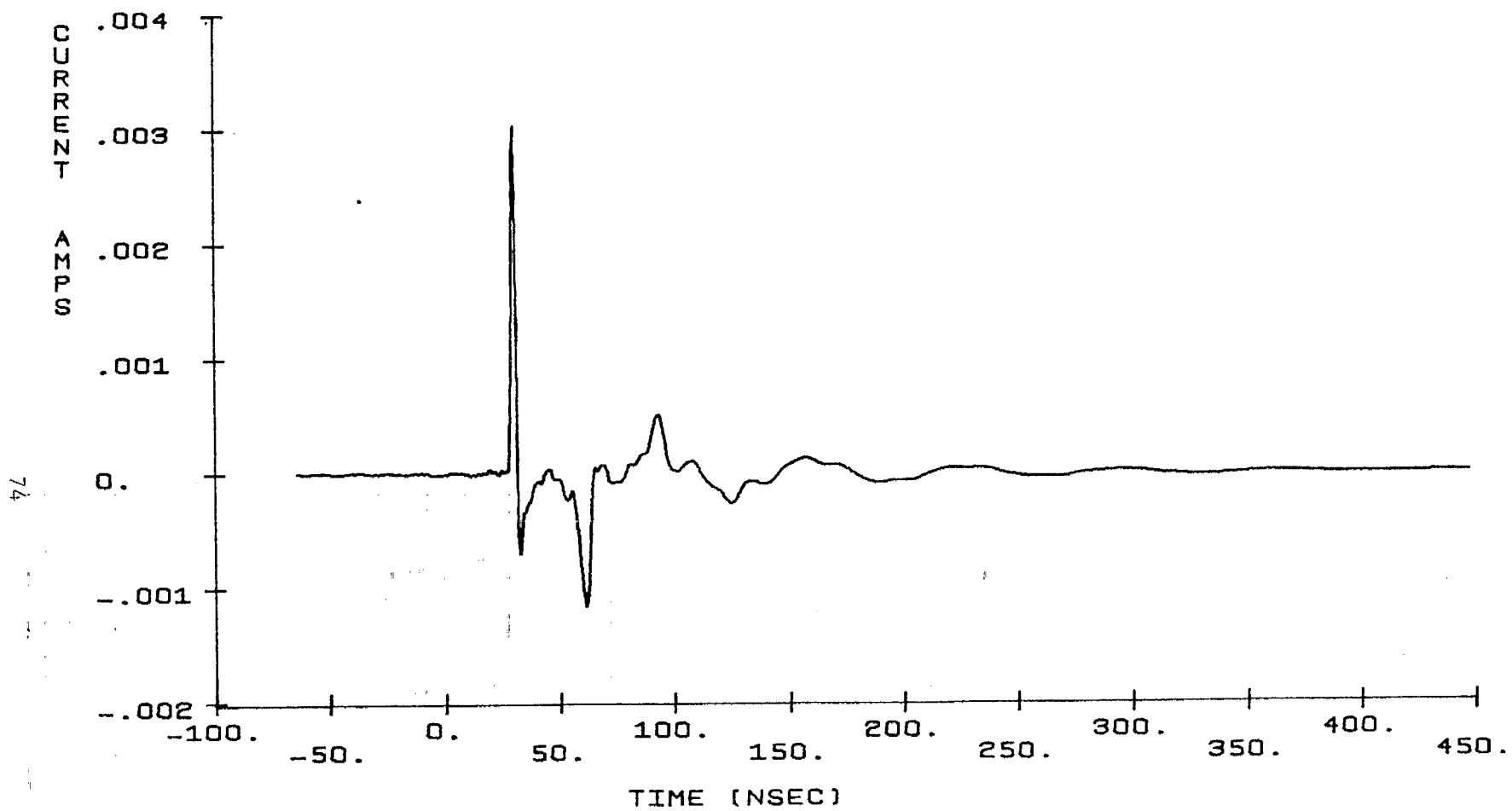
Figure 39.   Unloaded current transient response i(x,t).   Observation point x is on the feed patch.
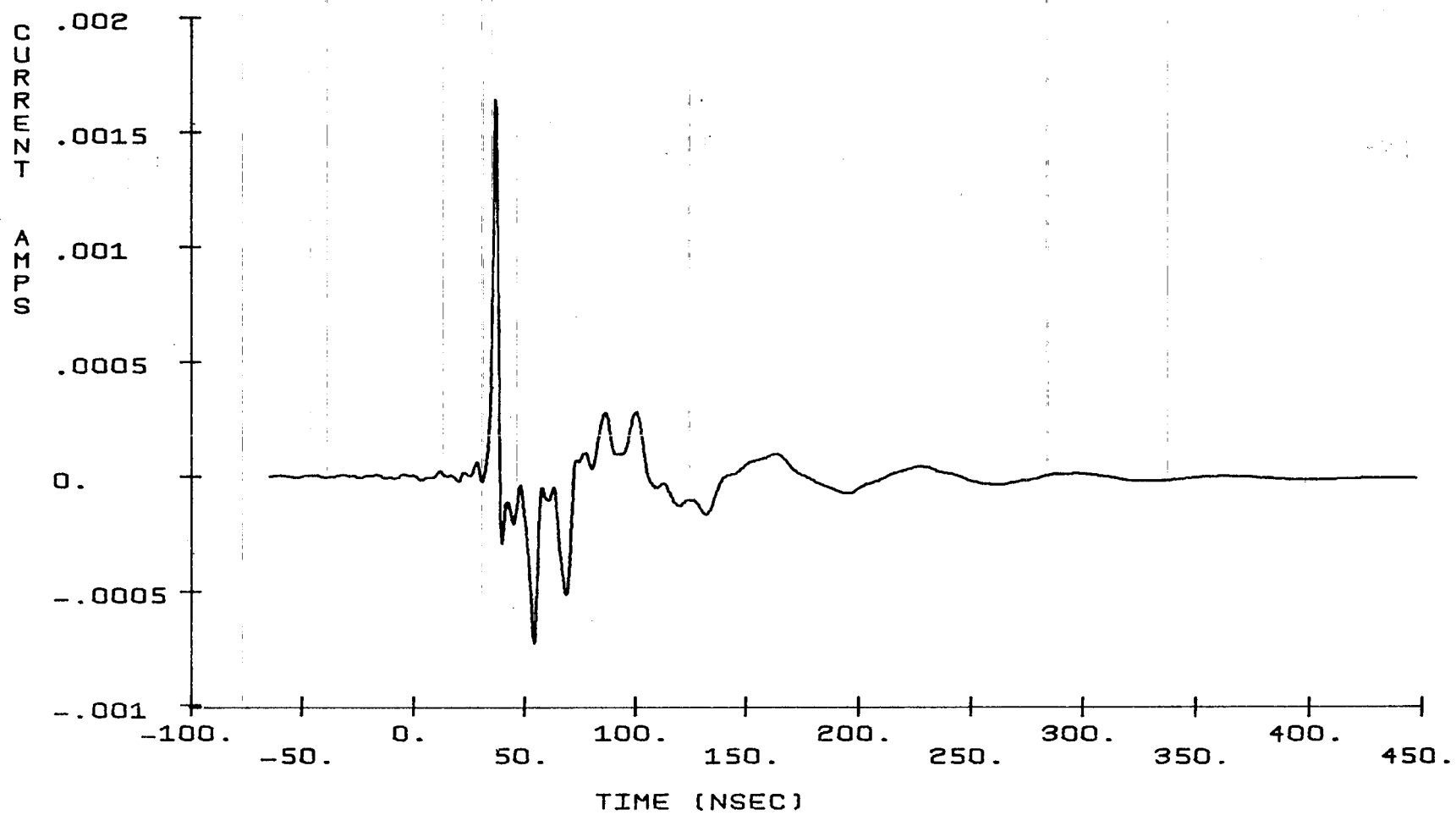
Figure 40. Unloaded current transient response i(x,t). Observation point x is midway between the feed and the end patches.
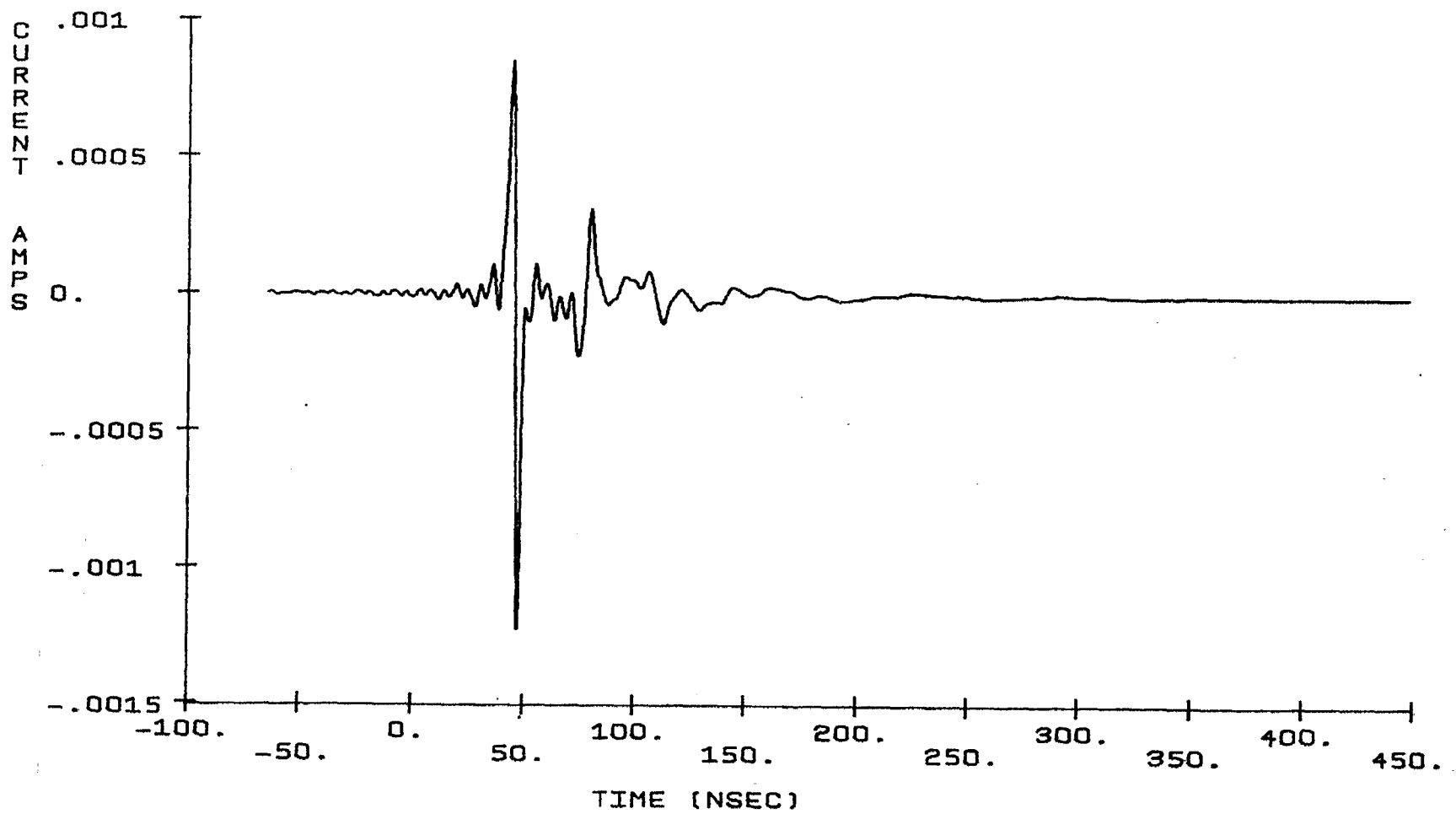
Figure 41. Unloaded current transient response i(x,t). Observation point x is on the center of the end patch.
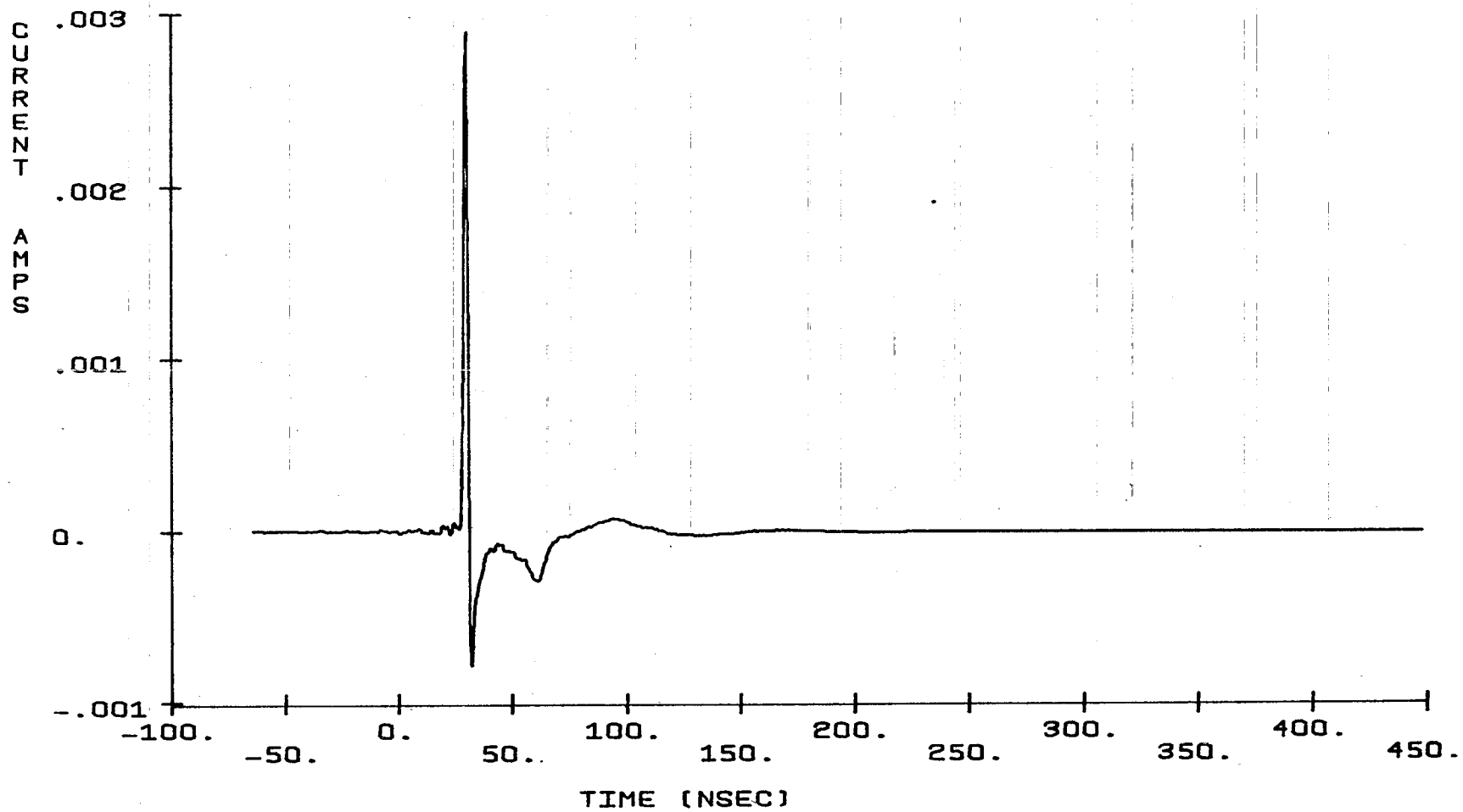
Figure 42. Loaded (Λ_0 = 20 ohms/m) current transient response i(x,t). Observation point x is on the feed patch.
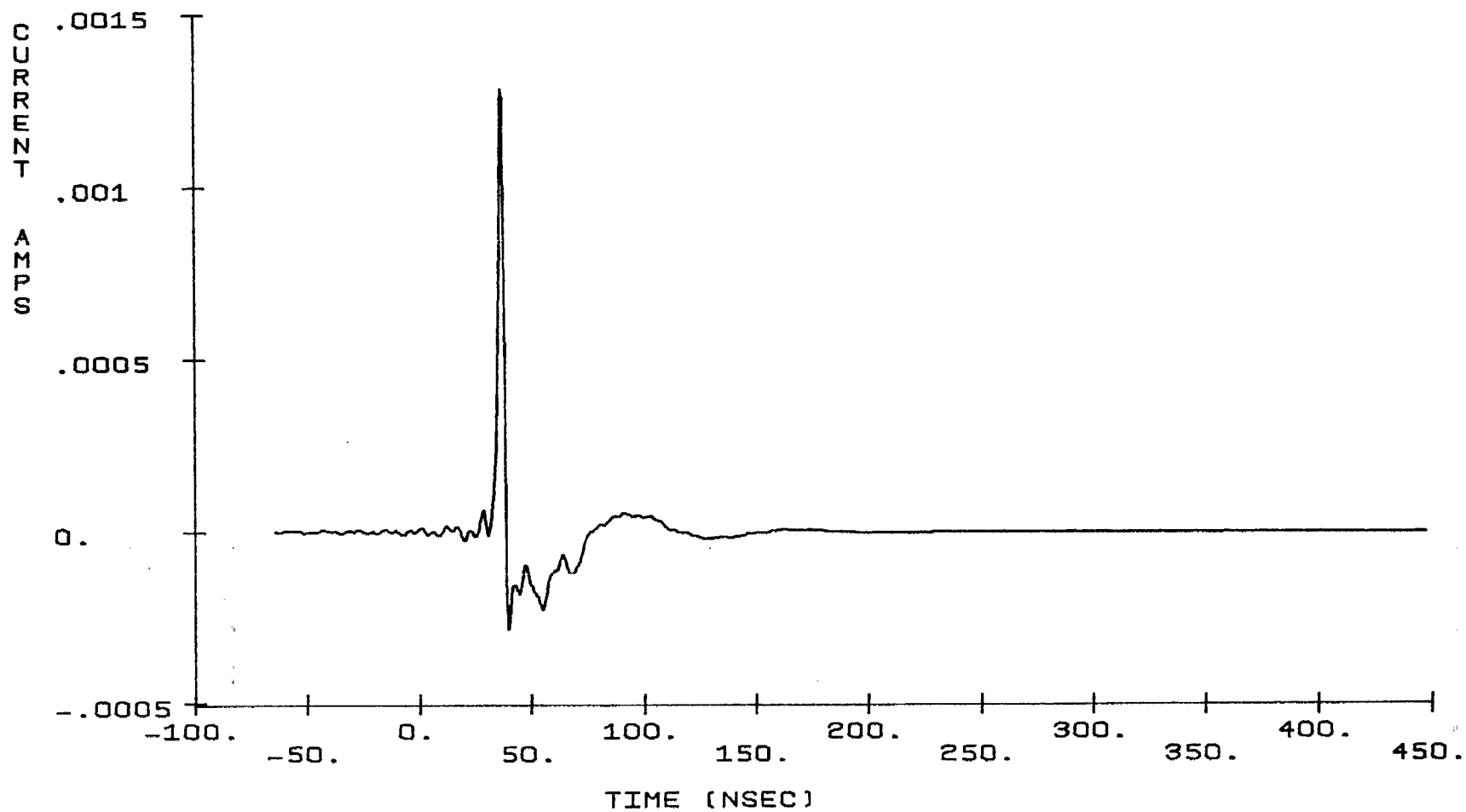
Figure 43. Loaded (Λ_0 = 20 ohms/m) current transient response i(x,t). Observation point x is midway between the feed and the end patches.
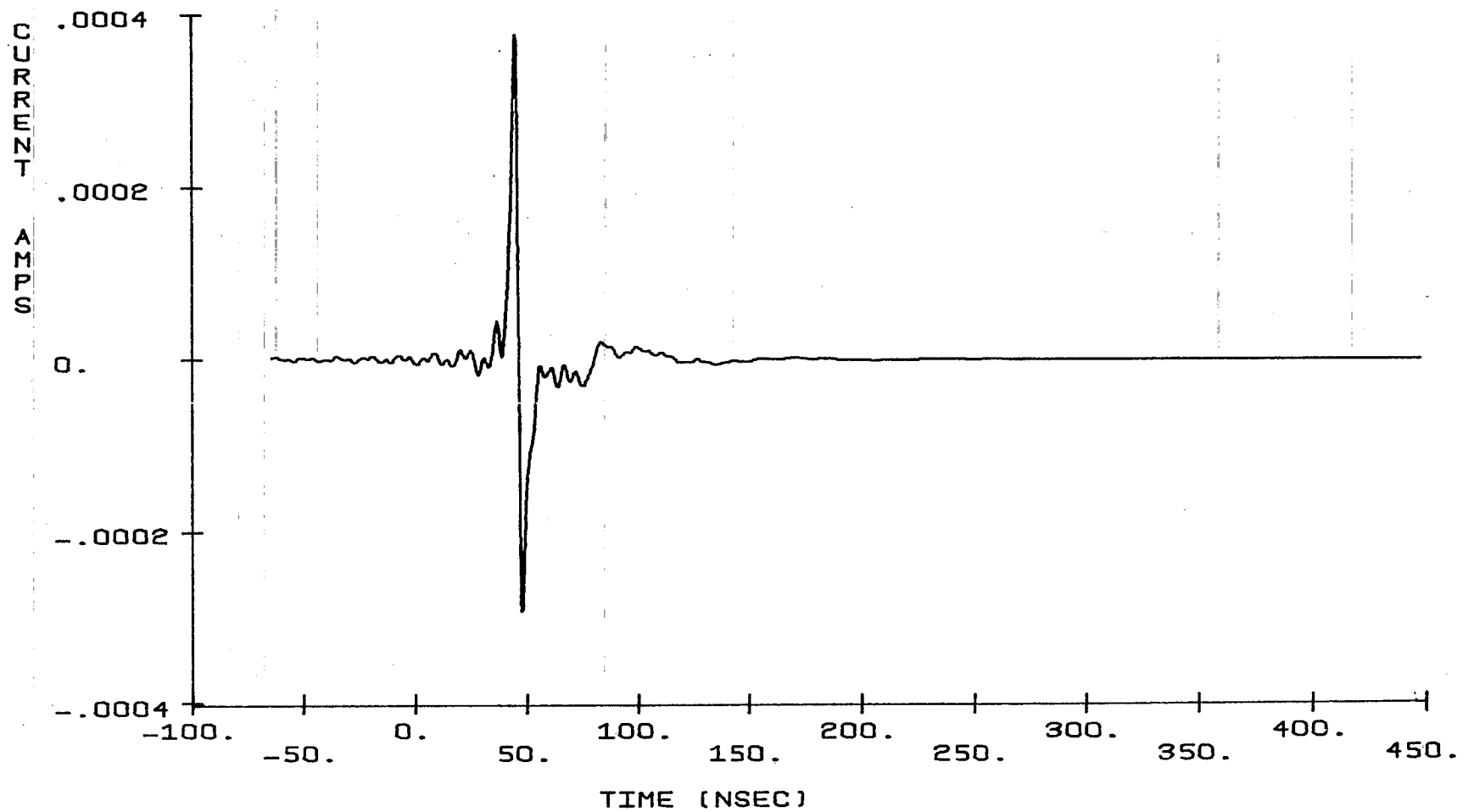
Figure 44. Loaded (Λ_0 = 20 ohms/m) current transient response i(x,t). Observation point x is on the center of the end patch.

Figure 45. Loaded (Λ_0 = 40 ohms/m) current transient response i(x,t). Observation point x is on the feed patch.
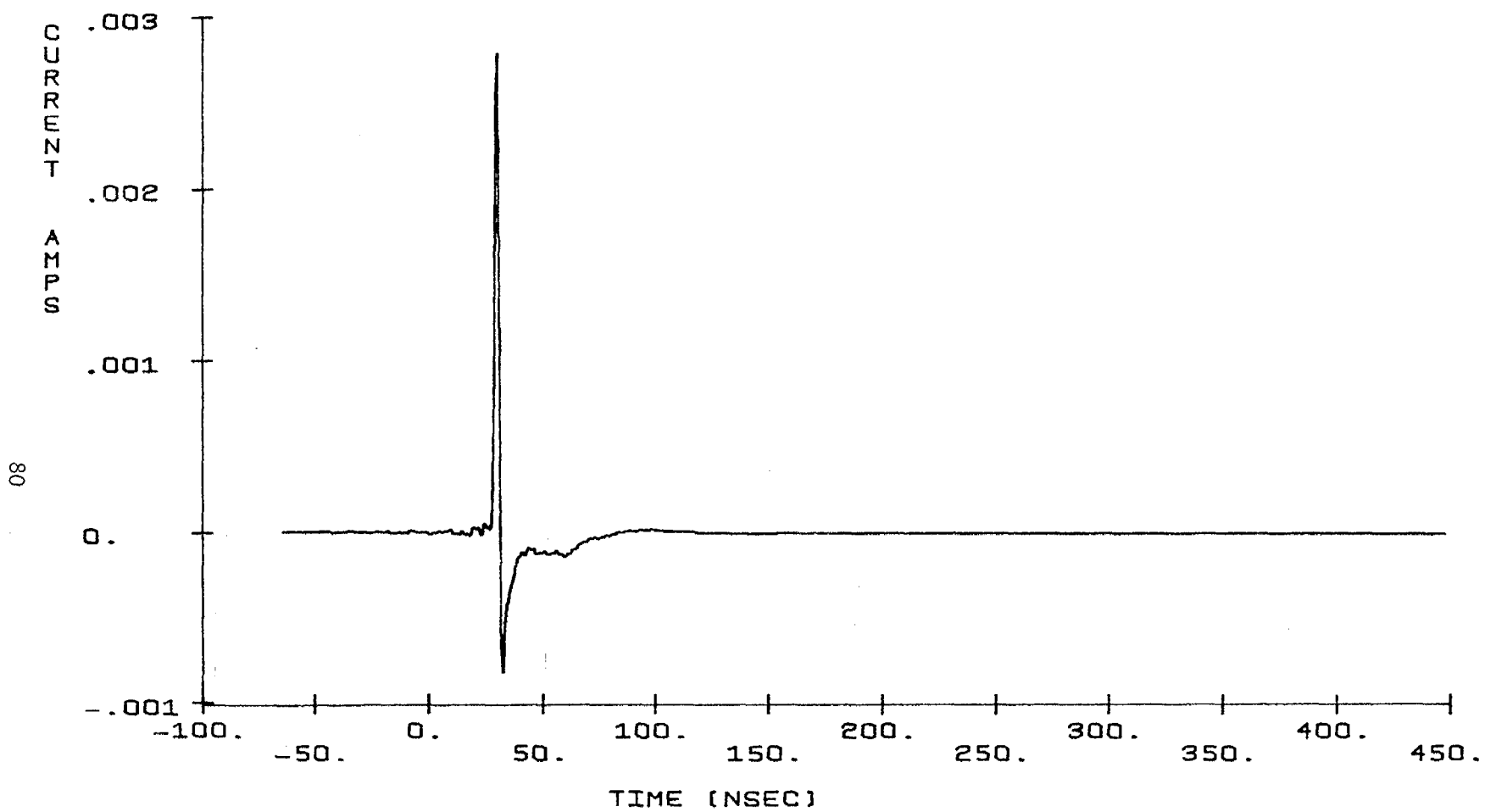
Figure 46. Loaded ($\Lambda_0 = 40$ ohms/m) current transient response i(x,t). Observation point x is midway between the feed and the end patches.

Figure 47. Loaded (Λ_0 = 40 ohms/m) current transient response $i(x,t)$. Observation point x is on the center of the end patch.

can be justified if we assume that the feed excitation travels along the antenna as a TEM mode while being multiply reflected from the antenna end-points. For example, at the center of the antenna (Fig. 39), the reflections from both ends return simultaneously and only one peak is detected per reflection. However, in Fig. 40, the observation point is midway between the feed and the end so that the reflections from the two ends are clearly distinct.

The ringing effect present in the unloaded current transient responses of Figs. 39-41 is partially overcome by the $\Lambda_0 = 20$ ohm/m loading (Figs. 42-44) and has practically disappeared for the $\Lambda_0 = 40$ ohm/m case (Figs. 45-47). This result agrees well with those reported in Appendix III in which the latter loading seemed to be a good approximation to the optimal loading parameters computed for a wide range of frequencies.

6. CONCLUSIONS

A novel procedure has been developed for accurately evaluating the Sommerfeld-type integrals and the integration results are compared with that of the asymptotic approximations. An efficient and fast user-oriented computer program is then developed for computing the current transient response of an arbitrarily loaded, horizontal, linear antenna over a lossy ground. Selective results have compared convincingly with those reported in the literature. This program is currently accurate as long as no poles are intercepted during the path deformations, and the possible branch cut contribution is negligible. Note that for larger θ_2 (see Fig. 5) and as $\sigma \to 0$ (see Fig. 4), chances of capturing a pole and/or a branch point increases, therefore, additional analytical and numerical analysis is needed to take their contributions into account. This work can then be extended to compute the near field of the antenna and will be reported in the near future.

ASYMPTOTIC EVALUATION

In this appendix a general formulation is developed for higher-order asymptotic evaluation of an integral with the following format

$$u = \frac{1}{4\pi j} \int_{\Gamma} P(\xi) \; e^{-jkr\cos(\xi-\theta)} \; d\xi \quad , \tag{I.1}$$

where it is assumed that kr is a large parameter, $-\pi/2 < \theta < \pi/2$ and $P(\xi)$ is a slowly varying function. For large values of kr one is usually interested in determining the asymptotic expression of (I.1). This is done by employing the method of the steepest descent path integration. At the saddle point $\xi = \theta$, one can deform the integration path Γ to the steepest descent path (SDP) defined by $\text{Re}[\cos(\xi - \theta)] = 1$. Assuming that in this deformation no poles or branch points are encountered, one may express (I.1) as

$$u = \frac{1}{4\pi j} \int_{SDP} P(\xi) \; e^{-jkr\cos(\xi-\theta)} \; d\xi \quad . \tag{I.2}$$

Since on SDP the relation $\text{Re}[\cos(\xi - \theta)] = 1$ holds, one introduces the change of variable

$$t = \sqrt{2} \; e^{-j\pi/4} \; \sin \frac{\xi - \theta}{2} \tag{I.3}$$

in which t is a real variable taking the domain $[-\infty, \infty]$. Substituting (I.3) into (I.2), one arrives at

$$u = \frac{e^{-jkr-j\pi/4}}{2\sqrt{2} \; \pi} \int_{-\infty}^{\infty} Q(t) \; e^{-krt^2} \; dt \tag{I.4}$$

where

$$Q(t) = P(\xi) \; \sec \frac{\xi - \theta}{2} \tag{I.5a}$$

in which ξ is replaced with

$$\xi = \pm \left[\frac{\pi}{2} + j Ln(t^2 + j + |t| \sqrt{t^2 + 2j}) \right] + \theta \; , \quad t \gtrless 0 \tag{I.5b}$$

and Ln is interpreted as being its principal value. The complete asymptotic expansion procedure [23] is now used for the asymptotic evaluation of (I.4). In this procedure, one first expands $Q(t)$ in a Taylor series

$$Q(t) = \sum_{n=0}^{\infty} \frac{Q^{(n)}(0)}{\Gamma(n + 1)} \; t^n \tag{I.6}$$

where $Q^{(n)}(0) = \dfrac{\partial^n}{\partial t^n} Q(t) \Big|_{t=0}$ and Γ is the Gamma function. Then (I.6) is substituted into (I.4) to finally result in

$$u = \frac{e^{-jkr - j\pi/4}}{2\sqrt{2\pi}} \sum_{n=0}^{\infty} \frac{2^{-2n}}{n!} (kr)^{-n-1/2} Q^{(2n)}(0) \; . \tag{I.7}$$

In constructing the preceding equation, the following identity was used, viz.,

$$\int_{-\infty}^{\infty} t^n e^{-krt^2} \, dt = \begin{cases} (kr)^{-(1+n)/2} \; \Gamma[(1 + n)/2] & \text{for n even} \\ \\ 0 & \text{for n odd} \end{cases} \tag{I.8}$$

The task is now to determine $Q^{(2n)}$'s in terms of P. This is achieved by differentiating (I.5a) and arriving at

$$\begin{cases} Q(0) = P(\theta) \\[2mm] Q^{(2)}(0) = 2j\left[\dfrac{d^2 P(\xi)}{d\xi^2} + \dfrac{1}{4} P(\xi)\right]_{\xi=\theta} \\[4mm] Q^{(4)}(0) = -4\left[\dfrac{d^4 P(\xi)}{d\xi^4} + \dfrac{5}{2}\dfrac{d^2 P(\xi)}{d\xi^2} + \dfrac{9}{16} P(\xi)\right]_{\xi=\theta} \end{cases} \qquad (I.9)$$

The higher-order terms can also be determined in the same fashion. It is worth emphasizing here that in deriving the preceding equations, the following assumption has been made: neither the poles nor the branch points of $P(\xi)$ are near the path SDP.

To present an example, the higher-order asymptotic expansion of the following Hankel function of the second kind and order ν is derived.

$$H_\nu^{(2)}(\Omega) = \frac{1}{\pi}\int_\Gamma e^{-j\nu\xi + j\nu\pi/2}\, e^{-j\Omega\cos\xi}\, d\xi \quad . \qquad (I.10)$$

Comparing (I.10) with (I.1), one obtains

$$P(\xi) = 4j\, e^{-j\nu\xi + j\nu\pi/2} \quad , \qquad (I.11)$$

where it is assumed that $\Omega \gg \nu$. Substituting (I.11) into (I.9) and simplifying the result, one finally arrives at

$$\begin{cases} Q(0) = 4j\, e^{j\nu\pi/2} \\[2mm] Q^{(2)}(0) = -8\left[-\nu^2 + \dfrac{1}{4}\right] e^{j\nu\pi/2} \\[3mm] Q^{(4)}(0) = -16j\left[\nu^4 - \dfrac{5}{2}\nu^2 + \dfrac{9}{16}\right] e^{j\nu\pi/2} \end{cases} \qquad (I.12)$$

The asymptotic expansion of $H_\nu^{(2)}$ is then determined using (I.7) to be

87

$$H_\nu^{(2)}(\Omega) = \sqrt{\frac{2}{\pi\Omega}}\ e^{-j(\Omega - \nu\pi/2 - \pi/4)}\left[1 + \frac{j}{2\Omega}\left(\frac{1}{4} - \nu^2\right) - \frac{1}{8\Omega^2}\left(\nu^4 - \frac{5}{2}\nu^2 + \frac{9}{16}\right)\right]$$

$$+\ 0(\Omega^{-7/2}) \qquad . \tag{I.13}$$

The purpose of this appendix has been to formulate the necessary steps for determining the asymptotic expansion of (3.1). Comparing (3.1) and (3.2) with (I.1) and using (I.13) in (3.2), one can then find the asymptotic expansion of (3.1) from (I.7). Since the final results take a complicated form, the following notations are introduced for the ease of representation, namely,

$$c = \cos\theta_2 \tag{I.14a}$$

$$s = \sin\theta_2 \tag{I.14b}$$

$$q = \sqrt{\kappa - \sin^2\theta_2} \qquad . \tag{I.14c}$$

Using (I.9) and performing a rather tedious differentiation, one finally arrives at

$$Q(0) = I_0 k_1 \sqrt{\frac{2}{\pi k_1 r_2}}\ e^{j\pi/4}\left[1 + \frac{j}{8k_1 r_2 s^2}\right]\frac{c}{c + q} \tag{I.15}$$

and

$$Q^{(2)}(0) = I_0 k_1 \sqrt{\frac{2}{\pi k_1 r_2}}\ e^{j\pi/4}\ (2j)\left\{-\frac{c^3}{4s^2(c + q)} + \frac{2c^2 - 3cq}{4q(c + q)}\right.$$

$$\left. +\ (1 - \kappa)\frac{4qs^2 + 3cq^2 + 2cs^2}{2q^3(c + q)^2}\right\} \qquad . \tag{I.16}$$

Clearly, the terms for $Q^4(0)$ get very involved and therefore are not included here. It is interesting to note that both the second term in (I.15) and the first term in (I.16) are singular at $s = 0$, i.e., $\theta_2 = 0$. Substituting (I.15) and (I.16) back into (I.7) and simplifying the result, one clearly observes that these singularities together produce a bounded result at $\theta_2 = 0$. In other words, though the asymptotic construction was not originally valid for $\theta_2 = 0$, the final solution can be used for this angle. This solution takes the following form

$$_0\Pi^r_{1x} = I_0 \frac{2c}{c + q} \frac{e^{-jk_1 r_2}}{4\pi r_2} + 0\left(k_1^{-2} r_2^{-2}\right) \quad , \tag{I.17}$$

and

$$_0\Pi^r_{1x} = I_0 \frac{2c}{c + q} \frac{e^{-jk_1 r_2}}{4\pi r_2} + \frac{j}{2} I_0 \left[\frac{c(c - q)}{q(c + q)} + (1 - \kappa) \frac{4qs^2 + 3cq^2 + 2cs^2}{q^3(c + q)^2}\right]$$

$$\cdot \frac{e^{-jk_1 r_2}}{4\pi k_1 r_2^2} + 0\left(k_1^{-3} r_2^{-3}\right) \quad . \tag{I.18}$$

It must be realized that the preceding asymptotic results are valid only for observation angles $\theta_2 < \theta_c$, where θ_c is the critical angle for which the saddle path of (3.1) intercepts the branch point of the integrand. For the cases where the interception happens, one has to determine the asymptotic contribution of the branch point near the saddle point. The procedure is discussed in [14] and it can be shown that the final result would be of the order $k_1^{-2} r_2^{-2}$, i.e., the same order as the second term in (I.18). Therefore, as far as $k_1 r_2$ is large and the branch points and poles are sufficiently away from the saddle point, one can use (I.17) with confidence for almost all angles of observation.

APPENDIX II.

EVALUATION OF $_0\Pi^r_{1x}$ AT $\theta_2 = 0$

In this appendix the behavior of (2.37) and (2.40) at $\rho_2 = 0$ is studied. In their present forms, these integrals are not defined at $\rho_2 = 0$, although it is clear that their equivalent form in (2.34) is bounded. Equation (2.37) may be expressed here for convenience as

$$_0\Pi^r_{1x} = \frac{I_0}{4\pi j} \int_{-\infty}^{\infty} \frac{\lambda}{\sqrt{k_1^2 - \lambda^2} + \sqrt{\kappa k_1^2 - \lambda^2}} H_0^{(2)}(\rho_2\lambda) \, e^{-jz_2\sqrt{k_1^2 - \lambda^2}} \, d\lambda \qquad (II.1)$$

where $\rho_2 = r_2 \sin\theta_2$. From Fig. 1 it is observed that $r_2 \geq h$ and $0 \leq \theta_2 \leq \pi/2$, and therefore the difficulty arises at $\theta_2 = 0$.

To circumvent this difficulty, one replaces $H_0^{(2)}$ with its expansion from [24]

$$H_0^{(2)}(\rho_2\lambda) = J_0(\rho_2\lambda) - j\left[\frac{2}{\pi} \ln \frac{\gamma\rho_2\lambda}{2} J_0(\rho_2\lambda) \right.$$
$$\left. + \frac{2}{\pi} \sum_{m=1}^{\infty} \frac{(-1)^{m+1}}{(m!)^2} \left(\frac{\rho_2\lambda}{2} \right)^{2m} \phi(m) \right] \qquad (II.2)$$

where γ is the Euler's constant and $\phi(m)$ represents the harmonic series, i.e.,

$$\phi(m) = 1 + 1/2 + 1/3 + \ldots + 1/m \quad . \qquad (II.3)$$

Using the fact that $\rho_2 = r_2 \sin\theta_2$, one may express the "$\ln$" term as

$$\ln \frac{\gamma\rho_2\lambda}{2} = \ln \frac{\gamma \sin\theta_2}{2} + \ln(r_2\lambda) \quad . \qquad (II.4)$$

90

It is noted that both the J_0 and the summation terms in (II.2) are even functions of λ, hence, their contributions to the integral (II.1) will be zero.

Using (II.4) in (II.2) and substituting the result into (II-1), one finally arrives at

$$_0\Pi_{1x}^r = \frac{I_0}{4\pi j} \int_{-\infty}^{\infty} \frac{\lambda}{\sqrt{k_1^2 - \lambda^2} + \sqrt{\kappa k_1^2 - \lambda^2}} \; \frac{-2j}{\pi} \; J_0(r_2 \sin \theta_2 \; \lambda)$$

$$\cdot \; \ell n(r_2 \lambda) \; e^{-jz_2\sqrt{k_1^2-\lambda^2}} \; d\lambda \quad , \tag{II.5}$$

which is obviously bounded at $\theta_2 = 0$. Introducing the change of variable $\lambda = k_1 \sin \xi$ into (II.5) and setting $\theta_2 = 0$, one finds

$$_0\Pi_{1x}^r = \frac{I_0 k_1}{4\pi j} \int_{\Gamma} \frac{\sin \xi \cos \xi}{\cos \xi + \sqrt{\kappa - \sin^2 \xi}} \; \frac{-2j}{\pi} \; \ell n(k_1 r_2 \sin \xi)$$

$$\cdot \; e^{-jk_1 r_2 \cos\theta_2 \cos\xi} \; d\xi \quad , \quad \theta_2 = 0 \quad . \tag{II.6}$$

The above result was used in (3.12) for defining $P(\xi)$. In a similar fashion, one can show that the following results also hold at $\theta_2 = 0$

$$\begin{cases} \Pi_{1z}^r = 0 \\[2mm] \dfrac{\partial}{\partial z} \Pi_{1z}^r = 0 \quad . \end{cases} \tag{II.7}$$

91

REFERENCES

1. Special Joint Issue on the Nuclear Electromagnetic Pulse, IEEE Trans. on Antennas and Propagation, January 1978 and also in IEEE Trans. on Electromagnetic Compatibility, February 1978.

2. L.B. Felsen, Ed., Transient Electromagnetic Fields, Topics in Applied Physics, Vol. 10, New York: Springer-Verlag, 1976.

3. E.K. Miller, A.J. Poggio, G.J. Burke, and E.S. Selden, "Analysis of Wire Antennas in the presence of a Conducting Half-Space. Part I. The Vertical Antenna in Free Space," Canadian J. of Physics, Vol. 50, pp. 879-888, 1972.

4. E.K. Miller, A.J. Poggio, G.J. Burke and E.S. Selden, "Analysis of Wire Antennas in the Presence of Conducting Half-Space: Part II. The Horizontal Antenna in Free Space," Canadian J. of Physics, Vol. 50, pp. 2614-2627, 1972.

5. J.D. McCannon, "A Comparative Numerical Study of Several Methods for Analyzing a Vertical Thin-Wire Antenna Over a Lossy Half-Space," PhD. Thesis, University of Illinois, Urbana, Illinois, 1974.

6. T.K. Sarkar and B.J. Strait, "Analysis of Arbitrarily Oriented Thin Wire Antenna Arrays Over Imperfect Ground Planes," Scientific Report No. 9 on contract F19628-73-C-0047, AFCRL-TR-75-0641, Syracuse University, Syracuse, New York, December 1975.

7. A. Sommerfeld, Partial Differential Equations in Physics, New York: Academic Press, 1964.

8. J.R. Wait, "The Electromagnetic Fields of a Horizontal Dipole in the Presence of a Conducting Half-Space," Canadian J. of Physics, Vol. 39, pp. 1017-1028, 1961.

9. A. Banos, Dipole Radiation in the Presence of Conducting Half-Space, New York: Pergamon Press, 1966.

10. D.L. Lager and R.J. Lytle, "Numerical Evaluation of Sommerfeld Integrals," Lawrence Livermore Laboratory," Report UCRL-51688, October 23, 1974.

11. D.L. Lager and R.J. Lytle, "Fortran Subroutines for the Numerical Evaluation of Sommerfeld Integrals Under Anderem'," Lawrence Livermore Laboratory," Report UCRL-51821, May 21, 1975.

12. J.A. Kong, L.C. Shen, and L. Tsang, "Field of an Antenna Submerged in a Dissipative Dielectric Medium," IEEE Trans. Antennas Propagat., Vol. AP-25, pp. 887-889, November 1977.

13. J.N. Brittingham, E.K. Miller, J.T. Okada, "Bivariate Interpolation Approach for Efficiently and Accurately Modelling Antennas Near a Half-Space," Electronics Letters, Vol. 13, pp. 690-691, Nov. 1977

14. J.A. Kong, _Theory of Electromagnetic Waves_, New York: Wiley, 1975.

15. L. Grun, Y. Rahmat-Samii, "Polynomial Approximations of Bessel, Neumann and Hankel Functions for Complex Arguments," University of Illinois at Urbana-Champaign, Electromagnetic Laboratory, Technical Report No. 77-15, July 1975.

16. R.F. Harrington, _Field Computation by Moment Methods_, New York: McMillan, 1968.

17. P. Parhami, Y. Rahmat-Samii, R. Mittra, "A Technique for Calculating the Radiation and Scattering Characteristics of Antennas Mounted on a Finite Ground Plate," _Proc. IEEE_, Vol. 124, pp. 1009-1016, Nov. 1977.

18. R.F. Harrington, "Matrix Methods for Field Problems," _Proc. IEEE_, pp. 136-149, February 1967.

19. E.C. Jordan and K.G. Balmain, _Electromagnetic Waves and Radiating Systems_, pp. 566-567, New Jersey: Prentice Hall, 1968.

20. C.M. Butler and D.R. Wilton, "Analysis of Various Numerical Techniques Applied to Thin-Wire Scatterers," _IEEE Trans. Antennas Propagat_. Vol. AP-23, pp. 534-540, July 1975.

21. Y.P. Liu, D.L. Sengupta, and C.T. Tai, "On the Transient Wave Forms Radiated by a Resistively Loaded Linear Antenna," _Sensor and Simulation Notes_, Note 178, February 1973.

22. F.M. Tesche, "Application of the Singularity Expansion Method to the Analysis of Impedance Loaded Linear Antennas," _Sensor and Simulation Notes_, Note 177, May 1973.

23. L.B. Felsen and N. Marcuvitz, _Radiation and Scattering of Waves_, New Jersey: Prentice Hall, 1973.

24. R.F. Harrington, _Time Harmonic Fields_, New York: McGraw-Hill, 1961.

LOADED HORIZONTAL ANTENNA OVER
AN IMPERFECT GROUND

Y. Rahmat-Samii, P. Parhami, and R. Mittra

Electromagnetics Laboratory
Department of Electrical Engineering
University of Illinois at Urbana-Champaign
Urbana, Illinois 61801

ABSTRACT

The Fresnel reflection coefficient technique is employed to establish
an E-field integral equation for the antenna current. A resistive loading
of the form $R(x) = R_0/(1-|x|/L)$ is used to load the antenna. An optimiza-
tion technique is discussed for determining the value of critical loading,
R_0^c, which enforces a traveling wave current on the antenna. Results are given
for the critical loading parameters, antenna currents, input impedances and
radiation patterns versus different antenna dimensions and ground permitti-
vities and conductivities.

LIST OF FIGURES

LIST OF TABLES

I.   INTRODUCTION

Loaded wire antennas, which have attracted attention in designing EMP simulators, often are regarded as open simulators. The basic design requirement is to generate a temporal signal which matches the waveform of an exoatmospheric burst [1] which is typically characterized by rise and fall times of approximately tens and hundreds of nsecs, respectively. The basic obstacle in using any pulse radiating finite antenna is the undesirable effect due to the reflection from the antenna ends. The effect of these reflections is predominantly seen in the early time behavior of the radiated pulse. Usually the antenna dimension (length) is several $\lambda/2$ (wavelength) for the upper part of the frequency spectrum of the pulse. One possible way to overcome these difficulties is to load the antenna with a non-uniform resistive loading (frequency independent) which eliminates the end reflections to a great extent.

Many different loading functions have been proposed and tested for antennas in free space. Liu, Sangupta and Tai [2] have analyzed and compared the effect of different loadings and have concluded that the following continuous loading is the most suitable one:

$$\Lambda(x) = \frac{\Lambda_0}{1 - |x|/L} \tag{1}$$

where x is measured along the antenna from its center and 2L is the antenna length. They used the method of moments with quadratic basis function and determined the critical value of Λ_0 by trial and error algorithm, i.e., by looking at the current distribution and searching for a traveling wave-type behavior. Tesche [3] has arrived at almost the same conclusion by applying the singularity expansion method.

In this paper, we analyze the effect of loading with characteristic function (1) for antennas over an imperfect ground, and specifically devise a novel approach for the determination of the critical loading. We use the Fresnel reflection coefficient approach and derive an E-integral equation for the antenna current. The effect of loading then appears as a diagonal term in the matrix equation formulation. Since for the critical loadings, the current phase distribution is almost linear along the antenna [2], we use this fact to develop our procedure. For a given value of Λ_0, the current phase distribution is determined. On one side of the feed, the phases are interpolated numerically by a best fit straight line and the resultant least square error is then associated with the Λ_0 parameter. The procedure then is simply a search for an optimized value of Λ_0 (critical loading) by minimizing the least square error. The phase obtained in this manner is almost linear except at the feed and end points where radiation occurs, which guarantees an almost reflectionless current distribution on the antenna. Results are given for the critical loading parameters, antenna currents, input impedances and radiation patterns, versus various different antenna dimensions and ground paramters.

II. BASIC FORMULATION

In deriving an integral equation for the antenna current, knowledge
of the radiated field from a current element is needed. The major steps
in constructing this field will be briefly discussed in this section.
The geometry of a current element P_1 over an imperfect ground is depicted
in Figure 1. Regions 1 and 2 are characterized by ($\varepsilon_1 = \varepsilon_0$, $\mu_1 = \mu_0$,
$\sigma_1 = 0$) and ($\varepsilon_2 = \varepsilon_r \cdot \varepsilon_0$, $\mu_2 = \mu_0$, $\sigma_2 = \sigma$), respectively, where ε_0 and μ_0
are free-space parameters. The current element is in the x-direction
(horizontal) and its coordinates are (x´, y´, z´). Furthermore, the
geometrical image of P_1 is designated by P_2 and their distances from the
observation point 0 (x, y, z) are labelled as $P_1 0 = R_1$ and $P_2 0 = R_2$,
respectively. Our objective is to find the radiated field of P_1 at the
observation point 0 in the presence of the imperfect ground.

As originally observed by Sommerfeld [4], two components of the
Hertz potential are needed for a complete description of the horizontal
current element problem. However, for the vertical case only one component
would be sufficient. The two components are chosen to be in the x and z
directions, i.e., along the current element and along the normal to the
interface, and are designated as follows

$$\vec{\Pi} = \Pi_x \hat{x} + \Pi_z \hat{z} \quad . \tag{2}$$

Later in this paper, quantities like Π_{1x}, Π_{2x}, etc., will be used which
specifically define these quantities in regions 1 and 2, respectively.
Employing Maxwell's equation and using the Lorentz guage, one arrives at

$$\nabla^2 \vec{\Pi} + k^2 \vec{\Pi} = -(j\omega\varepsilon)^{-1} \vec{J} \tag{3a}$$

$$\vec{H} = j\omega\varepsilon \nabla \times \vec{\Pi} \tag{3b}$$

$$\vec{E} = \nabla\nabla \cdot \vec{\Pi} + k^2 \vec{\Pi} \tag{3c}$$
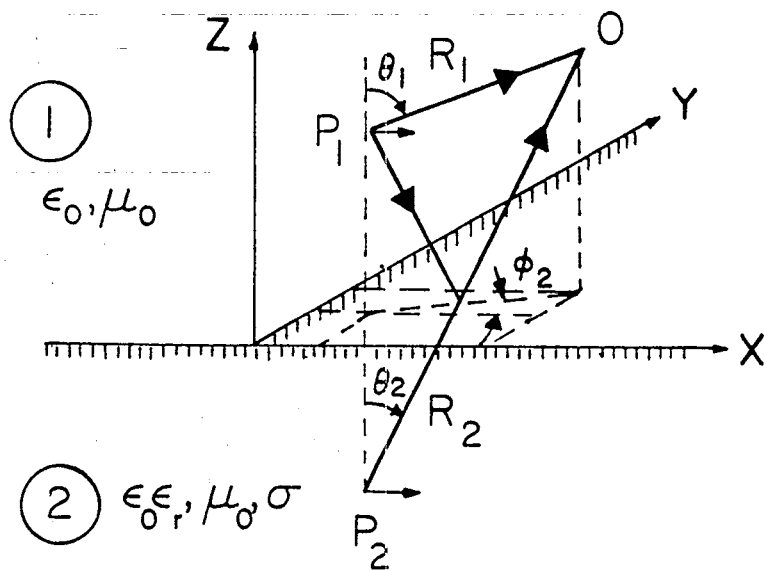
Fig. 1. Horizontal current element P_1 over an
imperfect ground.

where $\vec{E}$, $\vec{H}$ and $\vec{J}$ are the electric field, magnetic field and current source, respectively. Furthermore, throughout this work, the time convention $\exp(j\omega t)$ is used and suppressed in the formulations. For the problem at hand, the only source term is

$$\vec{J}_1 = \hat{x} I\, dx'\; \delta(x - x')\; \delta(y - y')\; \delta(z - z') \qquad , \qquad (4)$$

where $I\, dx'$ is the current element moment.

The continuity of the tangential $\vec{E}$ and $\vec{H}$ fields at the interface results in the following boundary conditions

$$\frac{\partial}{\partial x}\, \Pi_{1x} + \frac{\partial}{\partial z}\, \Pi_{1z} = \frac{\partial}{\partial x}\, \Pi_{2x} + \frac{\partial}{\partial z}\, \Pi_{2z} \qquad (5a)$$

$$\Pi_{1x} = \kappa\, \Pi_{2x} \qquad (5b)$$

$$\Pi_{1z} = \kappa\, \Pi_{2z} \qquad (5c)$$

$$\frac{\partial}{\partial z}\, \Pi_{1x} = \kappa\, \frac{\partial}{\partial z}\, \Pi_{2x} \qquad (5d)$$

where $\kappa = \varepsilon_2/\varepsilon_1 = \varepsilon_r - j\sigma(\omega\varepsilon_0)^{-1}$. Our goal at this point is to determine Π_{1x} and Π_{1z}. The boundary value problem (3) – (5) has an exact solution in terms of the well-known Sommerfeld integrals. These integrals take many different forms [5,6,7], and the following versions will be used for simplicity

$$\Pi_{1x} = \Pi_{1x}^i + \Pi_{1x}^r \qquad (6)$$

where

$$\Pi_{1x}^i = I_0\, \frac{e^{-jkR_1}}{4\pi R_1} \qquad (7)$$

and

$$\Pi_{1x}^r = -\, I_0\, \frac{e^{-jkR_2}}{4\pi\, R_2} + \frac{I_0 k}{4\pi j} \int_\Gamma \frac{\sin\xi\, \cos\xi}{\cos\xi + \sqrt{\kappa - \sin^2\xi}}$$

$$\cdot H_0^{(2)}(kR_2 \sin\theta_2 \sin\xi)\, \exp(-jkR_2 \cos\theta_2 \cos\xi)\, d\xi \qquad (8)$$

100

where $k = \omega\sqrt{\mu_0\varepsilon_0}$, $I_0 = (j\omega\varepsilon_0)^{-1} I\,dx'$, θ_2 is shown in Figure 1, and $H_0^{(2)}$ is the Hankel function of zero-order and second kind. The integration path Γ is shown in Figure 2. We have split Π_{1x} into Π_{1x}^i and Π_{1x}^r in order to emphasize the contributions obtained from the source at point 1, i.e., incident, and from its image at point 2, i.e., reflected, respectively. Furthermore, Π_{1z} takes the following form

$$\Pi_{1z} = -\frac{I_0 k}{4\pi}\cos\phi_2 \int_\Gamma \sin^2\xi\,\cos\xi\,\frac{\cos\xi - \sqrt{\kappa - \sin^2\xi}}{\kappa\cos\xi + \sqrt{\kappa - \sin^2\xi}}$$

$$\cdot H_1^{(2)}(kR_2\sin\theta_2\sin\xi)\exp(-jkR_2\cos\theta_2\cos\xi)\,d\xi \qquad (9)$$

where $H_1^{(2)}$ is the Hankel function of first order and second kind, and ϕ_2 shown in Figure 1. In (8) and (9), one must retain $\mathrm{Im}[\sqrt{\kappa - \sin^2\xi}] < 0$.

Expressions (8) and (9) cannot be evaluated in a closed form, and recently there have been some attempts to evaluate an equivalent version of them in the numerical sense [5,6,7]. The present authors have also developed an efficient method for numerical evaluation of (8) and (9). The results of this investigation will be reported in their future work. In this paper, only the asymptotic determination of (8) and (9) would be of interest, because it is assumed that the current element height $z = h > \lambda/2$ and the observation point are away from the interface. It is known that under these conditions asymptotic values of (8) and (9) would be an accurate approximation [5,6,8]. To this end, one replaces the Hankel functions in (8) and (9) by their asymptotic expressions and employs the standard saddle-point integration technique to finally arrive at

$$\Pi_{1x}^r \sim I_0 \left[\frac{2\cos\theta_2}{\cos\theta_2 + \sqrt{\kappa - \sin^2\theta_2}} - 1\right]\frac{e^{-jkR_2}}{4\pi R_2} \qquad (10a)$$
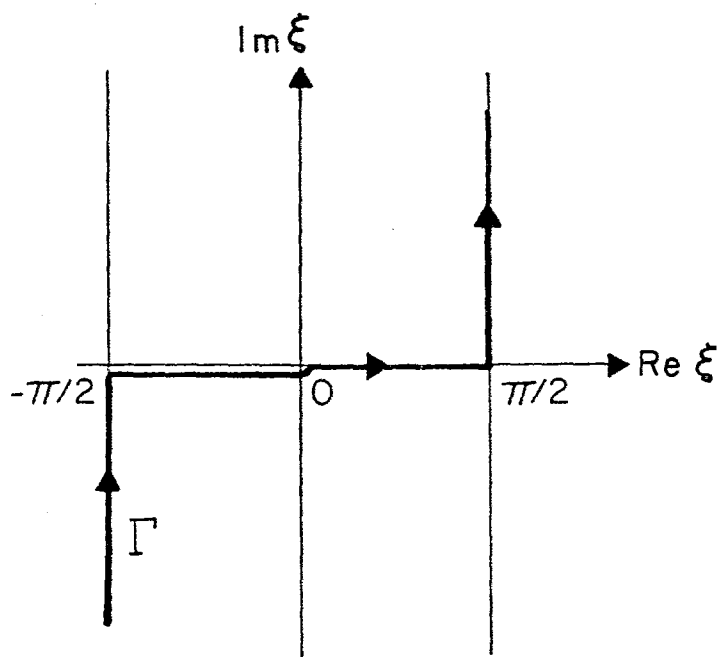
Fig. 2.   Integration path Γ in the complex ξ-plane.

and

$$\Pi_{1z} \sim 2I_0 \cos \phi_2 \sin \theta_2 \cos \theta_2 \frac{\cos \theta_2 - \sqrt{\kappa - \sin^2 \theta_2}}{\kappa \cos \theta_2 + \sqrt{\kappa - \sin^2 \theta_2}} \frac{e^{-jkR_2}}{4\pi R_2} \quad (10b)$$

$$\frac{\partial}{\partial z} \Pi_{1z} \sim -jk \cos \theta_2 \Pi_{1z} \quad . \quad (10c)$$

Since for angles $\theta_2 \sim 0$ the argument of the Hankel functions in (8) and (9) is small, it might appear that these Hankel functions cannot be replaced by their asymptotic expressions. However, if one proceeds to use the asymptotic expressions and then finds the limit as $\theta_2 \sim 0$, the results of (10) will be recovered. Therefore, (10) is valid for all θ_2 as long as the aforementioned conditions for asymptotic approximations are satisfied.

Substituting (10a) through (10c) into (3c) and employing the far-field approximation, one arrives at the following expression for the $\vec{E}^r$ (reflected) field:

$$E_\theta^r \hat{\theta}_2 = -k^2 I_0 \cos \theta \cos \phi_2 \left[\frac{\kappa \cos \theta_2 - \sqrt{\kappa - \sin^2 \theta_2}}{\kappa \cos \theta_2 + \sqrt{\kappa - \sin^2 \theta_2}} \right] \frac{e^{-jkR_2}}{4\pi R_2} \hat{\theta}_2 \quad (11)$$

and

$$E_\phi^r \hat{\phi}_2 = -k^2 I_0 \sin \phi_2 \left[\frac{\cos \theta_2 - \sqrt{\kappa - \sin^2 \theta_2}}{\cos \theta_2 + \sqrt{\kappa - \sin^2 \theta_2}} \right] \frac{e^{-jkR_2}}{4\pi R_2} \hat{\phi}_2 \quad . \quad (12)$$

In (11) and (12) $\hat{\theta}_2$ and $\hat{\phi}_2$ are the unit vectors of the spherical coordinates centered at the image point 2, shown in Figure 1, and the expressions in the brackets are the well-known Fresnel reflection coefficients [9]. It is, of course, an easy exercise to find the Cartesian components of $\vec{E}^r$ from (11) and (12). Furthermore, substituting (7) into (3c), one can readily arrive at the following far-field approximation for the current element

$$\vec{E}^i = k^2 I_0 \left[\hat{\theta}_1 \cos \theta_1 \cos \phi_1 - \hat{\phi}_1 \sin \phi_1\right] \frac{e^{-jkR_1}}{4\pi R_1} \qquad (13)$$

where (R_1, θ_1, ϕ_1) are the spherical coordinates centered at the source

point 1, shown in Figure 1.

III.   INTEGRAL EQUATION FORMULATION

The geometry of a thin linear antenna of length 2L and radius a mounted horizontally with height h over an imperfect ground is shown in Figure 3. It is assumed that the antenna is loaded with a resistive loading function $\Lambda(x)$, given in (1), and is fed from a finite source gap located at the mid-point of the structure. In this section, our objective is to establish an E-integral equation for the antenna current.

Let us denote the incident tangential electric field produced by the source gap as E^{inc} and the tangential scattered field by E^{sca}. The total tangential E-field may then be expressed as

$$E^{tot} = E^{inc} + E^{sca} \quad . \tag{14}$$

Application of Ohm's law allows one to relate the E^{tot} and the induced current $I(x)$ as

$$E^{tot} = \Lambda(x) \ I(x) \tag{15}$$

where $\Lambda(x)$ is defined in (1).

To find E^{sca}, we first define some new functionals. Since both the observation and source points are on the antenna, from (6), (7) and (9), we define the following

$$G_h(x, \ x') = I_0^{-1} \ \Pi_{1x} = g(x, \ x') - g_i(x, \ x') + g_h(x, \ x') \tag{16}$$

where

$$g(x, \ x') = \frac{e^{-jkR}}{4\pi R} \quad ; \quad R = \sqrt{(x - x')^2 + a^2} \tag{17a}$$

$$g_i(x, \ x') = \frac{e^{-jkR}}{4\pi R} \quad ; \quad R = \sqrt{(x - x')^2 + 4h^2} \tag{17b}$$
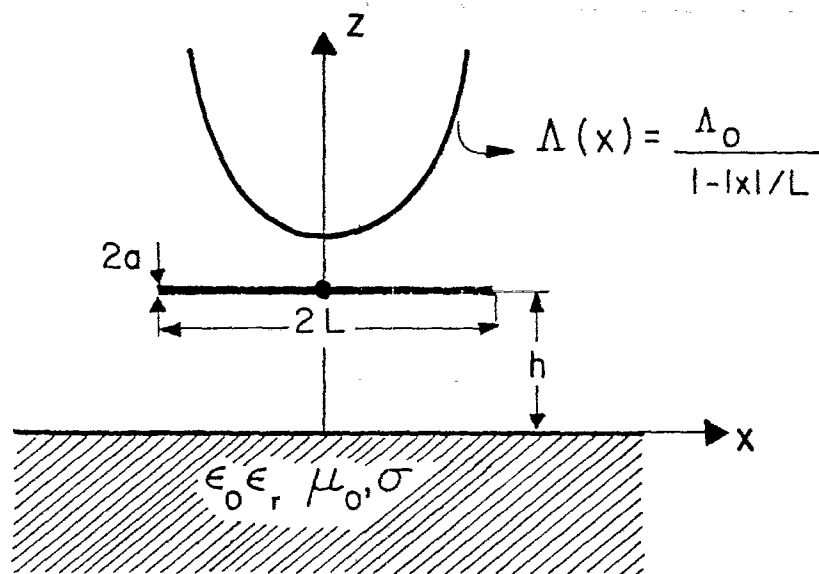
Fig. 3. Nonuniform resistively loaded horizontal antenna over an imperfect ground.

$$g_h(x, x') = \frac{2 \cos \theta_2}{\cos \theta_2 + \sqrt{\kappa - \sin^2 \theta_2}} \, g_i(x, x') \tag{17c}$$

and $\theta_2 = \text{Arctan} \left(|x - x'|/2h \right)$. In (16) subscripts h and i are used to denote "horizontal" and "image" terms, respectively. Furthermore, it should be mentioned that in defining (17a), we have incorporated the usual thin-wire approximation. Finally, from (10b), the following functional (vertical) is defined

$$G_v(x, x') = I_0^{-1} \frac{\partial}{\partial z} \Pi_{1z} = -2jk \frac{(x - x')}{|x - x'|} \sin \theta_2 \cos^2 \theta_2 \frac{\cos \theta_2 - \sqrt{\kappa - \sin^2 \theta_2}}{\kappa \cos \theta_2 + \sqrt{\kappa - \sin^2 \theta_2}}$$

$$\cdot \, g_i(x, x') \tag{18}$$

where $(x - x')/|x - x'|$ accounts for the change of the sign of $\cos \phi_2$ in (10b). It is apparent that for the perfect ground, i.e., $\kappa \to \infty$, both g_h and G_v vanish.

The tangential scattered field E^{sca} can be determined by substituting (16) and (18) into (3c). Finally the desired integral equation for the antenna current is obtained from (14) as follows

$$E^{inc}(x) = -(j\omega\varepsilon_0)^{-1} \left(\frac{d^2}{dx^2} + k^2 \right) \int_{-L}^{L} G_h(x, x') \, I(x') \, dx'$$

$$-(j\omega\varepsilon_0)^{-1} \frac{d}{dx} \int_{-L}^{L} G_v(x, x') \, I(x') \, dx' + \Lambda(x) \, I(x),$$

$$- L \leq x \leq L \quad . \tag{19}$$

In the next section, we describe the numerical steps employed to solve (19) for the determination of I(x) and the critical loading Λ_0^c, defined in (1).

IV. NUMERICAL CONSIDERATIONS

Standard numerical techniques based on the application of the method of moments [10] are used to transfer the integral equation (19) into a matrix equation. Two different schemes are used to generate the matrix equation. First, Harrington's triangular basis function [10] and point matching are employed. In this case the differential operators are transferred inside the integral sign and calculated in the manner described by Harrington [11]. The details of this procedure with a working computer program is also given in [12]. Second, the pulse basis function and point matching are used. In this case, the differential operators are evaluated outside the integral sign by applying a finite difference algorithm in the manner used in [13,14]. In all the cases, attempts are made to exploit the symmetries involved in filling the matrix elements in order to reduce computation time. Furthermore, the gap generator, i.e., $E^{inc}(x)$, is modeled as a column matrix with zero elements except at the center element where it takes the value one divided by the gap size.

As Λ_0 approaches the critical loading value, the current matrix $I(x_n)$ will take a linear phase shift among its elements, x_n's being coordinates of the patch centers, since one expects no reflection from the antenna ends due to the travelling wave nature of the current distribution. Based on this simple concept, we introduce the error function, hereafter denoted as $ER(\Lambda_0)$. For a given value of Λ_0, first the current matrix is computed, then the current phases are interpolated by a straight line such that the least square error is achieved (see Figure 4). This value of the least square error is the defined value of $ER(\Lambda_0)$ which is associated with the given Λ_0. It is apparent that as Λ_0 approaches the critical loading, $ER(\Lambda_0)$ will approach zero. Since perfect reflectionless behavior cannot

108
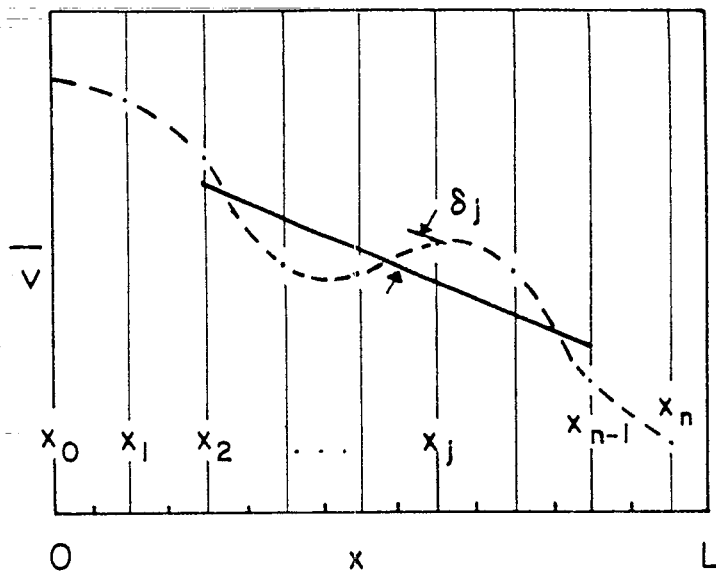
Fig. 4.   Determination of least square error for current phases, i.e., $ER(\Lambda_0) = \underset{j}{Min} \sum_j \delta_j^2$.

be achieved, we define the critical loading as Λ_0^c which minimized $ER(\Lambda_0)$, that is

$$\left. \frac{\partial ER(\Lambda_0)}{\partial \Lambda_0} \right|_{\Lambda_0^c} = 0 \qquad . \qquad (20)$$

There is now sufficient information to numerically compute the optimal Λ_0^c. Initially three consecutive values of Λ_0, i.e., $\Lambda_{01} < \Lambda_{02} < \Lambda_{03}$, are sought such that $ER(\Lambda_{01})$, and $ER(\Lambda_{02}) > ER(\Lambda_{02})$. This condition states that Λ_0^c is within the interval $[\Lambda_{01}, \Lambda_{03}]$. Note that we are interested in the first local minimum as the smallest value of Λ_0^c, which is most desirable. Successive parabolic interpolation through the three points and the finding of a new minimum will finally converge to the optimal Λ_0^c. It has been found that better convergence is obtained by ignoring the feed and the end patches in computing $ER(\Lambda_0)$. This observation is not too surprising as the radiation occurs mainly at these points and we expect the current behavior to deviate from its characteristic traveling wave.

V. NUMERICAL RESULTS AND DISCUSSION

The first example will consider a two-meter dipole antenna radiating in free space at frequency f = 50 MHz (λ = 2/3 m). Figure 5 shows the magnitude and the phase of the induced current for three different loading parameters Λ_0. The critical loading Λ_0^c = 247.2 Ω was determined in the manner described earlier. As the loading parameters take the no-loading value Λ_0 = 0, the intermediate value Λ_0 = 120, and finally the critical loading Λ_0 = 247.2, the phase behavior becomes more linear. On the other hand, the amplitude curve assumes a non-oscillatory behavior and varies similar to the current of a nonreflecting structure. We have chosen the example in order to compare our results with those given in [2]. In this reference the value of the critical loading was reported as Λ_0^c = 318 Ω, though no specific procedure for the determination of Λ_0^c was described. We believe that the main difference between our result and the one in reference [2] lies in the application of different numerical schemes for reducing the integral equation into a matrix equation.

In order to fully investigate the effect of ground and loading on the antenna performances, we consider a center-fed dipole antenna of length 2L = 10 m located at a height of h = 5 m above an imperfect ground (ε_r = 10, σ = .01 mhos/m). Table 1 contains the values of critical loading Λ_0^c as a function of frequency for two different radii of the antenna in free space. In this table, the minimum error, i.e., ER(Λ_0^c), is also tabulated. It is interesting to note that for the entire frequency range, a smaller Λ_0^c is needed as the radius changes from .025 m to .05 m. Table 2 shows the variation of Λ_0^c as a function of ε_r and σ for a fixed antenna radius a = .05 m. To illustrate the functional dependence of ER(Λ_0) on Λ_0, two plots are

111
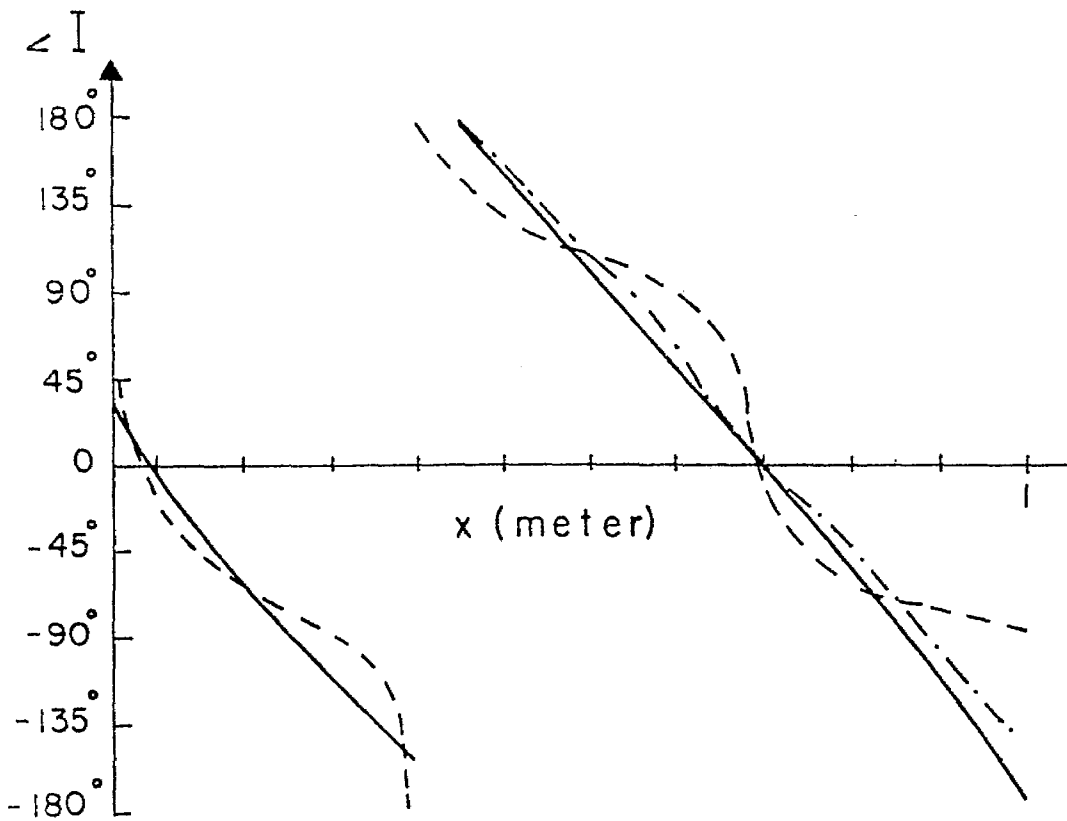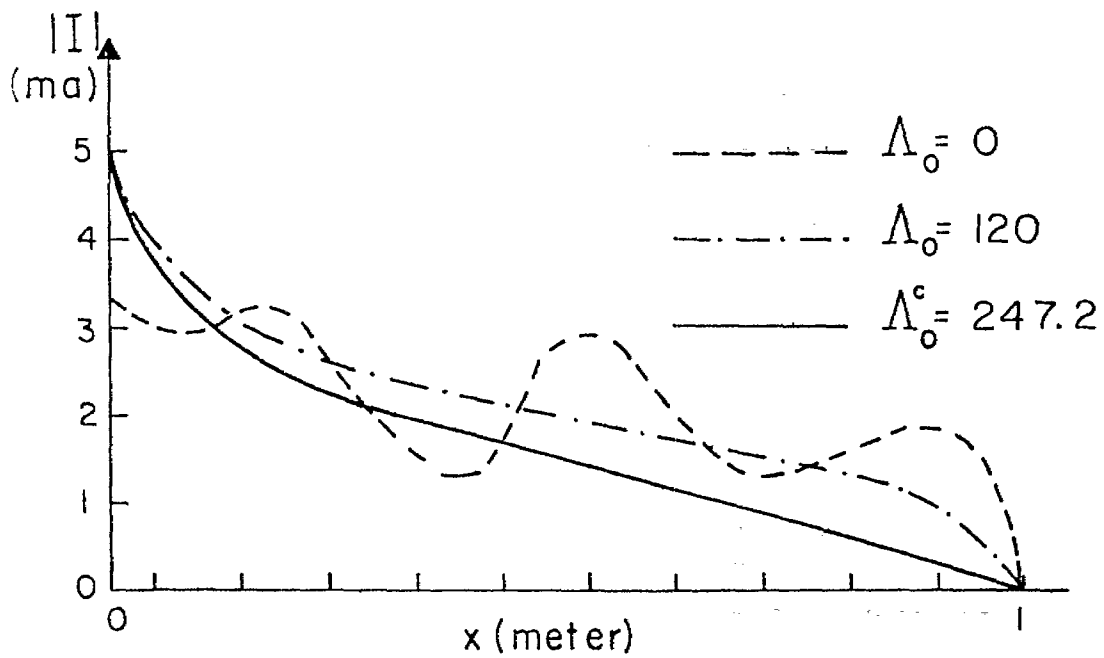
Fig. 5. Magnitude and phase of the current for three different loading
parameters. 2L = 2m and λ = 2/3m.

TABLE 1

CRITICAL LOADING PARAMETER Λ_0^c AND THE MINIMIZED ERROR $ER(\Lambda_0^c)$

VERSUS FREQUENCY FOR TWO ANTENNA RADII. 2L = 10 m.

	Radius = .025 (m)		Radius = .05 (m)			Radius = .025 (m)		Radius = .05 (m)	
Freq. (MHz)	Λ_0^c (Ω/m)	$ER(\Lambda_0^c)$	Λ_0^c (Ω/m)	$ER(\Lambda_0^c)$	Freq. (MHz)	Λ_0^c (Ω/m)	$ER(\Lambda_0^c)$	Λ_0^c (Ω/m)	$ER(\Lambda_0^c)$
18	35.3	3.2	28.4	4.	54	89.0	2.94	72.3	2.40
21	47.6	6.4	39.2	7.9	57	88.2	1.94	69.7	1.75
24	55.8	9.6	46.0	11.6	60	88.2	1.81	70.6	1.19
27	61.7	12.3	52.7	14.5	63	85.2	1.50	70.7	1.38
30	67.0	14.3	59.8	16.2	66	82.8	1.63	67.4	1.43
33	75.1	16.7	63.4	16.5	69	82.5	1.63	64.6	2.06
36	82.3	16.4	70.0	15.3	72	82.8	1.94	64.0	2.31
39	81.6	11.9	71.9	11.0	75	80.6	2.2	63.1	2.88
42	86.3	9.98	73.1	9.75	78	80.3	2.38	63.2	3.06
45	88.9	7.81	74.4	7.67	81	80.1	2.63	62.0	3.56
48	89.6	5.56	74.4	5.5	84	78.2	3.31	60.6	4.56
51	89.8	4.5	73.1	3.9	87	79.5	3.38	59.6	5.06
					90	76.3	4.18	59.6	5.56
					95	74.8	4.94	60.1	7.0
					100	73.6	6.56	40.3	10.1

TABLE 2

CRITICAL LOADING PARAMETER Λ_0^c AND THE MINIMIZED ERROR ER(Λ_0^c) VERSUS FREQUENCY

FOR DIFFERENT GROUND PARAMETERS. $2L = 10$ m, AND $h = 5$ m.

Freq. (MHz)	$\epsilon_r = 1, \sigma = 0$ mhos/m		$\epsilon_r = 5, \sigma = .001$		$\epsilon_r = 10, \sigma = .01$		$\epsilon_r = 80, \sigma = 4$		$\epsilon_r = 1, \sigma = \infty$	
	Λ_0^c (Ω/m)	ER(Λ_0^c)	Λ_0^c (Ω/m)	ER(Λ_0^c)	Λ_0^c (Ω/m)	ER(Λ_0^c)	Λ_0^c (Ω/m)	ER(Λ_0^c)	Λ_0^c (Ω/m)	ER(Λ_0^c)
30	59.8	16.2	59.4	16.9	53.5	15.9	49.9	15.1	49.5	15.1
33	63.4	16.5	60.6	16.4	64.5	18.9	60.9	20.0	60.1	20.8
36	70.0	15.3	65.9	18.0	72.6	18.6	68.1	20.0	67.8	19.9
39	71.9	11.0	76.2	13.2	79.2	14.7	77.2	16.2	80.9	17.9
42	73.1	9.75	79.6	11.6	83.0	12.0	91.0	14.3	89.7	14.4
45	74.4	7.67	82.1	8.2	85.9	8.5	100.1	10.0	97.4	10.1
48	74.4	5.5	79.8	5.6	86.3	5.6	160.2	2.9	151.1	3.4
51	73.1	3.9	79.2	3.6	84.8	3.3	139.6	1.1	130.5	1.9
54	72.3	2.4	81.1	2.6	79.6	1.9	87.1	1.6	104.0	1.9
57	69.7	1.75	70.1	1.6	69.9	2.3	69.2	4.0	71.8	4.1
60	70.0	1.2	66.6	2.4	61.3	3.4	60.9	8.8	59.7	9.0

114

constructed in Figure 6. These plots show the effect of the imperfect

ground on $ER(\Lambda_0)$. Since the antenna height is $h = \lambda$ and the ground has

low conductivity, the two results do not differ markedly.

The effect of Λ_0 on the input resistance of the aforementioned antenna

is depicted in **Figure 7, where the two cases of no ground and imperfect**

ground are considered. **This figure suggests that as Λ_0 becomes larger, in**

this case for instance $\Lambda_0 > 30$ Ω/m, the input resistance levels off and

does not vary significantly. For yet another example, Figure 8 displays

the variation of the input resistance versus frequency for loading parameters

$\Lambda_0 = 0$, i.e., no loading, and $\Lambda_0 = 40$ Ω/m, though this figure is for the no-

ground case ($\varepsilon_r = 1$, $\sigma = 0$ mho), it is clearly seen that when the antenna is

not loaded, the input resistance varies with the resonant frequencies of the

antenna, whereas when it is sufficiently loaded, the input resistance does

not vary markedly as the antenna ends are not seen from the feed point.

To investigate the radiation pattern characteristic of a loaded

antenna over an imperfect ground, a center-fed dipole antenna of length

$2L = 10$ m and radius $a = .05$ m located at the height $h = 5$ m over an

imperfect ground ($\varepsilon_r = 10$, $\sigma = .01$ mhos/m) is considered. Furthermore, it is

assumed that the antenna is radiating at frequency $f = 60$ MHz ($\lambda = 5$ m).

From Tables 1 and 2, it is found that the critical loading is $\Lambda_0^c = 70.6$ (Ω/m)

in the absence of the ground and $\Lambda_0^c = 61.3$ (Ω/m) in its presence,

respectively. Figure 9 shows the amplitude and phase distributions of the

antenna current I for the cases of both no loading and critical loading.

Again the linear phase behavior is obtained for the critical loading case.

The radiation patterns of the aforementioned antenna are plotted in

Figures 10, 11, and 12. All patterns are normalized to the maximum value

of the E-field shown in Figure 10. In each figure radiation patterns of

115
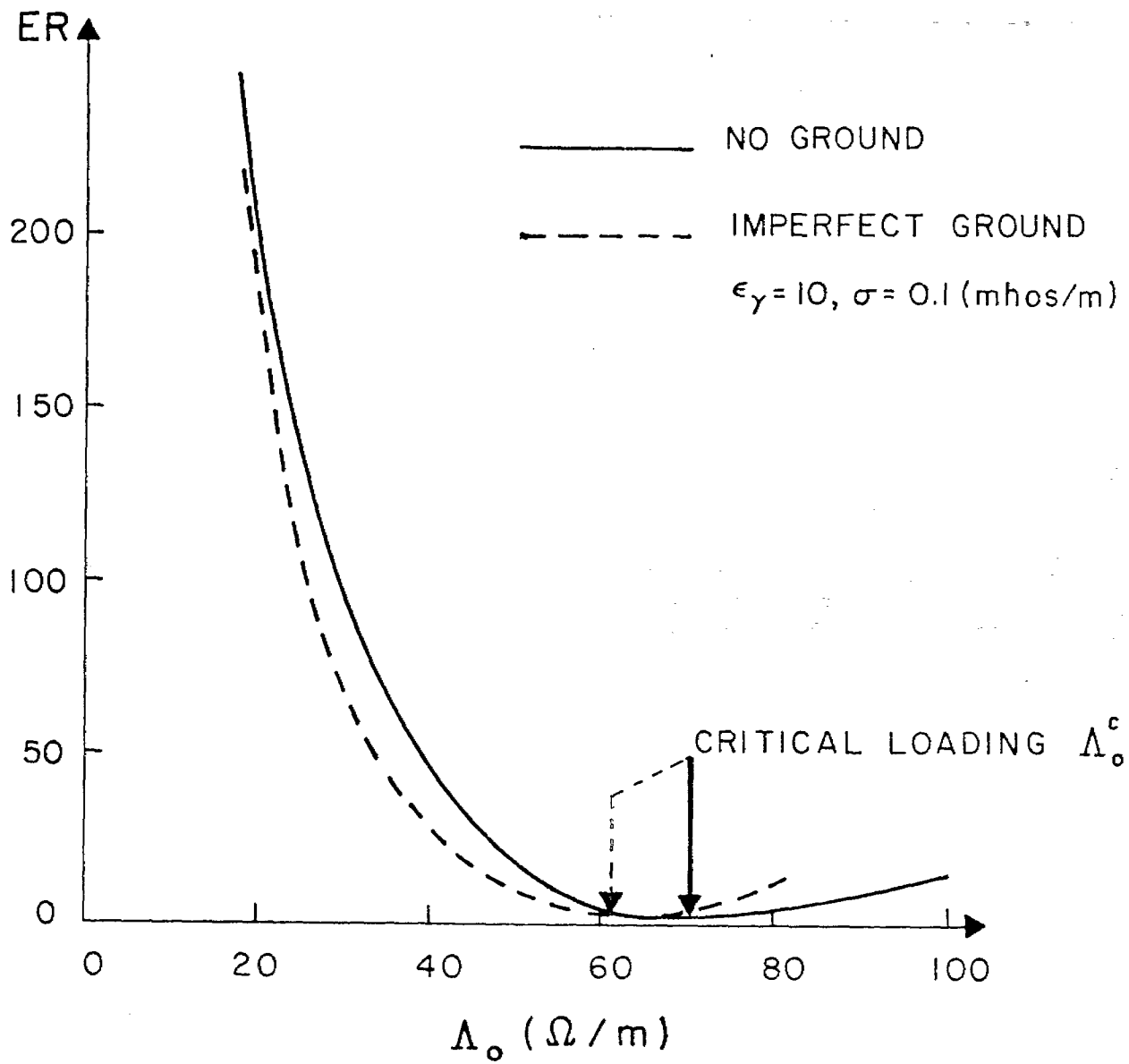
Fig. 6. Effects of imperfect ground on $ER(\Lambda_0)$.
2L = 10 m, h = 5 m and λ = 5 m.
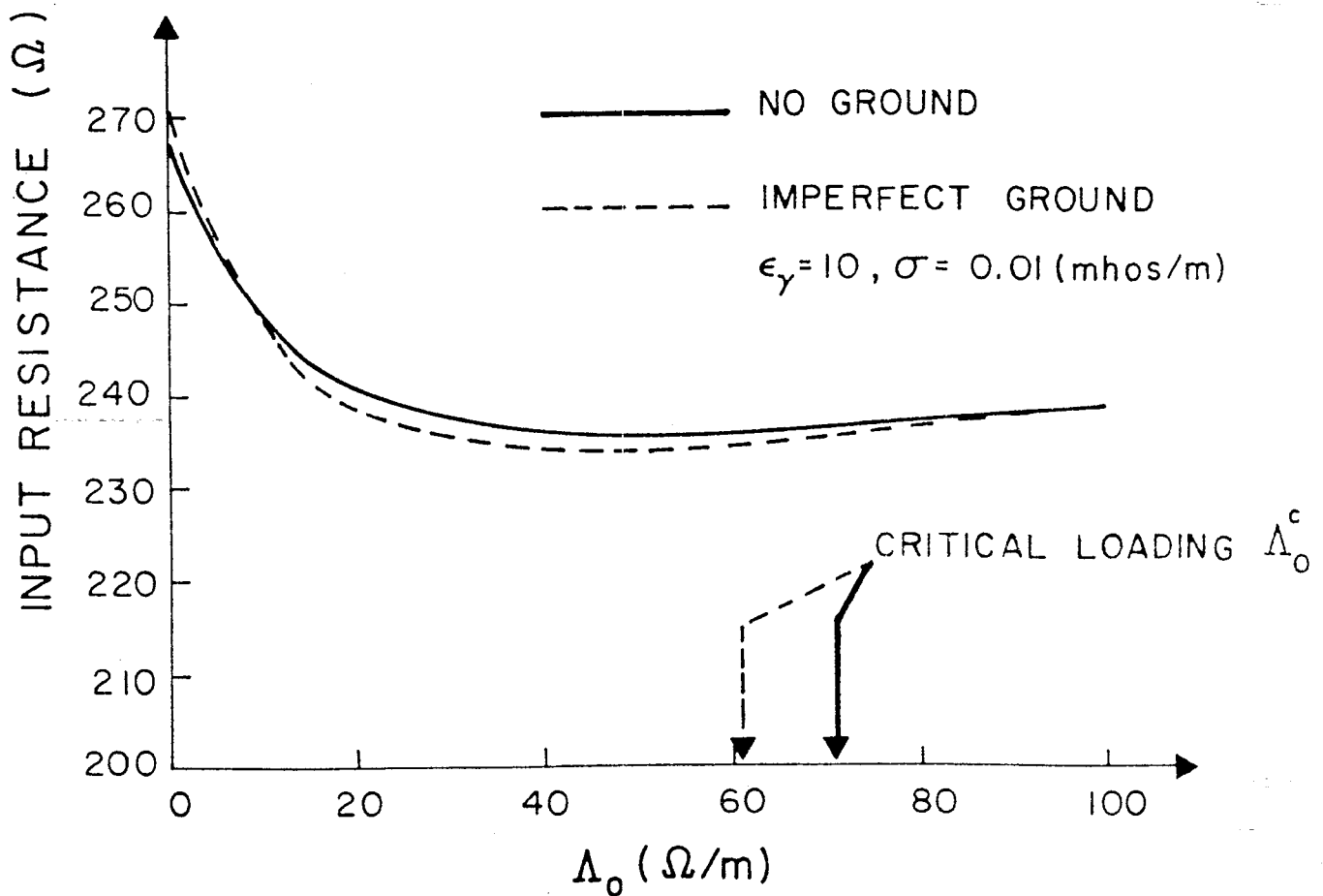
Fig. 7. Effect of Λ_0 on input resistance, no ground and imperfect ground cases. $2L = 10$ m, $h = 5$ m and $\lambda = 5$ m.
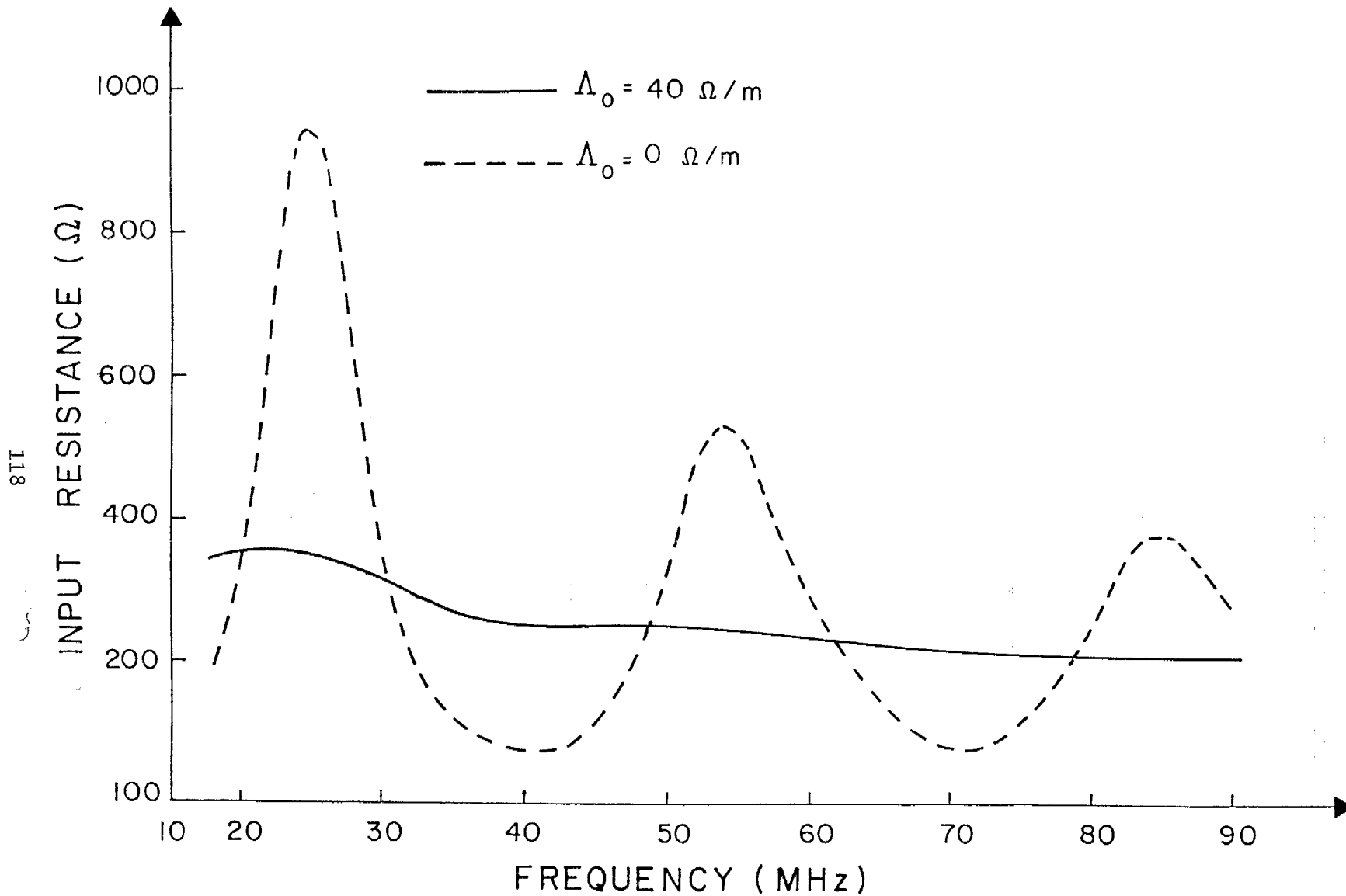
Fig. 8. Input resistance versus frequency for loaded and unloaded antenna in free space. 2L = 10 m.
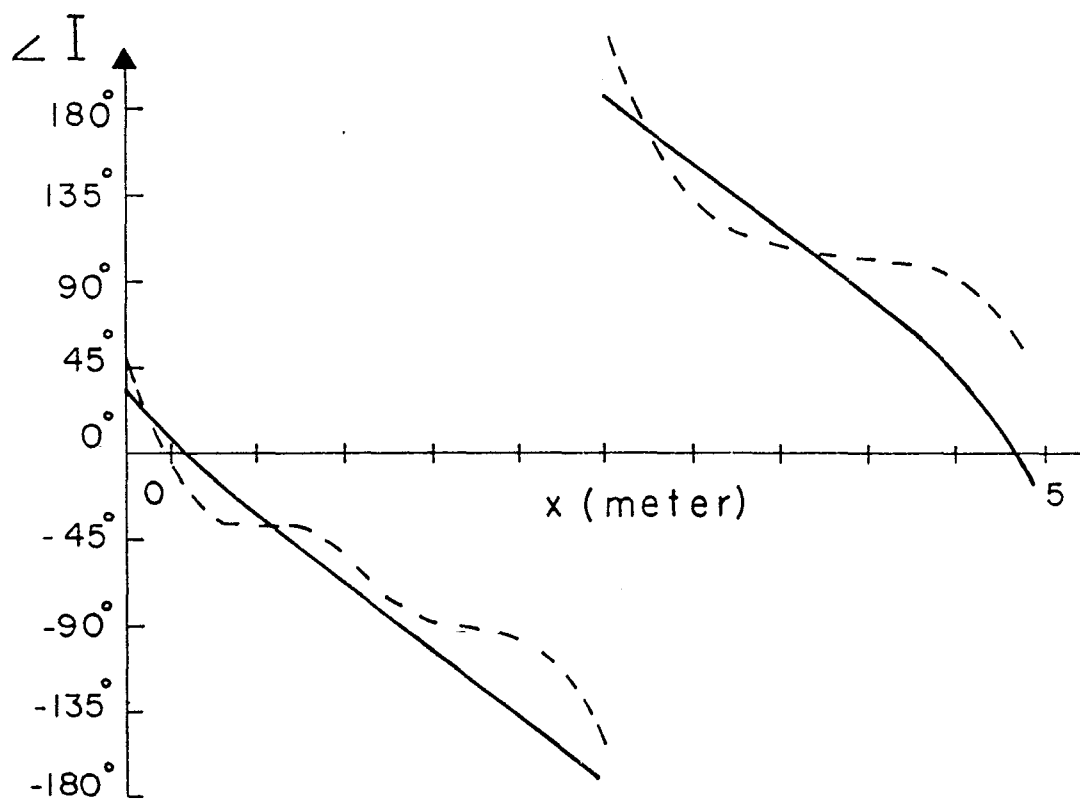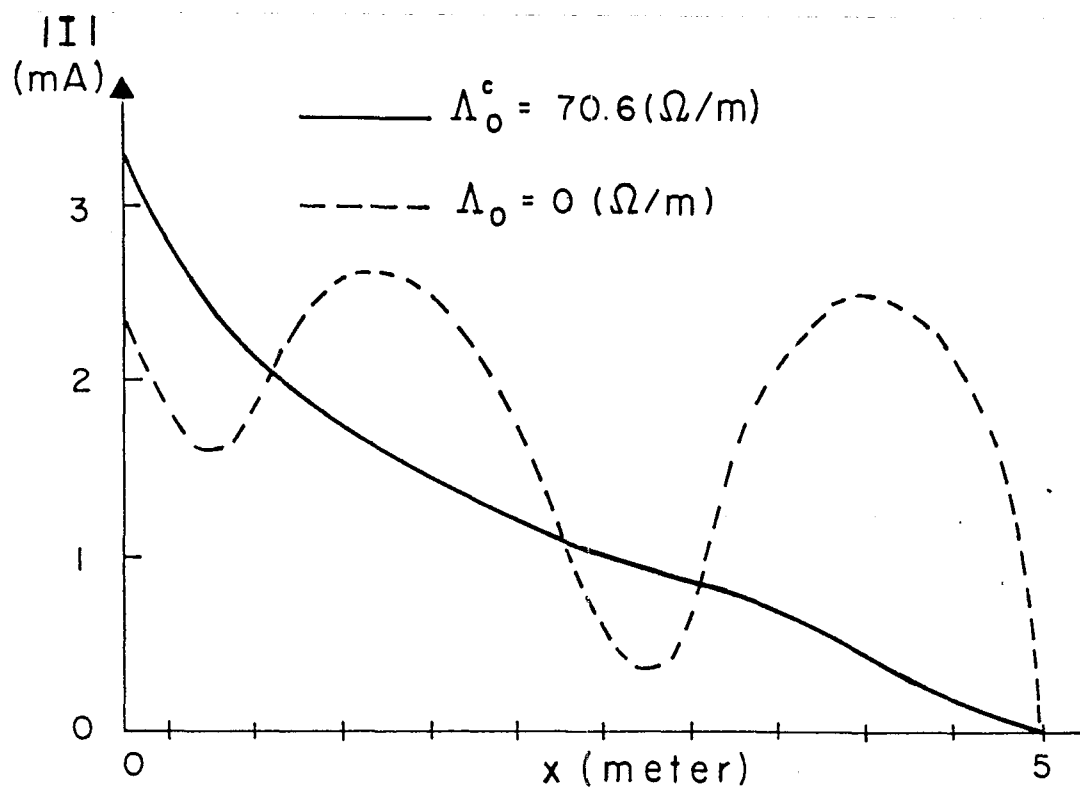
Fig. 9. Magnitude and phase of current for no loading and critical loading. $2L = 10$ m, and $\lambda = 5$ m.
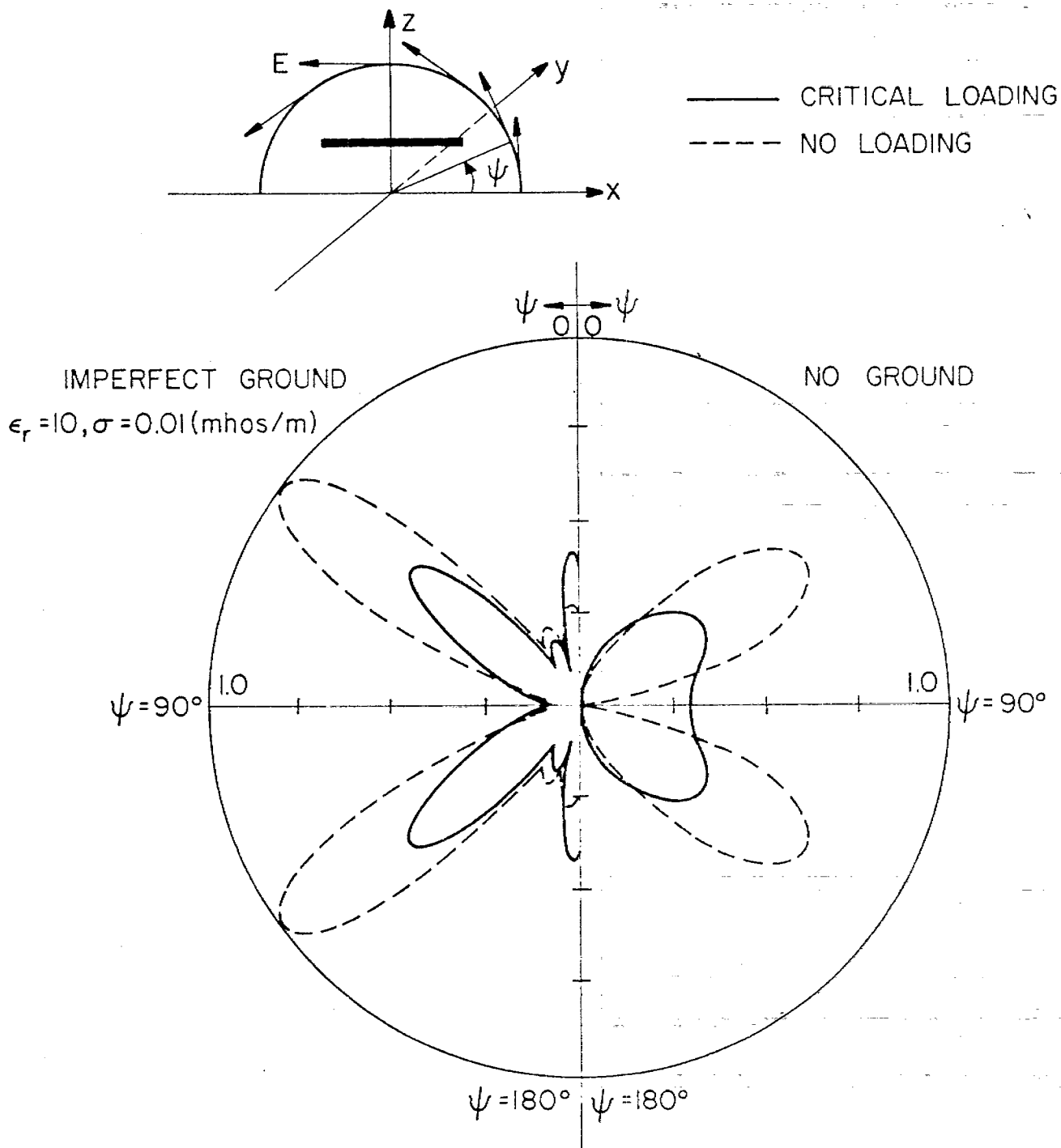
Fig. 10. Radiation pattern in plane X-Z for no ground, imperfect ground, no loading and critical loading. 2L = 10 m, h = 5 m, and λ = 5 m.
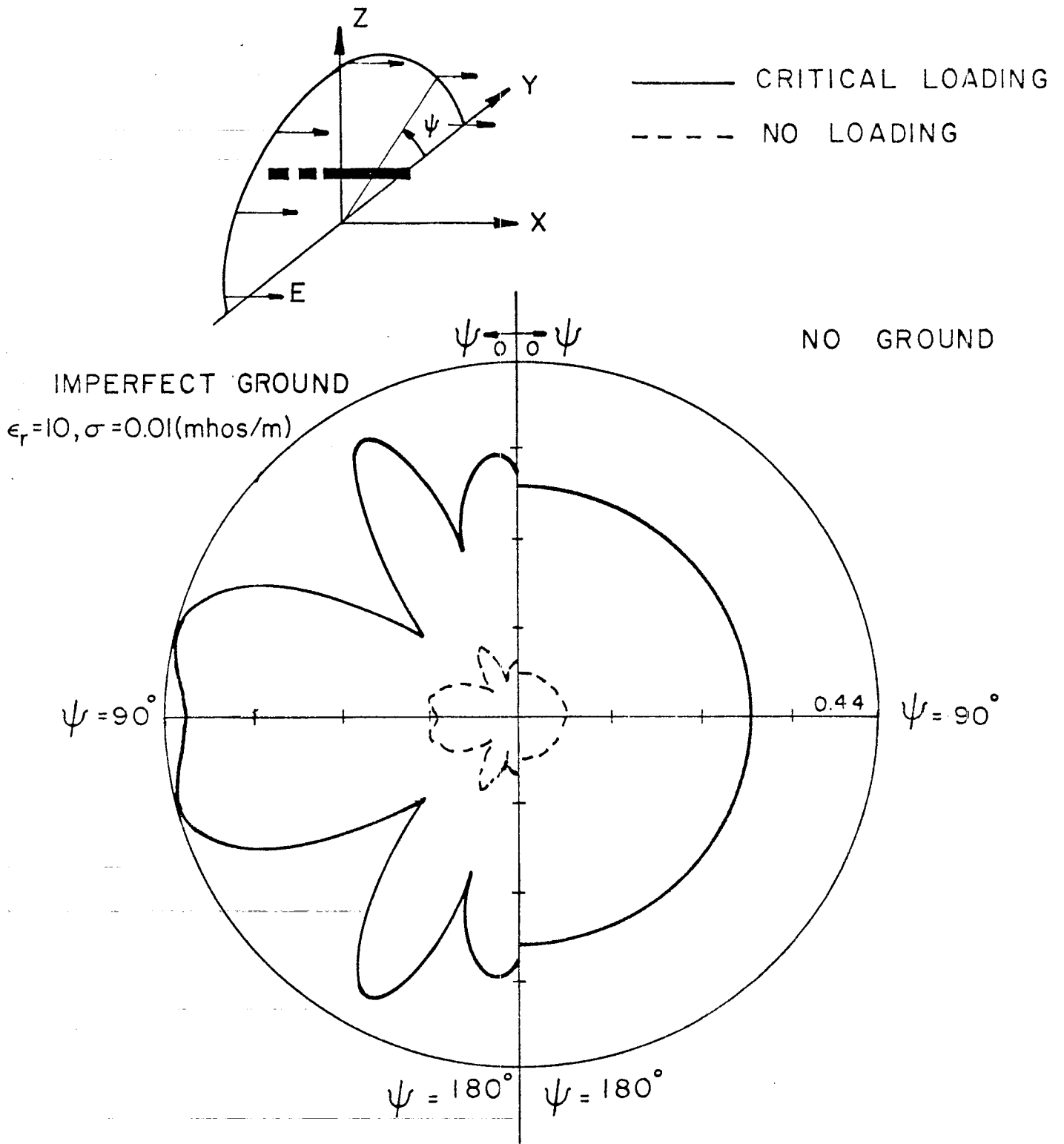
Fig. 11. Radiation pattern in plane Y-Z for no ground, imperfect ground, no loading and critical loading. 2L = 10 m, h = 5 m and λ = 5 m.
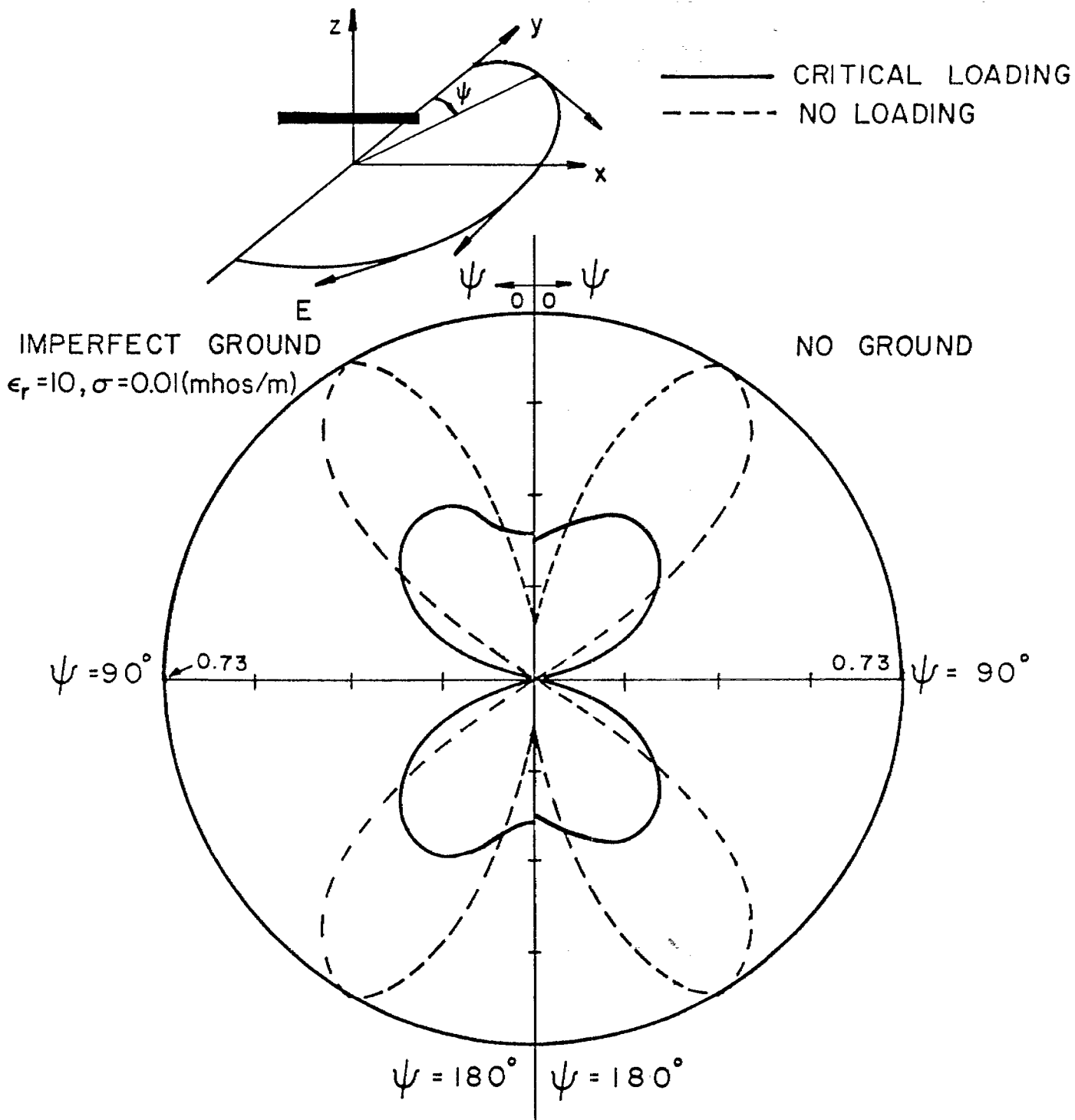
Fig. 12. Radiation pattern in X-Y plane for no ground, imperfect ground,
         no loading and critical loading. 2L = 10 m, h = 5 m and λ = 5 m.

the antenna in both the presence and absence of the ground for no loading and critical loading are plotted. This allows the reader to compare the results simultaneously. Except for the antenna pattern in the plane perpendicular to the antenna (Figure 11), the shape of the pattern is changed due to the loading effect. Except for the antenna pattern in the plane parallel to the ground interface (Figure 12), the pattern is effectively influenced by the presence of the imperfect ground. These results can intuitively be verified for most cases.

REFERENCES

[1] Special Joint Issue on the Nuclear Electromagnetic Pulse, IEEE Trans. on Antennas and Propagation, January 1978 and also in IEEE Trans. on Electromagnetic Compatibility, February 1978.

[2] Y. P. Liu, D. L. Sengupta, and C. T. Tai, "On the Transient Wave Forms Radiated by a Resistively Loaded Linear Antenna," Sensor and Simulation Notes, Note 178, February 1973.

[3] F. M. Tesche, "Application of the Singularity Expansion Method to the Analysis of Impedance Loaded Linear Antennas," Sensor and Simulation Notes, Note 177, May 1973.

[4] A. Sommerfeld, Partial Differential Equations in Physics, New York: Academic Press, 1964.

[5] E. K. Miller, A. J. Poggio, G. J. Burke and E. S. Selden, "Analysis of Wire Antennas in the Presence of Conducting Half-Space: Part II The Horizontal Antenna in Free Space," Canadian J. or Physics, Vol. 50, pp. 2614-2627, 1972.

[6] T. K. Sarkar and B. J. Strait, "Analysis of Arbitrarily Oriented Thin Wire Antenna Arrays Over Imperfect Ground Planes," Scientific Report No. 9 on contract F19628-73-C-0047, AFCRL-TR-75-0641, Syracuse University, Syracuse, New York, December 1975.

[7] A. Banos, Dipole Radiation in the Presence of Conducting Half-Space, New York: Pergamon Press, 1966.

[8] J. A. Kong, Theory of Electromagnetic Waves, New York: Wiley, 1975.

[9] E. C. Jordan and K. G. Balmain, Electromagnetic Waves and Radiating Systems, New Jersey: Prentice Hall, 1968.

[10] R. F. Harrington, Field Computation by Moment Methods, New York: McMillan, 1968.

[11] R. F. Harrington, "Matrix Methods for Field Problems," Proc. IEEE, pp. 136-149, February 1967.

[12] J. D. McCannon, "Numerical Analysis of a Thin-Wire Antenna Near Lossy Ground," M.S. Thesis, University of Illinois, Urbana, Illinois, 1972.

[13] R. Mittra and W. L. Ko, "A Finite Difference Approach to the Wire Junction Problem," IEEE Trans. Antennas Propagat., Vol. AP-23, pp. 435-438, May 1975.

[14] P. Parhami, Y. Rahmat-Samii, and R. Mittra, "A Technique for Calculating the Radiation and Scattering Characteristics of Antennas Mounted on a Finite Ground Plane," to appear in Proc. IEE .